# Analog quantum simulator of the multistate Landau-Zener model

zur Erlangung des akademischen Grades

Doktor der Naturwissenschaften

von der KIT-Fakultät für Physik des

Karlsruher Instituts für Technologie (KIT)

genehmigte

**Dissertation**

von

M.Sc. Alexander Denis Stehli

| | |
|---|---|
| Tag der mündlichen Prüfung: | 12.02.2021 |
| Referent: | Prof. Dr. Alexey V. Ustinov |
| Korreferent: | Prof. Dr. Martin Weides |

# Contents

# 1 Introduction

For the last decades, scientific and technological advances have been driven by classical computers based on semiconductor circuits. The steady growth of their computational power was promoted by a continuous increase of the transistor density in these devices, which, for the last 50 years, has approximately followed the exponential Moore's law [Our17]. However, a fundamental limit to further growth is imminent in the near future: When the underlying semiconducting circuit elements (currently on the scale of a few nanometers) reach the size of several atoms, quantum effects start to set in and may cause a loss of functionality. Even before this point is reached, it may not be viable from an economic point of view to cling to the man-made Moore's law [Wal16]. While future advances can still be expected to a certain extent, they will likely rely on innovations or the specialization of the processing units, such as the ray tracing acceleration units implemented in modern graphics cards [Nvi18].

In the light of this impending development, the demand for increasingly powerful computers has sparked the interest in an idea that has been around since the early 1980s [Fey82], that is, computing based on quantum states, rather than classical systems. In analog to their classical counterpart, the central building blocks of a quantum computer are quantum bits, or short - qubits. Qubits are quantum systems with two isolated energy eigenstates, replacing the classical 0 and 1 of a bit. Naturally, they can be initialized in an arbitrary superposition of their eigenstates. Multiple qubits can be entangled with each other, resulting in the exponential growth of the underlying Hilbert space. This enables a massive parallelization during computation, which is exploited by quantum algorithms, for example, for integer factorization [Sho97] and database search [Gro96]. A universal quantum computer with $\gtrsim$50 ideal qubits can outperform the most powerful classical computers at selected tasks [Boi+18].

But what kind of hardware is used to implement a quantum computer? A quantum system is suitable as a qubit if it has two individually addressable energy levels, which are distinguishable in a projective measurement to extract the current state. Many systems, such as trapped ions [CZ95; Mon+95; MK13], cold atoms [Blo08], and nitrogen-vacancy centers in diamond [JW06], come with intrinsically good

coherence properties, i.e., a measure for how long the system retains its quantum information. In superconducting qubits, on the other hand, the quantum state is encoded in the phase and charge degrees of freedom of an artificially patterned circuit [MSS01; Wen17; Kja+20]. These devices are operated at ultra-low temperatures just above absolute zero in order to reduce noise caused by thermal excitations. Nevertheless, early qubit implementations struggled with high energy and coherence loss rates. Over the last two decades, this has been improved dramatically: State of the art qubits feature coherence times on the order of $100 - 300\,\mu s$ [Ner+19; Zha+20; Pla+20], which is long enough to execute several thousand qubit gates [Kja+20]. Most recently, a quantum advantage over classical computers was for the first time demonstrated on a superconducting quantum processor [Aru+19].

A key factor of the stellar success of superconductor-based quantum information is a meticulous fabrication of the structures encoding their quantum properties. The center piece of (almost) all superconducting quantum circuits are Josephson junctions. In qubits, these nonlinear elements are used to isolate the two computational states from the rest of the complex energy spectrum. In practice, the Josephson contacts are realized with a simple superconductor-insulator-superconductor interface. Due to the simplicity of the surrounding circuitry, scaling up to larger devices with more qubits often boils down to streamlining the fabrication of the Josephson junctions, while maintaining or improving qubit coherence times [Wu+17; For+19b; Kre+20; Tsi+20]. The widespread shadow-evaporation techniques exploit free-standing bridges [Dol77] or overhangs [Lec+11] in conjunction with multi-angle evaporation to generate the desired interface in situ. This comes at the cost of a systematic angle-dependent parameter spread, especially for large-scale wafers. Sub-micron sized overlap junctions do not suffer from this effect and, therefore, have started to attract attention in recent years [Wu+17].

In the context of this thesis, we developed a subtractive process for patterning overlap Josephson junctions, compatible with standardized nanofabrication methods. In contrast to existing overlap or shadow evaporation techniques, resist masks are eliminated from the evaporation chamber during the barrier growth. The process is angle-independent and enables metal deposition at elevated temperatures or in the presence of reactive gases. This lifts preexisting restrictions on the choice of material, as well as the employed deposition and growth methods. Concurrently, subtractive patterning allows for smaller, more coherent junctions, which can be fabricated in the same process step with large contacts, utilized in quantum limited amplifiers for qubit readout [Roc+12; Mac+15; Win+20]. In conjunction with the angle-independence and scalability, this enables the integration into a streamlined and large-scale processing platform for arbitrary quantum circuits.

While the development of fabrication tools is one crucial ingredient for building systems comprising hundreds or thousands of qubits, an error-corrected universal quantum computer is still a dream of the future. However, already current and upcoming noisy intermediate-scale quantum (NISQ) devices with several decent qubits and imperfect gates are expected to exceed the capabilities of classical computers at certain tasks [Pre18]. Here, a great interest lies in quantum chemistry, where the advantage over classical simulations is rather apparent: Quantum state based computing can directly infer the energy spectrum or time evolution of the underlying systems, which obey the laws of quantum mechanics [Asp+05; Cao+19; McA+20].

Analog quantum simulators have advanced rapidly over the last years and can now tackle problems which are hard to solve, even for modern supercomputers [Ber+17; Zha+17]. Here, the simulator emulates the Hamiltonian of a model system and, thereby, mimics its properties and time dynamics. Since the simulators are tailored to a given problem, they lack the flexibility of a gate-based quantum processor. However, no sophisticated error-correction schemes are needed. Therefore, analog quantum simulation is useful, particularly for the study of universal effects. Especially, open quantum systems are an appealing target for analog quantum simulation, since they are hard to model with classical [Mos+17] and even quantum computers [GRM20]. In these open quantum systems, a small subsystem interacts with a structured environment. Typically, they are used to describe energy loss and decoherence in real quantum systems [Man20] and can be employed to study non-Markovian physics [OIL13; Pue+19]. An implementation based on superconducting circuits seems ideal, due to their tailored functionality and broad tool box, including qubits, bosonic modes, and additional drive tones.

In this work, we built a quantum simulator comprising a superconducting qubit coupled to an artificial environment composed of several bosonic modes to study the multistate Landau-Zener model. The underlying Hamiltonian describes the transient dynamics of at least two coupled quantum states, where an order parameter is used to tune the energy separation of the states linearly with time [Lan32; Zen32; Stü32]. Due to its simplicity and generality, the Landau-Zener model has a wide range of application. It is used to model molecular collisions [Chi96] and chemical reaction dynamics [Nit06]. Landau-Zener tunneling can be employed to measure the energy splitting of interacting quantum states, for example in magnetic molecular clusters [WS99]. Recently, its ubiquity in artificial quantum devices has revitalized the broad interest in the model: Mach-Zehnder-like interference effects were observed in superconducting flux [Oli+05; Ber+08] and charge qubits [Sil+06], but also in semiconductor qubits [PLG10; OHM18] and nitrogen-vacancy centers in diamond [CM10; Fuc+11]. Experimentally, the time evolution of the Landau-Zener

model was investigated to some extent at the hand of Helium Rydberg atoms [YSK92], superconducting flux qubits [Ber+08], accelerated optical latices [Zen+09], and single electronic spins [Hua+11], albeit only with two involved quantum levels. In this work, we expand these studies to the multistate model and particularly its transient dynamics, which have also found great interest in theoretical works [Vit99; ZHK08; OIL10; OIL13].

This thesis is organized as follows: In the first chapter, I provide a short introduction to superconductivity and the experimental methods needed to reach the ultra-low temperatures at which superconducting quantum devices are operated. The following chapter comprises a comprehensive introduction to the mathematical framework of qubits, particularly those based on superconducting circuits. Here, I put an emphasis on dispersive qubit readout, the most common method employed in superconducting devices. This is expanded upon in the next chapter, where the microwave circuits used to implement and operate superconducting qubits are described. Thereafter, the experimental realization of these devices is discussed. Here, I focus on the subtractive fabrication process for nanoscaled Josephson junctions published in Ref. [Ste+20], which was developed in the context of this thesis. Subsequently, the analog quantum simulation of the multistate Landau-Zener model is presented. The final chapter concludes this work with a short summary and an outlook on upcoming projects.

# 2 Superconductivity

The macroscopic quantum phenomenon "superconductivity" describes the complete loss of resistance of a material below a certain critical temperature $T_c$. For over four decades after its discovery, that is, until the development of the standard Bardeen–Cooper–Schrieffer (BCS) theory [BCS57], it was one of the most challenging problems in solid-state physics. Even today open questions remain, particularly on the topic of high-temperature superconductors. Nevertheless, superconductivity has become technologically relevant in several areas: While the most obvious application - energy transport in power grids - is still pending, magnets with high magnetic fields are almost exclusively implemented with superconducting wires, for example in magnetic resonance imaging or particle accelerators [BK12]. Superconducting devices are used to measure magnetic fields, both in science and technology [Fag06] or as particle detectors [ZR04]. Replacing large-scale, semiconductor-based servers and computers with systems based on rapid single flux quantum (RSFQ) logic promises a drastic reduction of energy consumption [LS91]. Currently, the most popular prospect also relevant in the context of this work is the realization of a quantum computer using superconducting circuits [GCS17].

Superconductivity is a broad research area and a thorough discussion far exceeds the frame of this thesis. In this chapter, I discuss some of its fascinating aspects, with a focus on those relevant for quantum applications. Here, the Josephson effect is examined in more detail, justified by its key role in most superconducting quantum circuits. Finally, the experimental low-temperature setup employed in the presented experiments, the dilution refrigerator, is discussed.

## 2.1 Properties of superconductivity

In a superconducting material below a critical temperature $T_c$, the electrons experience an effective attraction, mediated by virtual phonons. This results in a two-electron bound state, the Cooper pairs, where the two constituents have an

opposing spin and momentum [BCS57]. The boson-like Cooper pairs themselves condense into a macroscopic wave function, often simplified as [BK12]

$$\Psi(\boldsymbol{r},t) = \sqrt{\rho(\boldsymbol{r},t)}\mathrm{e}^{\mathrm{i}\theta(\boldsymbol{r},t)}, \tag{2.1}$$

where the density $\rho$ and phase $\theta$ are generally position- and time-dependent. The pairing goes hand in hand with the formation of an energy gap $2\Delta(T)$ at the Fermi surface of the superconductor, which is proportional to the binding energy of a Cooper pair. In contrast to an insulator, global shifts of the Fermi sphere, where all Cooper pairs share the same momentum, are still allowed. This helps to illustrate the loss of resistance in superconductors: In a normal metal, the electrons on the Fermi surface can scatter inelastically, thereby relaxing the sphere back to the origin, where no mean current flows. In a superconductor, however, the bandgap provides a forbidden region for these processes. In this picture, paired electrons can only scatter around the Fermi sphere, such that no mean momentum is lost. This results in a lossless current, carried by the BCS condensate. Inelastic scattering is only possible if the energy transfer is sufficiently large to overcome the bandgap, which corresponds to breaking a Cooper pair. The intrinsic coherence of the wave function is crucial for macroscopic quantum systems based on superconducting circuits. The existence of an energy gap also implies that energy transitions of such a device should reside below the superconducting bandgap (typically on the order of $\sim 100\,\mathrm{GHz}$).

Another byproduct are quasiparticle excitations of the condensate. In a simplified picture, they can be imagined like hole and electron excitations in a semiconductor. Their energy is always larger than $\Delta$ and their charge continuously transitions from $-e$, far above, to $+e$, far below the energy gap. In contrast to the Cooper pairs, quasiparticles can scatter inelastically. Therefore, they impose a potential loss mechanism for quantum circuits, see Sec. 3.2.2 for additional information.

Other interesting properties include the Meissner-Ochsenfeld effect, describing the perfect diamagnetism up to a critical external magnetic field $H_\mathrm{c}$, the quantization of magnetic flux, most apparent in closed loops, Josephson junctions, and type-II superconductors, and of course the Josephson effect, discussed in the following section [GM12].

## 2.2 The Josephson effect

The Josephson effect is crucial for almost all superconducting quantum devices. It was first described theoretically by Brian Josephson in 1962 [Jos62], which later

awarded him the Nobel Price in Physics. The Josephson effect makes predictions about the current flow and voltage difference across a weak link, coupling the wave functions $\Psi_1$ and $\Psi_2$ of two adjacent superconductors, see Fig. 2.1. While Josephson derived the effect specifically for the superconducting phase, it can be shown that it is prevalent in other systems, for example, superfluid helium-4 [Suk+01]. The two Josephson equations read

$$\begin{aligned} I &= I_\mathrm{c} \sin\varphi, \\ \dot{\varphi} &= \frac{2\pi}{\Phi_0} V, \end{aligned} \tag{2.2}$$

where the flux quantum is given by $\Phi_0 = h/2e$, with the elementary charge $e$ and Planck's constant $h$. The gauge-invariant phase difference $\varphi$ across the weak link is defined as [BK12]

$$\varphi = \theta_2 - \theta_1 - \int_1^2 \boldsymbol{A} \mathrm{d}\boldsymbol{l}, \tag{2.3}$$

with the vector potential $\boldsymbol{A}$. The second Josephson equation predicts a time-dependent phase across the junction in response to an applied voltage and vice versa. Due to its high precision, this effect is used to define the (Josephson) voltage standard [BK12]. The first Josephson equation describes the flow of a lossless current $I$ up to a maximum value of $I_\mathrm{c}$ across the junction, as response to a phase difference across the weak link. Here, $I_\mathrm{c}$ can be inferred from the normal state resistance $R_\mathrm{n}$ of the contact from the Ambegaokar-Baratoff relation [AB63; BK12]

$$I_\mathrm{c} R_\mathrm{n} = \frac{\pi\Delta(T)}{2e} \tanh\left(\frac{\Delta(T)}{2k_\mathrm{B}T}\right) \approx \frac{\pi\Delta}{2e}, \tag{2.4}$$

with the Boltzmann constant $k_\mathrm{B}$. Experimentally, this is particularly useful in the pre-characterization of the critical current via a simple resistance measurement at room temperature, see Sec. 5.3.3.

The supercurrent $I$ across the junction is associated with the energy

$$E_\mathrm{J}(\varphi) = \int V I \mathrm{d}t = -E_\mathrm{J} \cos\varphi + \mathrm{const.}, \tag{2.5}$$

which is calculated using the Josephson equations, see Eq. (2.2). Herein, the Josephson energy is given by $E_\mathrm{J} = \Phi_0 I_\mathrm{c}/2\pi$. In the limit of small $\varphi$, the energy $E_\mathrm{J}(\varphi)$ is comparable to that of the magnetic energy stored in a conventional inductor with inductance $L_\mathrm{J} = \Phi_0/2\pi I_\mathrm{c}$, see Appendix B.

In the quantum limit, the gauge-invariant phase $\hat{\varphi}$ does not commute with the Cooper pair number operator $\hat{n}$ and [Dev97]

$$[\hat{\varphi}, \hat{n}] = \mathrm{i}. \tag{2.6}$$

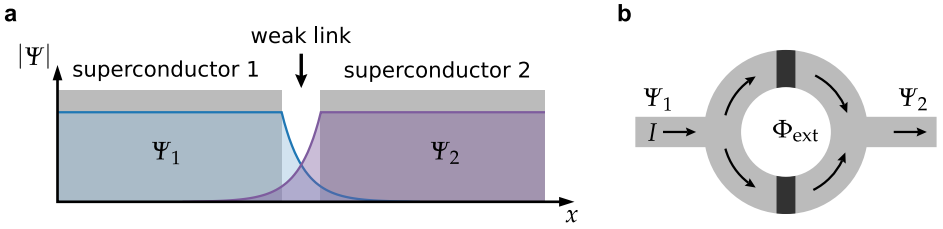


**Figure 2.1: Visualization of the Josephson weak link and SQUID.** (a) The wave functions $\Psi_1$ and $\Psi_2$ of the two superconducting slabs are coupled via a weak link. The resulting overlap of $\Psi_1$ and $\Psi_2$ enables coherent Cooper pair tunneling across the barrier, which is the underlying mechanism of the Josephson effect. Experimentally, the weak link is typically implemented with a superconductor-insulator-superconductor interface. (b) Sketch of a dc SQUID. Due to the interference of the superconducting wave function, the critical current across the SQUID can be adjusted by an external flux $\Phi_{\text{ext}}$.

Similar to the position and momentum of a particle, wave functions and operators can be expressed in either basis, with the transformation [Dev97]

$$|n\rangle = \frac{1}{2\pi}\int_0^{2\pi} \mathrm{e}^{-\mathrm{i}n\varphi}\,|\varphi\rangle\,\mathrm{d}\varphi. \tag{2.7}$$

In the charge basis, the Hamiltonian associated with $E_{\mathrm{J}}(\varphi)$ in Eq. (2.5) reads

$$\hat{H}_{\mathrm{J}} = \frac{E_{\mathrm{J}}}{2}\sum_{n=-\infty}^{\infty}\left(|n+1\rangle\langle n| + |n\rangle\langle n+1|\right). \tag{2.8}$$

This illustrates that the supercurrent is a result of coherent Cooper pair tunneling across the barrier.

In quantum devices, the non-linearity introduced by the Josephson effect is employed to isolate two energy levels of a circuit, usually ground and first excited state, which may then be used as logical quantum states for computation, see Sec. 3.4. Experimentally, Josephson junctions are typically implemented using a superconductor-insulator-superconductor interface. Therefore, the junction is naturally shunted by a capacitor. In this work, the intrinsic capacitance of the contact is always merged with that of parallel capacitors of the quantum circuit, unless stated otherwise.

## 2.3 The dc SQUID

In superconducting quantum interference devices (SQUIDs) a loop is used as an effective Mach-Zehnder interferometer for the superconducting wave function.

This becomes interesting when external magnetic flux can penetrate the loop by interrupting it with one or more Josephson junctions. For example, the dc SQUID comprises two Josephson junctions, one either side of the loop, which separate the wave functions on in- and output by weak links, see Fig. 2.1. For a negligible inductance of the loop and with equal critical currents $I_c$ of both junction, the total current $I$ and phase $\varphi$ across the device are connected by the equation

$$I = 2I_c \cos\left(\pi \frac{\Phi_{ext}}{\Phi_0}\right) \sin\left(\varphi + \pi \frac{\Phi_{ext}}{\Phi_0}\right). \tag{2.9}$$

This is similar to the behavior of a single junction, however, the effective critical current can be manipulated via the external magnetic flux $\Phi_{ext}$.

In many superconducting quantum devices, this effect is capitalized upon to enable in situ control over some of their properties, for example, the transition frequency of a qubit, see Sec. 3.4.2.

## 2.4 Dilution refrigerators

In the final section of this chapter the technical aspects of working with superconducting devices are discussed, that is, how to get them cold. Most metals employed for these quantum circuits transition to the superconducting phase at "moderately low" temperatures of few degree Kelvin, e..g., $\sim$ 1.2K for Aluminum[Phi59]. In order to reduce relaxation and decoherence due to thermal photons and quasiparticles, see Sec. 3.2, their operation regime lies significantly lower at around 20 mK. There are several commercially available types of refrigerators, which easily reach these temperatures on the timescale of several hours and maintain them for months at a time.

For superconducting quantum circuits, dilution refrigerators are most commonly used. The underlying cooling mechanism is based on the continuous endothermic dilution of mixtures of helium-3 and helium-4. Consequently, a pre-cooling down to $\sim$ 2 K, i.e., the transition temperature of liquid to superfluid helium-4, is required. Modern commercial dilution refrigerators utilize at least two stages of pulse tube coolers to reach these temperatures. The device employed in this work uses thermal baths of liquid nitrogen ($T_{LN_2} = 77\,K$) and helium-4 ($T_{L^4He} = 4.2\,K$), acting as heat sinks for the circulating gas. The helium bath is connected to the so-called 1 K pot. Here, a small volume of liquid is subjected to a low pressure generated by a rotary pump, resulting in evaporation cooling. Temperature and cooling power are adjusted by a sensitive valve, managing the flow from the helium bath.

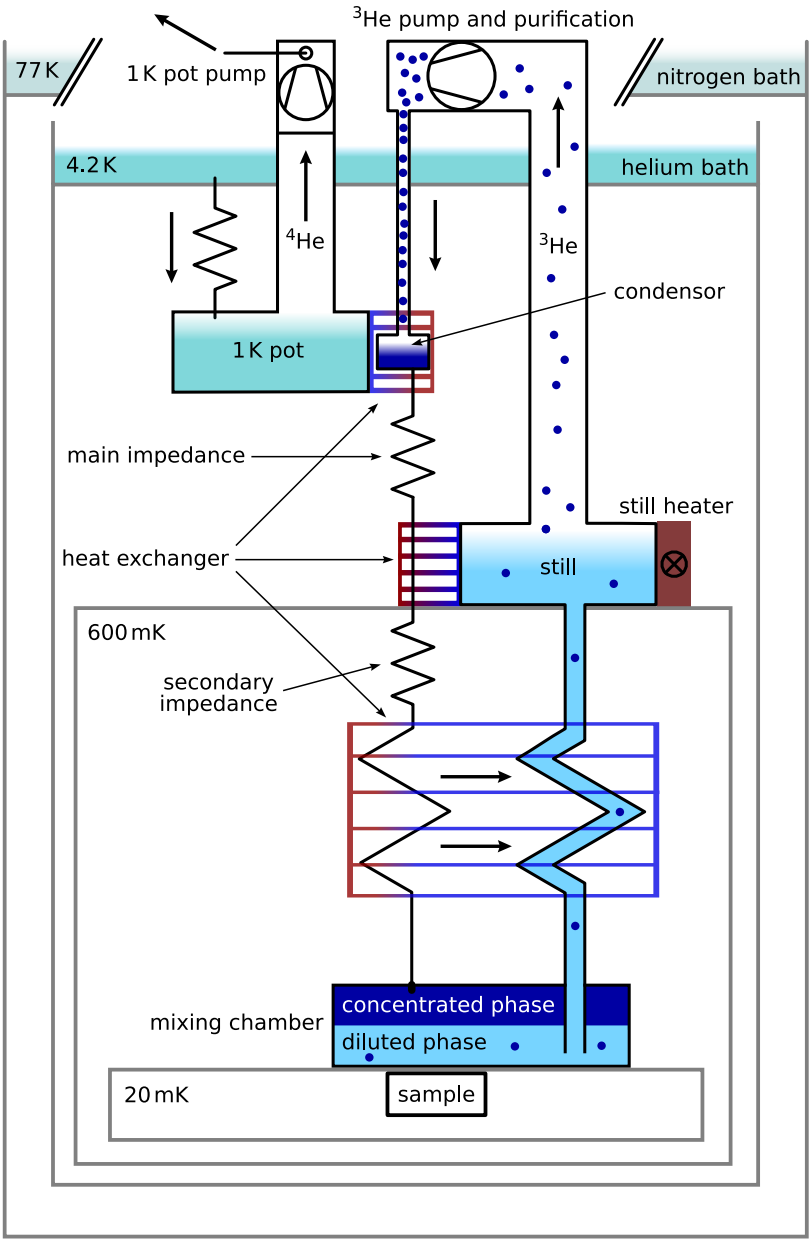


**Figure 2.2: Schematic diagram of a dilution refrigerator.** Helium-3 acts as the coolant and circulates through the cryostat in a closed cycle. It is pre-cooled by thermal baths of liquid nitrogen and helium, at the 1 K pot, at the still, as well as in a counter-current heat exchanger just ahead of the base stage. Here, in the mixing chamber, the main cooling mechanism comes into play: Helium-3 "evaporates" into the helium-4 rich phase, which results in a cooling of the mixture. Heat shields (gray) protect each stage from thermal radiation. Figure taken from Ref. [Sch20] with permission of S. Schlör.

Figure 2.2[1] shows a sketch of the cooling cycle [Sch20]. In operation mode, the mixing chamber gathers helium in a concentrated phase and a dilute phase, separated by a phase boundary. The helium-4 rich phase, composed of 93.4% superfluid helium-4 and $\sim$ 6.6% helium-3, extends up to the still. Here, at temperatures of $\sim$ 600mK, the partial pressure of helium-3 is greater than that of helium-4. By pumping on the still, helium-3 is distilled from the dilute phase, where the flow rate is adjusted by the still heater. The result is twofold: An osmotic pressure is created, leading to a net flow of helium-3 from mixing chamber to still. Additionally, the temperature of still is reduced by evaporation cooling. Before the gaseous helium-3 is cycled back into the cryostat, it is purified in a liquid nitrogen and helium cold trap. Subsequently, it is pre-cooled by the nitrogen and helium bath. It condenses to a liquid in a reservoir, thermally coupled to the 1 K pot. From here on, large flow impedances guide it back to the mixing chamber. On the way, a heat exchanger at still and a counter-current heat exchange with the helium-3 rising from the mixing chamber lead to additional cooling. At base, the helium-3 enters the mixing chamber into the concentrated phase, which is practically void of helium-4. As helium-3 is removed from the dilute phase through the still, additional helium-3 may traverse the phase boundary in the mixing chamber. Hereby, the entropy of the dilute phase increases, which, at constant heat, leads to a cooling of the mixture [EH05]. In this continuous operation mode, base temperatures of $10-20$ mK are achieved.

[1] Figure taken from Ref. [Sch20] with permission of S. Schlör.

# 3 Qubits and their environment

Quantum bits (qubits) are the central building blocks for quantum information processors. In contrast to their classical counterparts, they can be prepared in an arbitrary superposition of their two states. This allows for a massive parallelization during computation, enabling few ($\sim 50$) qubits to outperform classical supercomputers at selected tasks [Pre18]. Prominent examples are algorithms for integer factorization [Sho97] and database search [Gro96], however, currently the greatest interest is applications in quantum chemistry [Asp+05; Cao+19; McA+20].

Several platforms compete in the race for a quantum computer: trapped ion systems [CZ95; Mon+95; MK13] and qubits based on semi- [Col+01; Pet+05; Yon+18] or superconducting circuits [MSS01; Wen17; Kja+20] are the strongest candidates. In recent years, superconducting qubits seem to have taken the lead [Aru+19]. The micro-fabricated electrical circuits encoding the qubit states can be fabricated in large numbers [For+19b; Kre+20] and are just as easily coupled to each other [Kra+19; Kja+20]. This makes them appealing to construct quantum meta materials [ZFR16; Bre+21]. The surrounding circuits offer a tailored functionality of the quantum chip, which makes them particularly attractive for analog quantum simulation [GAN14; Bra+17; Lam+18].

This chapter comprises the basic mathematical tools needed to work with superconducting qubits. I start with a recapitulation of the platform-independent mathematical framework used to describe a qubit, including gate operations and the concept of energy relaxation and decoherence. In this context, I also briefly discuss the most relevant loss channels in superconducting qubits. This is followed by an introduction to circuit quantum electrodynamics with a focus on dispersive readout - the most widespread method for inferring the quantum state of a superconducting qubit. Finally, I give a brief description of arguably the most successful superconducting qubit architecture, also employed throughout this work: the transmon qubit.

## 3.1 Mathematical framework and operation

This section contains the mathematical tools to describe qubits from an arbitrary platform. We start with the Bloch sphere representation, followed by the implementation of single-qubit gates.

### 3.1.1 Qubit state representation

Independent of the physical realization of a qubit, the state of an arbitrary two-level system is mathematically represented by [Kra+19]

$$|\psi\rangle = \alpha\,|\mathrm{e}\rangle + \beta\,|\mathrm{g}\rangle\,, \tag{3.1}$$

where the state vector $|\psi\rangle$ is a superposition of the ground state $|\mathrm{g}\rangle$ and excited state $|\mathrm{e}\rangle$. The coefficients $\alpha$ and $\beta$ are complex numbers fulfilling

$$|\alpha|^2 + |\beta|^2 = 1, \tag{3.2}$$

such that $|\psi\rangle$ is normalized. A more convenient notation, obeying Eq. (3.2) by default, reads

$$|\psi\rangle = \cos\frac{\theta}{2}\,|\mathrm{e}\rangle + \mathrm{e}^{\mathrm{i}\phi}\sin\frac{\theta}{2}\,|\mathrm{g}\rangle\,. \tag{3.3}$$

Both notations are in principle equivalent, apart from a global phase, which can be omitted without loss of generality. An intuitive representation of Eq. (3.3) can be found by interpreting the two angles $\theta$ and $\phi$ as those of a spherical coordinate system. Every point on this so-called Bloch sphere corresponds to a quantum state and every state is unambiguously represented on the sphere, see Fig. 3.1.

Especially when working with gates, it is advantageous to express the qubit state in a vector notation, where

$$|\mathrm{e}\rangle = \begin{pmatrix}1\\0\end{pmatrix} \text{ and } |\mathrm{g}\rangle = \begin{pmatrix}0\\1\end{pmatrix}. \tag{3.4}$$

While it may seem counter-intuitive at first, states on opposing sites of the sphere are orthogonal, as is the case for $|\mathrm{g}\rangle$ and $|\mathrm{e}\rangle$. The choice of north and south pole as excited and ground state is arbitrary, however, it also determines the states pointing in $x$- and $y$-direction (if a right handed coordinate system is desired).

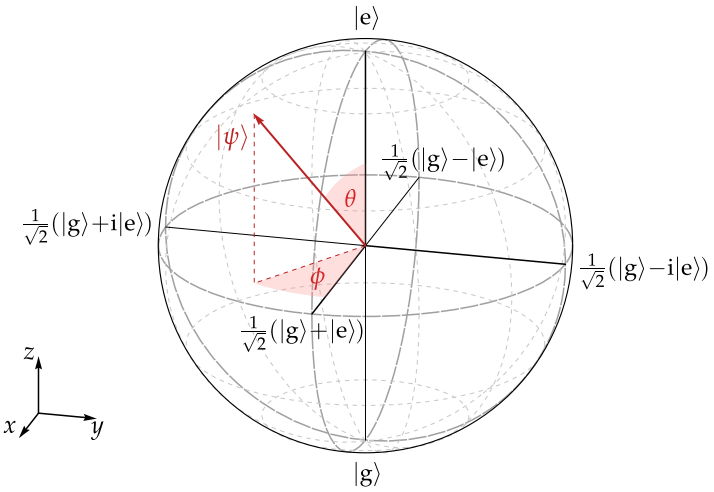


**Figure 3.1: Bloch sphere representation of a quantum state.** Each point on the Bloch sphere corresponds to a quantum state $|\psi\rangle$, unambiguously defined by the angles $\theta$ and $\phi$. Vectors in $x$-, $y$-, and $z$-direction are eigenvectors of the respective Pauli matrix.

### 3.1.2 Operating a qubit

Inspired by classical computing, operations performed on quantum bits are denoted as gates. As shown in the previous chapter, an arbitrary qubit state can be represented by a complex two-component vector. Naturally (i.e., due to its quantum nature), operations on the qubit can be represented by a two-dimensional Hermitian matrix [Kra+19]. Consequently, all qubit gates are reversible by their Hermitian conjugate. Likewise, multi-qubit gates are represented by $2^n$-dimensional matrices, where $n$ is the number of participating qubits. For both classical and quantum computation, a set of universal gates is needed to perform arbitrary computations. Classically, this means that any Boolean computation can be performed. For qubits, all conceivable superposition states need to be reachable by a combination of gates from a universal set [Kra+19]. In this section, we focus on the description of single-qubit gates, as all systems investigated in this work comprise only a single qubit.

#### Arbitrary rotations

Many single-qubit operations are denoted after the axis and angle of rotation on the Bloch sphere. For example, rotating a state by 180° around the $x$-axis is referred to as a $\pi_x$-pulse. Oftentimes, the angle denominator is omitted and may be interpreted

as a rotation around $x$, unless stated otherwise. Neglecting a global phase, arbitrary rotations of a state vector are performed by the operator [Lan17]:

$$\mathrm{e}^{-\mathrm{i}\frac{\alpha}{2}\boldsymbol{n}\hat{\boldsymbol{\sigma}}} = \mathbb{1}\cos\frac{\alpha}{2} - \mathrm{i}\boldsymbol{n}\hat{\boldsymbol{\sigma}}\sin\frac{\alpha}{2}, \tag{3.5}$$

where $\alpha$ is the angle of rotation, $\boldsymbol{n}$ is a (three-dimensional) normal vector around which a state is rotated, and $\hat{\boldsymbol{\sigma}} = \left(\hat{\sigma}_x, \hat{\sigma}_y, \hat{\sigma}_z\right)^\mathsf{T}$ is constituted from the Pauli matrices, which read:

$$\hat{\sigma}_x = \begin{pmatrix} 0 & 1 \\ 1 & 0 \end{pmatrix}, \quad \hat{\sigma}_y = \begin{pmatrix} 0 & -\mathrm{i} \\ \mathrm{i} & 0 \end{pmatrix}, \quad \hat{\sigma}_z = \begin{pmatrix} 1 & 0 \\ 0 & -1 \end{pmatrix}. \tag{3.6}$$

The Pauli matrices are the generators of rotations in the SU(2) vector space all state vectors reside in [Lan17]. Therefore, it is obvious that the vectors in $x$-, $y$-, and $z$-direction are eigenvectors of the Pauli matrices to eigenvalues $\pm 1$ (depending on their direction), e.g., $\hat{\sigma}_x\left(|\mathrm{g}\rangle \pm |\mathrm{e}\rangle\right) = \pm\left(|\mathrm{g}\rangle \pm |\mathrm{e}\rangle\right)$.[1]

**Frame of reference and $z$-rotation**

The Hamiltonian of a simple two-level system or qubit reads

$$\frac{\hat{H}_\mathrm{q}}{\hbar} = \frac{\omega_\mathrm{q}}{2}\hat{\sigma}_z. \tag{3.7}$$

Here, our choice of north and south pole proves advantageous, as it ensures that the excited state is energetically higher than the ground state while maintaining a right-handed coordinate system. The probability to find the qubit in the excited state is given by $n_\mathrm{q} = \frac{1}{2}(1 + \langle\hat{\sigma}_z\rangle)$, which is equal to the number of photons in the qubit, typically denoted as qubit population. Here, $\langle\hat{\sigma}_z\rangle$ is the expectation value of the $\hat{\sigma}_z$ operator.

From the Schrödinger equation, we find the time evolution operator $\hat{U} = \exp\left(-\mathrm{i}\omega_\mathrm{q} t\hat{\sigma}_z/2\right)$, which amounts to a continuous rotation around the $z$-axis at frequency $\omega_\mathrm{q}$ in the so-called laboratory frame of reference, i.e., a reference frame which is at rest. However, in a frame rotating at the frequency $\omega$, Eq. (3.7) reduces to

$$\frac{\hat{H}_\mathrm{q}}{\hbar} = \frac{\omega_\mathrm{q} - \omega}{2}\hat{\sigma}_z. \tag{3.8}$$

For more details on going into the rotating frame, see Appendix A. In the qubit frame of reference, that is, for $\omega = \omega_\mathrm{q}$, the time evolution operator is given by the

[1] Vector norm omitted for better readability

unit matrix and all states on the Bloch sphere are time-independent.[2] Herewith, it becomes clear that arbitrary state rotations around the $z$-axis are simply implemented by either changing the qubit frequency for a certain time or by offsetting the laboratory frame of reference.

Another implication is that uncontrolled variations of the qubit frequency lead to arbitrary rotations of the Bloch vector, causing a loss of phase information across multiple measurements, see Sec. 3.2 for details.

#### Rabi oscillations and *xy*-rotation

Experimentally, $x$- and $y$-rotations are often implemented using Rabi oscillations. The Hamiltonian of a qubit interacting with an oscillating photon field, e.g., a microwave tone or laser, reads [GKK05]

$$\frac{\hat{H}_{\text{Rabi}}}{\hbar} = \frac{\omega_{\text{q}}}{2}\hat{\sigma}_z + \Omega_0\hat{\sigma}_x\left(\hat{a}^\dagger \mathrm{e}^{\mathrm{i}\omega t} + \hat{a}\mathrm{e}^{-\mathrm{i}\omega t}\right), \tag{3.9}$$

where $\omega_{\text{q}}$ is the qubit frequency and $\Omega_0$ is the coupling strength between the qubit and the photon field, oscillating with the frequency $\omega$. Photons are created (annihilated) by the operator $\hat{a}^\dagger(\hat{a})$. In the rotating frame of the drive, Eq. (3.9) simplifies to

$$\frac{\hat{H}_{\text{Rabi}}}{\hbar} = \frac{\omega_{\text{q}} - \omega}{2}\hat{\sigma}_z + \Omega_0\left(\hat{\sigma}_+\mathrm{e}^{\mathrm{i}\omega t} + \hat{\sigma}_-\mathrm{e}^{\mathrm{i}\omega t}\right)\left(\hat{a}^\dagger\mathrm{e}^{\mathrm{i}\omega t} + \hat{a}\mathrm{e}^{-\mathrm{i}\omega t}\right). \tag{3.10}$$

Here, $\hat{\sigma}_\pm = (\hat{\sigma}_x \pm \mathrm{i}\hat{\sigma}_y)/2$ are related to the bosonic creation and annihilation operators, in the sense that they raise or reduce the eigenstates of $\sigma_z$, for example, $\hat{\sigma}_+ |\mathrm{g}\rangle = |\mathrm{e}\rangle$. In a rotating wave approximation, fast rotating terms with a frequency of $2\omega$ are neglected, which yields

$$\frac{\hat{H}_{\text{Rabi}}}{\hbar} \approx \frac{\delta}{2}\hat{\sigma}_z + \Omega_0\left(\hat{\sigma}_+\hat{a} + \hat{\sigma}_-\hat{a}^\dagger\right). \tag{3.11}$$

This approximation is valid for $\sqrt{N}\Omega_0 \ll \omega_{\text{q}}, \omega$. Here, the total photon number is given by $N = n_{\text{d}} + n_{\text{q}}$, where $n_{\text{d}} = \langle\hat{a}^\dagger\hat{a}\rangle$ is the photon number of the driving field. Taking a closer look at Eq. (3.11), it becomes clear that the total photon number is conserved and the Hamiltonian can be solved block-wise for constant $N$. In the

[2] This is obvious, as the operator for transforming into the rotating frame is simply the inverse time evolution operator.

basis $\{|n_q, n_d\rangle, |n_q - 1, n_d + 1\rangle\}$ and writing $\Omega = \sqrt{N}\Omega_0$, the $2 \times 2$ Hamiltonian reads

$$\frac{\hat{H}_N}{\hbar} = \begin{pmatrix} \frac{\delta}{2} & \Omega \\ \Omega & -\frac{\delta}{2} \end{pmatrix}. \tag{3.12}$$

Comparing with Eq. (3.5), the time evolution operator

$$\hat{U} = \exp\left(-\frac{i\hat{H}_N t}{\hbar}\right) = \exp\left(-i\frac{\Omega_R t}{2}\boldsymbol{n}\hat{\boldsymbol{\sigma}}\right) \tag{3.13}$$

is identified as a rotation around $\boldsymbol{n} = (2\Omega/\Omega_R, 0, \delta/\Omega_R)^T$ at the Rabi frequency

$$\Omega_R = \sqrt{\delta^2 + 4\Omega^2}. \tag{3.14}$$

With the qubit initially in the ground state, its time dependent population is given by [Rab37]

$$P_e(t) = \frac{1}{2}\left(1 - \left(\frac{\delta}{\Omega_R}\right)^2\right)(1 - \cos(\Omega_R t)), \tag{3.15}$$

Figure 3.2(a) displays the qubit population during these Rabi oscillations as a function of detuning and time. For large detuning, the Rabi frequency increases, and asymptotically approaches $\delta$, see Fig 3.2(b), which comes at the cost of a reduced oscillation amplitude.

Notably, for resonant driving ($\delta = 0$), Eq. (3.13) amounts to a rotation around the $x$-axis[3] at the Rabi frequency $\Omega_R = 2\Omega = 2\sqrt{N}\Omega_0$. As $\Omega_0$ is usually fixed by the experimental setup, qubit gates are defined by adjusting the duration $\Delta t$ and photon number of the driving field. For example, applying the field for a short time $\Delta t = \pi/2\Omega_R$ yields a $\pi_x$-pulse. Rotations around the $y$-axis are implemented similarly, by adding a $\pi/2$-phase shift to the driving field.

## 3.2 Real qubits and their dynamics

Previous discussions were limited to ideal qubits. Real systems, however, are prone to external perturbations [Kra+19]. Inevitably, this leads to a deterioration of the quantum state: spontaneous loss of the qubit excitation into various loss channels may occur and fluctuations of the qubit frequency destroy the phase information of superposition states. Here, we briefly describe how these effects are introduced mathematically to a quantum system and how energy loss and decoherence are determined experimentally. Finally, the most relevant sources of energy and coherence loss in superconducting qubits are discussed.

[3] In the qubit frame of reference

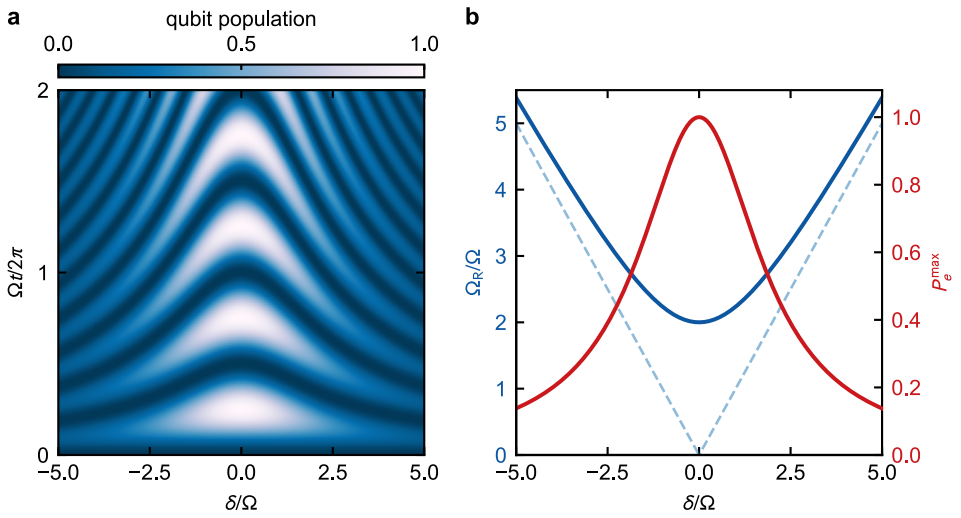


**Figure 3.2: Rabi oscillations induced by a photon field with drive strength $\Omega$.** (a) Qubit population as a function of time and detuning $\delta$ from the drive frequency, see Eq. (3.15). The population oscillates harmonically with time $t$. (b) Oscillation frequency $\Omega_\mathrm{R}$ (blue) and maximal excited state population $P_e^\mathrm{max}$ (red) depend strongly on $\delta$. For large detuning, $\Omega_\mathrm{R}$ asymptotically approaches $\delta$ (blue dashed line).

### 3.2.1 Time evolution of a Bloch vector

The time evolution of a real qubit is best captured by an ensemble, i.e., several identical, or a single system across multiple measurements. This statistical mixture, or mixed state, is encoded by the density operator [GKK05]

$$\hat{\rho} = \sum_{i,j} \rho_{ij} \left|\psi_i\right\rangle \left\langle\psi_j\right| , \tag{3.16}$$

where all $|\psi_i\rangle$ form an arbitrary orthonormal basis of the Hilbert space, and the components of $\hat{\rho}$ fulfill $\mathrm{Tr}(\hat{\rho}) = \sum_i \rho_{ii} = 1$. For a qubit, the density operator of an arbitrary mixed state reads

$$\rho = \begin{pmatrix} \rho_{11} & \rho_{10} \\ \rho_{10}^* & 1-\rho_{11} \end{pmatrix} = \frac{1}{2}\left(\mathbb{1} + \boldsymbol{m}\hat{\boldsymbol{\sigma}}\right) , \tag{3.17}$$

in the $\{|\mathrm{e}\rangle, |\mathrm{g}\rangle\}$ basis. In general, the vector $\boldsymbol{m}$ does not need to be normalized. In fact, for $|\boldsymbol{m}| = 1$, the density matrix belongs to a pure state, described by Eq. (3.3).

For an ideal system, the time dynamics of the density operator is given by the von Neumann equation [GKK05]

$$\frac{\partial}{\partial t}\hat{\rho} = -\frac{\mathrm{i}}{\hbar}\left[\hat{H}, \hat{\rho}\right], \tag{3.18}$$

which is inferred from Eq. (3.16) in conjunction with the Schrödinger equation. Introducing the effects of an arbitrary environment generally proves to be a difficult mathematical exercise. If the coupling between system and environment is sufficiently small and either frequency-independent or has a fixed frequency, the dynamics are described by the Lindblad equation in the form[Bal+19; Man20]

$$\frac{\partial}{\partial t}\hat{\rho} = -\frac{\mathrm{i}}{\hbar}\left[\hat{H}, \hat{\rho}\right] + \sum_i \hat{L}_i \hat{\rho} \hat{L}_i^\dagger - \frac{1}{2}\{\hat{L}_i^\dagger \hat{L}_i, \hat{\rho}\}, \tag{3.19}$$

with the anticommutator notation $\{\hat{a}, \hat{b}\} = \hat{a}\hat{b} + \hat{b}\hat{a}$. In Eq. (3.19), the environment is traced out and its effect on the original system is fully captured by the jump operators $\hat{L}_i$.

Neglecting thermal excitations of the quantum state, two mechanisms impair the performance of a two-level system: energy relaxation from excited to ground state and a variation of the qubit transition frequency, which leads to a loss of phase information across the ensemble. The jump operators for these processes are given by [Man20]

$$\hat{L}_1 = \sqrt{\Gamma_1}\hat{\sigma}_- \text{ and } \hat{L}_2 = \sqrt{\frac{\Gamma_\varphi}{2}}\hat{\sigma}_z, \tag{3.20}$$

with the energy relaxation rate $\Gamma_1$ and pure dephasing rate $\Gamma_2$. Inserting the definitions of the density matrix from Eq. (3.17), the jump operators from Eq. (3.20), and the single-qubit Hamiltonian from Eq. (3.8) into Eq. (3.19) yields

$$\frac{\partial \boldsymbol{m}}{\partial t}\hat{\boldsymbol{\sigma}} = -\Gamma_1 (1 + m_z)\hat{\sigma}_z - \left(\frac{\Gamma_1}{2} + \Gamma_\varphi\right)\left(m_x\hat{\sigma}_x + m_y\hat{\sigma}_y\right) + \delta\left(m_x\hat{\sigma}_y - m_y\hat{\sigma}_x\right) \tag{3.21}$$

for the equation of motion of the Bloch vector in a reference frame rotating at $\omega$, where $\delta = \omega_\mathrm{q} - \omega$. Since the Pauli matrices are linearly independent, the differential equation for $m_z$ can be separated. From Section 3.1.2 it is known that the qubit rotates around the $z$-axis at the frequency $\delta$ in the reference frame. This motivates the ansatz $(m_x, m_y) = m_\varphi(\cos(\delta t + \varphi_0), \sin(\delta t + \varphi_0))^\mathsf{T}$. Overall, this yields

$$\boldsymbol{m} = \begin{pmatrix} m_\varphi^0 \cos(\delta t + \varphi_0)\mathrm{e}^{-\Gamma_2^* t} \\ m_\varphi^0 \sin(\delta t + \varphi_0)\mathrm{e}^{-\Gamma_2^* t} \\ m_z^0 \mathrm{e}^{-\Gamma_1^* t} \end{pmatrix}, \tag{3.22}$$

for the time evolution of the Bloch vector $\boldsymbol{m}$, where $m_\varphi^0$, $m_z^0$, and $\varphi_0$ determine its initial state at $t = 0$. The dephasing rate is defined as $\Gamma_2^* = \Gamma_1/2 + \Gamma_\varphi$. Both, qubit

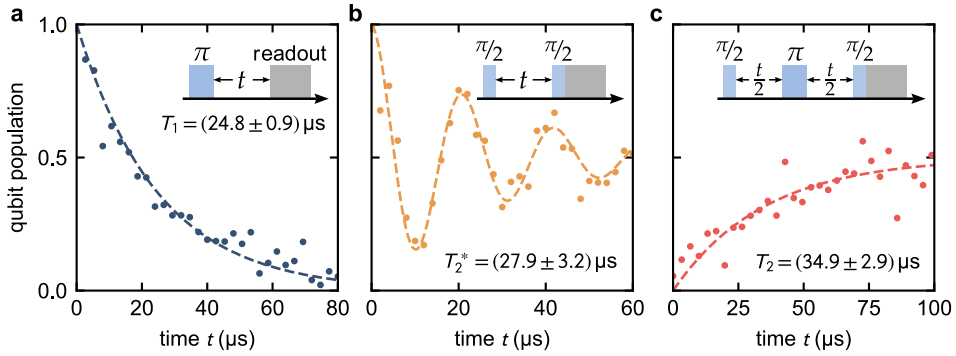


**Figure 3.3: Exemplary measurements of energy relaxation and decoherence times.** Measurement of a qubit's energy lifetime $T_1$ (a), Ramsey coherence time $T_2^*$ (b), and spin-echo coherence time $T_2$ (c). Insets show a schematic drawing of the gate sequences. The measurements were performed on the quantum device presented in [Ste+20], see Sec. 5.3.

energy (proportional to the $z$-component of the Bloch vector), and phase information decay exponentially on the timescales $T_1 = 1/\Gamma_1$ and $1/T_2^* = 1/2T_1 + 1/T_\varphi$, respectively, with $T_\varphi = 1/\Gamma_\varphi$. Apparently, the dephasing time is fundamentally limited by $T_2^* \leq 2T_1$.

On a final note, thermal excitation of an ensemble of two-level systems results, on average, in a finite excited state population. For a single qubit, the underlying quantum jumps (which are actually coherent Rabi transitions [Min+19]) between $|g\rangle$ and $|e\rangle$ can be tracked to infer the rates of spontaneous emission and thermal excitation [VSS11].

### 3.2.2 Measuring characteristic timescales

Due to the quantum nature of qubits, only a projection of the state vector can be measured. This is usually referred to as qubit state readout. Reconstructing the whole trajectory of a Bloch vector requires a projection of all three components across consecutive measurements [Kat+06; Ste+06; Kra+19]. However, the characteristic time scales for energy loss and decoherence can be extracted in more basic experiments.

Figure 3.3 displays the three most common measurements, at the example of a superconducting qubit. Here, the projection axis coincides with the $z$-axis of the Bloch sphere. Consequently, a ***$T_1$*-measurement** of the (energy) lifetime boils down to preparing the qubit in the excited state and projecting at various times $t$ across several measurements, see Fig. 3.3(a).

Information on the coherence time $T_2^*$ can only be inferred from Bloch vectors with components in $x$-, or $y$-direction. In a **Ramsey measurement**, the qubit is prepared on the equator of the Bloch sphere, using a $\pi/2$-pulse. After free evolution for a certain time $t$, another $\pi/2$ rotation about the same axis is performed. In the qubit frame, i.e., for $\delta = 0$ in Eq. (3.22), this yields exponential decay with a time constant $T_2^*$ down to half population. If the drive is slightly detuned from the qubit frequency, the rotation around the $z$-axis at $\delta$ corresponds to a sinusoidal oscillation of the qubit population after the second $\pi/2$-pulse. Experimentally, this is advantageous, as the qubit frequency can be inferred from the oscillations with high accuracy and the baseline for fitting the measurement signal is fixed, see Fig. 3.3(b).

Figure 3.3(c) displays a **spin-echo experiment**. Compared to a Ramsey measurement, an additional $\pi$-pulse (around an arbitrary equatorial axis) is inserted in between the $\pi/2$-pulses. The "echo"-pulse flips the state vectors in the measurement ensemble around the $x$-axis, changing the direction of rotation around the $z$-axis. Herewith, low-frequency noise, i.e., variations of the qubit frequency slower than the measurement time, is eliminated, as the state vectors constituting mixed state re-phase. Therefore, the timescale $T_2$ at which the qubit population decays is usually greater than $T_2^*$, however, is still limited by $2T_1$.

Finally, as discussed in the previous section, an exponential decay of energy or coherence only holds if the corresponding loss channel is frequency-independent or has contributions at only one frequency.

### 3.2.3 Sources of noise and decoherence in superconducting qubits

Whether a certain loss channel leads to energy relaxation or dephasing is determined by the coupling mechanism to the qubit. Longitudinal coupling ($\hat{\sigma}_z$-type) results in dephasing, transverse coupling ($\hat{\sigma}_{x,y}$-type) reduces the energy lifetime. Superconducting qubits are macroscopic objects made up of a combination of capacitors, inductors, and Josephson junctions or SQUIDs. The coupling type to external perturbations crucially depends on the arrangement of these components. In fact, most modern qubit architectures are designed to specifically suppress the influence of certain loss channels [Koc+07; Man+09; Yan+16; Gye+19]. Over the past two decades, significant and ongoing efforts were directed at improving qubit life-, and coherence times. Here, we touch on some of the most relevant loss mechanisms in superconducting circuits - and ways to circumvent them.

In small capacitors, fluctuations of local charges can lead to drastic changes in the associated charging energy. This **charge noise** may be avoided by increasing the capacitor size, as was done for the transmon qubit [Koc+07], see Sec. 3.4, or C-shunted flux qubit [Yan+16].

Josephson junctions and especially SQUIDs are prone to variations of the external magnetic field, altering the Josephson energy. Among others, this **flux noise** can be caused by current noise in the tuning coil or even flipping of microscopic surface spins [Bra+20]. Therefore, careful filtering of all flux bias lines is needed. The effects of surface spins may be mitigated by surface treatment [Kum+16].

Another noise channel is provided by **quasiparticle excitations** of the superconducting condensate tunneling across a Josephson junction [Mar+05; Cat+11; Cat+12]. This is particularly relevant for low gap superconductors like Aluminum used in the junction of almost all state of the art qubits. An architecture with suppressed quasiparticle tunneling is the fluxonium qubit (biased to its flux sweet spot) [Pop+14]. Moreover, direct and indirect trapping of quasiparticles, for example, using metallic traps, is heavily investigated [Wan+14; Riw+16; RC19; Hen+19].

Many, if not all, superconducting quantum circuits are hosts to parasitic **two-level-systems** (TLS), which interact via their electric dipole moment [Gra+12; MCL19]. Especially inside the junction, TLS greatly impair qubit performance [Sim+04; Mar+05; Sch+19; Bur+19]. While the influence of TLS on surfaces and interfaces is smaller, it may be one of the main limiting factors for current superconducting qubits [Bil+20]. Reducing the electrical field on the qubit surface, as well as a meticulous fabrication of the circuit [Dun+17; Gam+17; Ner+19] and surface treatment [Kum+16; Gra+17] can help to mitigate this effect. Additionally, there is an ongoing quest for materials less prone to forming TLS [Vis+13; McR+20; Pla+20].

In circuit and cavity quantum electrodynamics (cQED/CQED) systems, qubits are coupled to at least one bosonic mode, usually serving as a tool for state readout [Bla+04; Wal+04], see Sec. 3.3 for additional information. The resonator itself is coupled to the continuous and broad spectrum of a transmission line. Especially for strong qubit resonator coupling, energy relaxation of the qubit into the transmission line via the resonator is enhanced [EDM86]. This **Purcell loss** [PTP46] is discussed in more detail in Sec. 3.3.2 and 4.3.4. Similarly, direct coupling to the mode spectrum of a transmission line, e.g., employed as a port to drive gates, leads to an enhanced energy decay rates, see Sec. 4.4.3. Overall, proper attenuation and thermalization of all lines going to and coming from a cQED setup is crucial. Populating a readout resonator with thermal photons can lead to additional dephasing, see Sec. 3.3.1, as does direct irradiation of the qubit.

On a final note, noise is generally frequency-dependent, also in superconducting circuits. The study of the noise power spectral density is a vital tool for understanding and ultimately mitigating or eliminating sources of decoherence [Kra+19].

## 3.3 Circuit quantum electrodynamics

In circuit quantum electrodynamics (cQED), a bosonic mode is coherently coupled to a two-level system. From an academic point of view, these artificial systems are interesting study subjects, as they map directly on light-matter interaction [Bra+17; Sch+18; Kri+20; Wol+20]. In quantum engineering, the harmonic oscillators are repurposed for qubit state readout [Bla+04; Wal+04]. Dispersive readout of the qubit state can achieve readout fidelities around $\sim 87\%$ [Ree+10]. This is further improved in conjunction with superconducting amplifiers [Aum20], operating near the quantum limit of added noise [Roc+12; Mac+15; Win+20]. Additionally, dispersive readout is a non-demolition measurement, that is, the qubit does not escape the computational basis due to the readout, but rather remains in the state it is projected to by the measurement. While slight modifications may be needed, dispersive readout is applicable to all (current) superconducting qubit architectures, such as the transmon, see Sec. 3.4, used throughout this work.

### 3.3.1 Jaynes–Cummings model and dispersive readout

The Jaynes-Cummings model describes the interaction of a bosonic mode with a two-level system and therefore is ubiquitous in nature - and cQED. The Jaynes-Cummings Hamiltonian reads [GKK05]

$$\frac{\hat{H}_{\mathrm{JC}}}{\hbar} = \frac{\omega_{\mathrm{q}}}{2}\hat{\sigma}_z + \omega_{\mathrm{r}}\hat{a}^\dagger\hat{a} + g\left(\hat{\sigma}_-\hat{a}^\dagger + \hat{\sigma}_+\hat{a}\right), \tag{3.23}$$

where a rotating wave approximation was already applied and is valid for $\sqrt{N}g \ll \omega_{\mathrm{q}}, \omega_{\mathrm{r}}$, with the total photon number $N = n_{\mathrm{q}} + n_{\mathrm{r}}$. Here, $g$ is the coupling strength between the qubit and bosonic mode. It is not surprising that this Hamiltonian is practically identical to that of the Rabi model introduced in Eq. (3.11), which also describes light-matter interaction. In contrast to Sec. 3.1.2, we are now interested in the energy dispersion of the system rather than its time evolution. Once again, in the basis $\{|n_{\mathrm{q}}, n_{\mathrm{r}}\rangle, |n_{\mathrm{q}} - 1, n_{\mathrm{r}} + 1\rangle\}$ of constant $N$, the Hamiltonian

$$\frac{\hat{H}_N}{\hbar} = \begin{pmatrix} \omega_{\mathrm{q}} + (N-1)\,\omega_r & \sqrt{N}g \\ \sqrt{N}g & N\omega_r \end{pmatrix}. \tag{3.24}$$

can be solved block-wise. Introducing the detuning as $\delta = \omega_q - \omega_r$, its energy eigenvalues read

$$\frac{E_N^{\pm}}{\hbar} = N\omega_r + \frac{\delta}{2} \pm \sqrt{\left(\frac{\delta}{2}\right)^2 + Ng^2}, \tag{3.25}$$

$$E_0 = 0, \tag{3.26}$$

For small detuning, the coupling between bosonic mode and qubit leads to an avoided level crossing and strong hybridization of the participating quantum states of each photon manifold. For tunable qubits, Eq. (3.25) can be used to experimentally extract the coupling strength from the dispersion, see Fig. 3.4(a). Especially for $\delta = 0$, the two states are fully hybridized and their energy spitting is given by $(E_N^+ - E_N^-)/\hbar = 2\sqrt{N}g$. Qubit readout is typically performed in the dispersive regime where $2\sqrt{N}g/\delta \ll 1$ [Bla+04]. Here, Eq. (3.25) can be approximated as

$$\frac{E_{n_q,n_r}}{\hbar} \approx n_q\left(\omega_q + \frac{g^2}{\delta}\right) + n_r\omega_r + (2n_q - 1)n_r\frac{g^2}{\delta} \tag{3.27}$$

which corresponds to the Hamiltonian [Bla+04]

$$\frac{\hat{H}_{\text{disp}}}{\hbar} = \frac{\tilde{\omega}_q}{2}\sigma_z + \omega_r\hat{a}^\dagger\hat{a} + \chi\sigma_z\hat{a}^\dagger\hat{a}. \tag{3.28}$$

The qubit frequency $\tilde{\omega}_q = \omega_q + \chi$ is "dressed" by the presence of the bosonic mode, with

$$\chi = \frac{g^2}{\delta}. \tag{3.29}$$

Figure 3.4(b) displays a sketch of the energy diagram in the dispersive regime for $\omega_r > \omega_q$. The frequency of both qubit and bosonic mode are mutually dependent on the number of photons in the other system. Consequently, measuring the transition frequency of the oscillator is equivalent to a projective measurement of the qubit state, i.e., qubit state readout. In the experiment, this is only possible in the strong coupling regime, where $g > \Gamma_1, \kappa$ [Bla+04] with the qubit and resonator decay rates $\Gamma_1$ and $\kappa$. For increasing drive power, the oscillator decouples from the qubit, see Sec. 3.4.3.

On the other hand, measuring the qubit transition frequency projects the photon number of the oscillator and its state can be inferred [Sch+07]. An exemplary measurement is displayed in Fig. 3.4(c). By continuous driving of a lossy bosonic mode we, naturally, prepare it in an eigenstate $|\alpha\rangle$ of the annihilation operator with $\hat{a}|\alpha\rangle = \alpha|\alpha\rangle$, typically referred to as a coherent state. In the basis of the oscillators Fock states $|n\rangle$, the coherent state reads [GKK05]

$$|\alpha\rangle = e^{-\frac{|\alpha|^2}{2}} \sum_{n=0}^{\infty} \frac{\alpha^n}{\sqrt{n!}} |n\rangle . \tag{3.30}$$

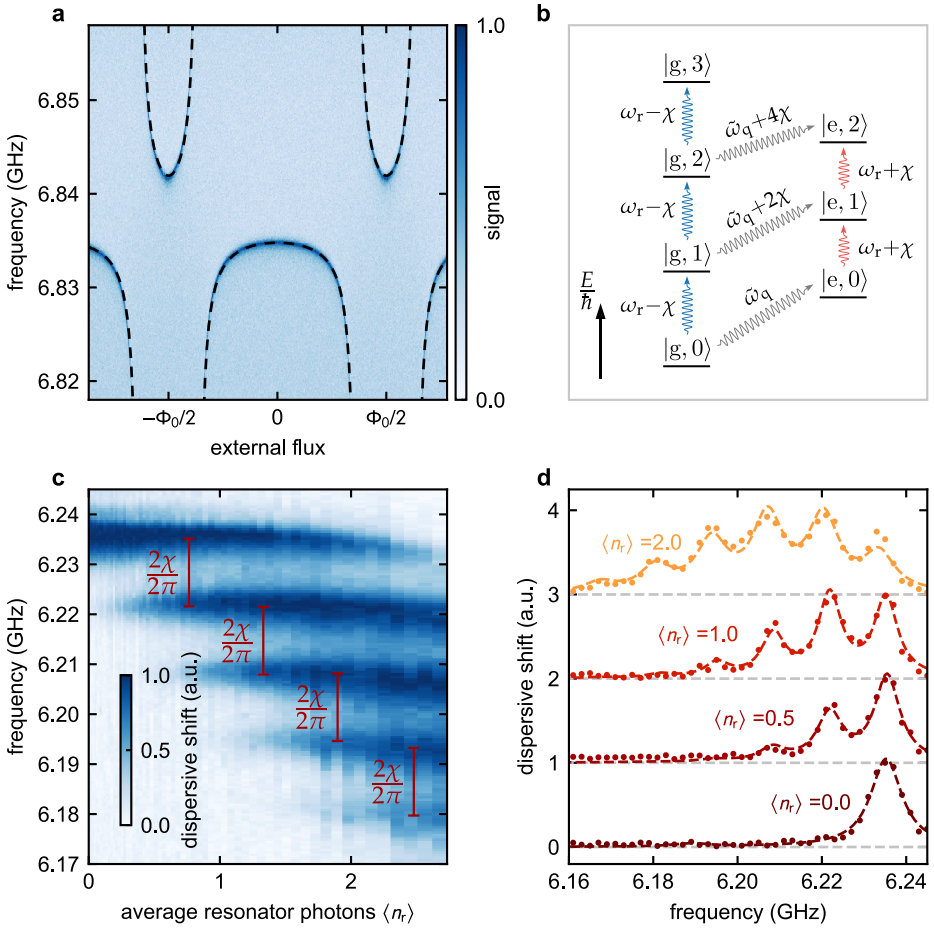


**Figure 3.4: Frequency spectrum and dispersive shift in the Jaynes-Cummings model.** (a) Frequency spectrum of a microwave resonator coupled to a transmon qubit for small detuning $\delta = \omega_q - \omega_r$ and in the single-photon manifold. Following Eq. (3.38), we tune the transmon's frequency by applying an external flux, which results in several avoided level crossings with the resonator. On resonance, qubit and resonator are fully hybridized with a level splitting of $(E_1^+ - E_1^-)/\hbar = 2g$. (b) Schematic energy diagram of the Jaynes-Cummings model in the dispersive regime for $\omega_q < \omega_r$, thus, $\chi < 0$. Depending on the qubit state, the frequency of the bosonic mode is red or blue shifted. The qubit frequency depends on the number of photons in the harmonic mode. (c) Qubit spectrum with the resonator prepared in a coherent state with average photon number $\langle n_r \rangle$. Each peak corresponds to a Fock state, where neighboring peaks are separated by $2\chi/2\pi = (13.7 \pm 0.4)$ MHz. The resonator has a frequency of $\omega_r/2\pi = 6.860$ GHz. (d) The Fock states follow a Poisson distribution, see Eq. (3.30). From a fit (dashed lines) we extract $\langle n_r \rangle$. Neighboring traces are offset by 1 to improve visibility.

Here, $n$ is Poisson distributed, with an average photon number $\langle n_\mathrm{r}\rangle = |\alpha|^2$. Owed to the dispersive shift, this distribution is captured by the qubit spectrum, with a peak separation of $2\chi$, see Fig. 3.4(d). Experimentally, this provides a unique method to calibrate incident drive power at the oscillator.

### 3.3.2 Purcell loss

One drawback of cQED architectures is the introduction of Purcell loss. The bosonic mode used for qubit state readout inevitably has to be coupled to the environment, i.e., the continuous mode spectrum of the vacuum or a transmission line, see Sec. 4.1. Therefore, even in the absence of intrinsic loss channels (which most physical systems are prone to), the resonator has a finite decay rate $\kappa$, see Sec. 4.3 for details. Consequently, a dressed qubit can decay into the environment seen through the bosonic mode. In the simplest case where the oscillator couples directly to a continuous mode spectrum, this can be interpreted as the decay of the resonator's contribution to the dressed qubit state $|\tilde{\mathrm{e}}\rangle$, with rate $\kappa$. For the Hamiltonian in Eq. (3.24), first order perturbation theory predicts a Purcell rate of [Bla+04]

$$\Gamma_\mathrm{P} = \kappa |\langle \mathrm{g}, 1|\tilde{\mathrm{e}}\rangle|^2 = \kappa \left(\frac{g}{\delta}\right)^2, \tag{3.31}$$

contributing to the total energy relaxation rate.

In modern cQED architectures, the additional contribution to the decay rate is addressed with Purcell filters, see Sec 4.3.4. Here, the bosonic mode used for qubit state readout is coupled to a broadband (high $\kappa$) oscillator, rather than directly to a transmission line. As a result, the environment seen by the qubit is reduced to the spectrum of the Purcell filter [Jef+14; SMK15]. This is particularly efficient when the qubit is far detuned from the filter. Of course, the readout mode has to be on (or close to) resonance with the filter to retain its coupling to the environment, needed for dispersive qubit state readout.

## 3.4 The transmon qubit

The transmon qubit [Koc+07] has been adapted by global players such as Google [Bar+13] and IBM [McK+16] in their effort to build a universal quantum computer. Therefore, it is one of the most successful qubit implementations across all platforms. One reason for this stellar success is its simplicity - it is made up of a capacitor and a Josephson junction, or SQUID for the tunable version. Consequently, the transmon is also a good platform to study sources of decoherence and find

ways to eliminate them. Recent optimizations of the electrode material have led to record-breaking coherence times around 300 µs [Pla+20], which is on the order of several thousand qubit gates [Kja+20]. Nevertheless, the transmon has certain drawbacks, i.e., its large size and low anharmonicity, which may ultimately lead to its replacement by other superconducting qubit architectures.

The transmon qubit is also used in this work. Therefore, this section is aimed at providing a basic understanding of the transmon qubit's working principle and, thereby, its perks and perils. Equations and explanations in this section are inspired by the work of Koch *et al.* [Koc+07], where the concept of the transmon qubit was established theoretically.

### 3.4.1 Mathematical treatment and relation to the harmonic oscillator

The transmon qubit is assembled from a capacitor and a Josephson junction. Using circuit quantization, see Sec. 4.4.1, its Hamiltonian is derived as [Koc+07]

$$\hat{H} = 4E_{\mathrm{C}}\hat{n}^2 - E_{\mathrm{J}}\cos\hat{\varphi}. \tag{3.32}$$

Here, the charge number $\hat{n}$ and phase operator $\hat{\varphi}$ do not commute, see Eq. (2.6). The charging energy $E_{\mathrm{C}} = e^2/2C_{\mathrm{q}}$ is associated with a single charge $e$ on the capacitor with capacitance $C_{\mathrm{q}}$ and $E_{\mathrm{J}}$ is the Josephson energy, see Sec. 2.2 for details. Overall, this can be understood as a virtual particle interacting with a cosine potential, where the particle mass is proportional to $C_{\mathrm{q}}$. An extreme case is the so-called "transmon limit", where the charging energy is much smaller than the Josephson energy, typically, $E_{\mathrm{J}}/E_{\mathrm{C}} > 30$. In this regime, the virtual particle is trapped at the bottom of the cosine potential

$$\cos\hat{\varphi} = 1 + \frac{\hat{\varphi}^2}{2} - \frac{\hat{\varphi}^4}{24} + \mathcal{O}\left(\hat{\varphi}^6\right), \tag{3.33}$$

and higher orders $\mathcal{O}\left(\hat{\varphi}^6\right)$ can be neglected. Apart from a constant energy offset, equation (3.32) may be rewritten as

$$\hat{H} \approx 4E_{\mathrm{C}}\hat{n}^2 + \frac{E_{\mathrm{J}}}{2}\left(\hat{\varphi}^2 - \frac{\hat{\varphi}^4}{12}\right), \tag{3.34}$$

which bears a striking resemblance to the quantum mechanical harmonic oscillator, see Appendix B, where the inductor is replaced by the Josephson inductance

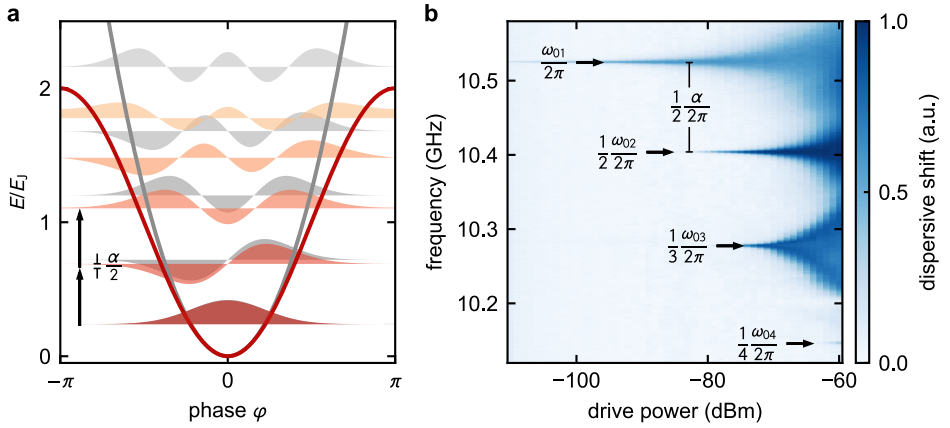


**Figure 3.5: Energy eigenvalues, eigenstates, and transitions of the transmon qubit.** (a) Harmonic oscillator (gray) and transmon qubit potentials (red) as a function of the phase. Shaded areas indicate the (real part of the) wave functions of the oscillator (light gray) and transmon (light red). The transmon potential flattens towards higher energies, shifting its eigenstates to lower energies compared to their counterpart in the harmonic oscillator, with a greater effect for higher states. Consequently, the degeneracy of the transition frequency is lifted, allowing for a selective excitation of the eigenstates. The difference between $\omega_{01}$ and $\omega_{12}$ is denoted as anharmonicity $\alpha$. (b) Measurement of a transmon qubit's transition frequencies. At greater drive power, i.e., larger number of photons, multi-photon transitions become possible (indicated by black arrows in (a)). Their frequency is given by $\omega_{0n}/n$, where $n$ is the state number and number of photons needed to drive the transition. Using Eq. (3.37), the anharmonicity of this particular device is extracted as $\alpha/2\pi = -241\,\mathrm{MHz}$.

$L_\mathrm{J} = \Phi_0/2\pi I_\mathrm{c}$. It is intuitive to rewrite the Hamiltonian in Eq. (3.34) in the basis of the harmonic annihilation and creation operators, which read

$$\hat{b} = \left(\frac{E_\mathrm{J}}{32E_\mathrm{C}}\right)^{\frac{1}{4}} \left(\hat{n} + \mathrm{i}\left(\frac{8E_\mathrm{C}}{E_\mathrm{J}}\right)^{\frac{1}{2}} \hat{\varphi}\right). \tag{3.35}$$

It can be shown that terms which do not conserve photon number may be neglected. This yields

$$\hat{H} = \sqrt{8E_\mathrm{J}E_\mathrm{C}}\hat{b}^\dagger\hat{b} - \frac{E_\mathrm{C}}{2}\left(\left(\hat{b}^\dagger\hat{b}\right)^2 + \hat{b}^\dagger\hat{b}\right), \tag{3.36}$$

Figure 3.5(a) displays the (exact) energy eigenvalues and eigenstates of the transmon in comparison to those of the harmonic oscillator. The most apparent distinction to the harmonic oscillator is the loss of degeneracy of the transition frequency, see Fig. 3.5(b) for a measurement of the transmon's spectrum. Typically this is labeled as a qubit's anharmonicity, and is defined as

$$\alpha = \omega_{12} - \omega_{01} = \omega_{02} - 2\omega_{01} \approx -E_\mathrm{C}/\hbar, \tag{3.37}$$

where $\omega_{ij}$ is the transition frequency from state $i$ to $j$. The approximation holds for $E_J/E_C \gtrsim 20$. In fact, $\alpha$ is always smaller than $-E_C$ in this regime.

This loss of degeneracy is a crucial feature for systems operated as qubits, as it allows for a systematic state preparation, i.e., the implementation of gate operations, see Section 3.1.2. Evidently, the anharmonicity reduces with increasing capacitance: As the virtual particle's mass increases, it is trapped deeper inside the cosine potential. Here, higher orders of the Tailor expansion play a minor role and the Hamiltonian asymptotically approaches that of the harmonic oscillator.

Generally, a larger anharmonicity reduces gate errors and allows for faster qubit control [Kja+20]. However, a large capacitance is advantageous for one simple reason: superior qubit coherence. This becomes clear when comparing even some of the earliest transmons [Hou+07; Sch+08] with charge qubits, which essentially share the same Hamiltonian. Due to the charge qubit's small capacitance, even slight fluctuations in the local charge environment have great effects on the qubit frequency, drastically impairing its phase coherence. In the transmon, the sensitivity to charge is suppressed exponentially with $\sim \exp\left(\sqrt{8E_J/E_C}\right)$ [Koc+07]. Additionally, the large metallic electrodes of the capacitor allow for a dilution of the electric fields of the qubit. In contrast, the capacitance of the charge qubit is only given by the capacitance of its Josephson junction. As was described in more detail in Section 3.2.3, this also reduces the transmon's coupling to two-level systems, which seem to be one of the main limiting factors for the coherence of modern qubits [MCL19].

### 3.4.2 Tunability

Achieving tunability for a transmon qubit is just as straightforward as building a single transmon qubit. In Section 2.3, the working principle of a dc SQUID was discussed. By replacing the single Josephson junction of the transmon with this device, the Josephson energy can be controlled in situ by applying an external magnetic field. Mathematically, this is expressed as

$$E_{J,\,\mathrm{tot}} = (E_{J1} + E_{J2}) \left|\cos\left(\frac{\pi\Phi_{\mathrm{ext}}}{\Phi_0}\right)\right| \sqrt{1 + d^2 \tan^2\left(\frac{\pi\Phi_{\mathrm{ext}}}{\Phi_0}\right)}, \tag{3.38}$$

see [Koc+07] for a proper derivation. Here, $E_{J1}$ ($E_{J2}$) is the Josephson energy of the first (second) SQUID junction. The asymmetry of the SQUID is captured in the coefficient $d = (E_{J1} - E_{J2}) / (E_{J1} + E_{J2})$, which is typically on the order of 1-30%, depending on the junction fabrication, see Sec. 5.3. By varying the external flux

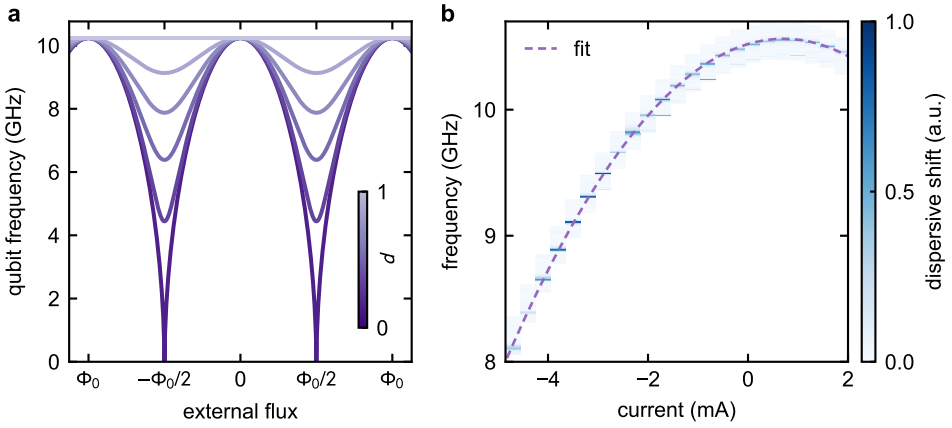


**Figure 3.6: Qubit transition frequency as a function of external flux.** By applying flux through the SQUID loop of a transmon qubit, its frequency is tuned. This comes at the cost of additional flux noise, reducing the qubit's coherence time. (a) Qubit dispersion as a function of external flux and the asymmetry parameter $d = (E_{J1} - E_{J2}) / (E_{J1} + E_{J2})$. A second sweet spot can be engineered by increasing the asymmetry of the SQUID while maintaining the same total Josephson energy. (b) Measurement of a transmon qubit's dispersion. Applying a current to an on-chip magnetic coil generates the flux needed to tune the qubit frequency. Already without externally applied flux, the dispersion is slightly offset towards positive currents. This is a result of stray flux coupling into the SQUID loop. Around the sweet spot, the dispersion is well-approximated by a parabola (see blue dashed line).

$\Phi_{\text{ext}}$, the Josephson energy and thereby the qubit frequency can be changed over the range of several GHz, see Fig. 3.6.

An obvious drawback of tunable, compared to fixed frequency qubits, is a stronger coupling to flux noise, see Sec. 3.2.3. The longitudinal coupling to external flux (and thus flux noise) leads to increased dephasing rates and reduced qubit coherence times. The magnitude of this effect is proportional to the flux derivative of the qubit dispersion $\partial\omega_{01}/\partial\Phi_{\text{ext}}$ [Kra+19]. A steeper dispersion results in greater variations of the qubit frequency and thus stronger dephasing. This gives rise to a sweet spot at $\Phi_{\text{ext}} = 0$, where the derivative, and thereby the flux noise, vanishes. Additionally, a second (energetically lower) sweet spot can be engineered at $\Phi_{\text{ext}} = \Phi_0/2$ by systematically adding a junction asymmetry [Hut+17], see Fig. 3.6. Here, good control over the fabrication, particularly, a low spread of the Josephson junctions' critical current, is needed.

In this work, tunability of the qubit is vital for the realization of the analog quantum simulator of the Landau-Zener model.

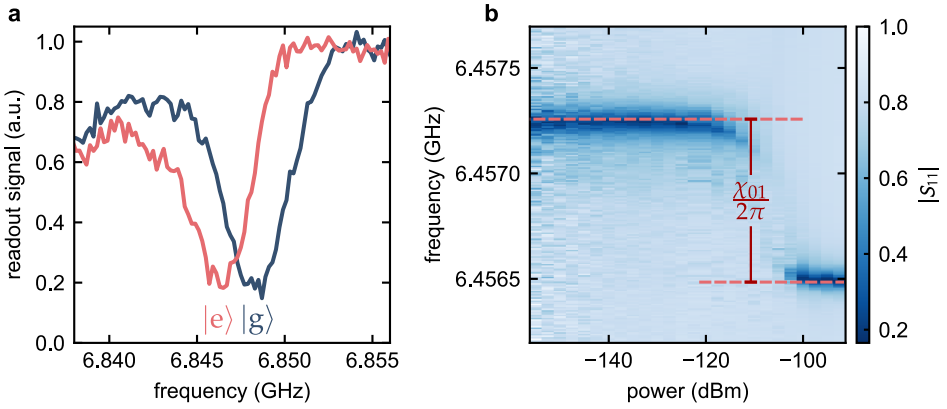


**Figure 3.7: Bosonic mode for state readout.** (a) Readout of a transmon qubit. The frequency of the oscillator changes depending on the qubit state. Therefore, the reflected amplitude of a fixed-frequency signal applied to the oscillator gives information on the qubit population. (b) Power dependence of the amplitude $|S_{11}|$ of a signal reflected on the readout mode. For large input power, qubit and oscillator decouple and the states are no longer dressed. The shift $\chi_{01}$ of the readout mode can be used to extract the coupling strength to the qubit.

### 3.4.3 Modification of the dispersive readout

Owed to the multi-level structure of the transmon qubit, the dispersive shift in a Jaynes-Cummings system is modified. The higher levels of the transmon also couple to the bosonic mode, effectively reducing the dispersive shift to [Koc+07]

$$\chi = \alpha \frac{g^2}{\delta\,(\delta + \alpha)}, \tag{3.39}$$

where $g$ is the coupling strength to the first excited state and $\delta = \omega_\mathrm{q} - \omega_\mathrm{r}$ is the frequency difference of the qubit and readout resonator. Figure 3.7 displays the readout signal of the bosonic mode, implemented by a microwave resonator, depending on the quantum state of the transmon qubit.

For $\alpha/\delta \ll 1$ the scaling is rather close to that of Purcell loss, see Eq. (3.31). Particularly for high-quality transmons, maintaining a good readout signal while avoiding a limitation of $T_1$ by the Purcell effect is challenging. This makes Purcell filters indispensable for transmon circuits.

Additionally, the bosonic mode is dressed by the qubit, and its frequency becomes

$$\omega_\mathrm{r}' = \omega_\mathrm{r} - \frac{g^2}{\delta + \alpha}. \tag{3.40}$$

Experimentally, the oscillator can be decoupled from the qubit by applying strong drive fields. For a given $\delta$, the frequency difference of the resonator after and before decoupling is

$$\chi_{01} = \omega_\mathrm{r} - (\omega_\mathrm{r}' - \chi) = g^2/\delta, \tag{3.41}$$

which, for a given detuning, yields the coupling strength. This is in analog to Eq. (3.29) for the Jaynes-Cummings model with an ideal two-level qubit.

# 4 Microwave circuits for quantum devices

Nowadays, all superconducting quantum circuits are characterized and addressed by microwave photons [Gu+17]. As described in the previous section, additional energy relaxation and decoherence are introduced by coupling a qubit to its environment. This, however, is inevitable for both qubit state control and readout. Performance-impairing effects can be kept at a minimum if proper precautions are taken. Here, a sufficient understanding of the microwave environment qubits are embedded in is needed, which is provided in this chapter.

This chapter starts with a brief introduction to the concept of impedance in these circuits, followed by the S-matrix formalism - a vital tool for the characterization of microwave circuits. Thereafter, I shortly discuss microwave resonators, which are key components for the analog quantum simulation experiments presented in chapter 6 and for qubit state readout, see Sec. 3.3. Next, I talk about the design of microwave circuits. Finally, I give an overview of the measurement setup, both, in- and outside the cryostat.

## 4.1 Impedance

The concept of impedance is an extension of dc resistance for time-dependent signals. This becomes crucial, when the wavelength of voltage and current is on the scale of a network's circuit elements, as is the case for the quantum circuits investigated in this work. Consequently, the impedance matrix $Z$ of a microwave network links the (frequency-dependent) voltage response $\boldsymbol{V}$ to an applied current $\boldsymbol{I}$ via [Poz11]

$$\boldsymbol{V} = Z\boldsymbol{I}, \tag{4.1}$$

where the components $V_i$ ($I_i$) are voltage (current) at port $i$ of the network, see Fig. 4.1(a). Particularly, $V_i = V_i^+ + V_i^-$ and $I_i = I_i^+ - I_i^-$ where in- and outgoing signal are denoted by $+$ and $-$, respectively. For microwave photons, impedance plays a role similar to the refractive index of optical light. For example, with a

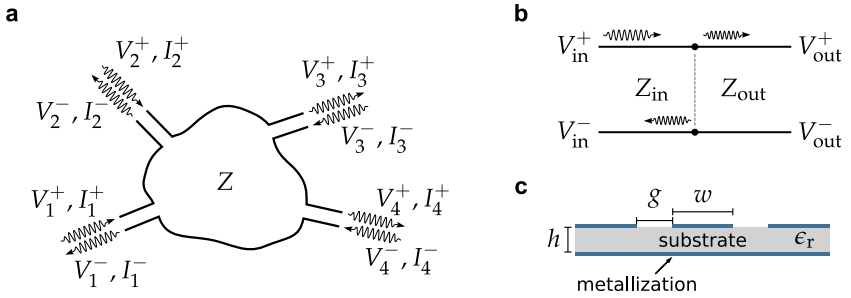


**Figure 4.1: Network impedance and reflection.** (a) The impedance of a microwave network connects in- and outgoing voltages and currents via Eq. (4.1). (b) A discontinuous impedance mismatch between two ports leads to partial reflection of incoming signals. (c) Schematic diagram of the cross-section of a coplanar waveguide. For a substrate of height $h$ and relative permittivity $\epsilon_r$, the line impedance can be adjusted via the ratio of track width $w$ to gap width $g$.

discontinuous impedance mismatch between two ports of a network, see Fig. 4.1(b), the reflection coefficient for an incident microwave is given by [Poz11]

$$\Gamma = \frac{V_{in}^-}{V_{in}^+} = \frac{Z_{out} - Z_{in}}{Z_{out} + Z_{in}}. \tag{4.2}$$

Here, $Z_{in}$ is the impedance of the in- and $Z_{out}$ of the output line. It becomes immediately clear that an industry standard for the impedance of all commercial transmission lines and cables, in fact all microwave devices, is needed. In modern microwave engineering, this is set to $Z_0 = 50\,\Omega$. Therefore, the impedance of the on-chip circuits employed in this thesis are also matched to $50\,\Omega$. In comparison, the impedance of free space $Z_{vac} \approx 377\,\Omega$ is higher [Mes06].

Two-dimensional transmission lines are typically implemented as metallic striplines. The go-to architecture for modern quantum circuits, are coplanar waveguides (CPW), see Fig. 4.1(c). Here, a central conductor of width $w$ is surrounded by an on-chip ground plane, separated by a gap of width $g$. Occasionally, an additional backside metallization is added. For lossless lines, capacitance and inductance per length, $C_l$ and $L_l$, respectively, define the line impedance $Z = \sqrt{L_l/C_l}$. Typically $w, g \ll h$, and the impedance is largely determined by the ratio of $g$ and $w$. For a perfect conductor on c-plane sapphire substrate ($\epsilon_r \approx 10$), a $50\,\Omega$ line impedance is achieved for $g/w \approx 0.5$ [Sim01; Che].

In coplanar waveguides, electric and magnetic fields are strongly confined, resulting in lower crosstalk compared to other architectures if a proper grounding is ensured. This also enables a tighter packaging and thus superior scalability. Therefore, CPW circuits are also employed throughout this work.

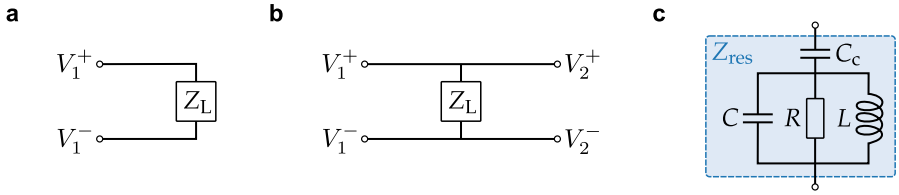


**Figure 4.2: Simple networks as examples for the *S*-matrix formalism.** (a) Schematic diagram of a simple one-port reflection network. The $S$-matrix of a load $Z_L$ connected to a transmission line is equal to the reflection coefficient $\Gamma$, see Eq. (4.2). (b) Simple network for a two-port measurement, with a load shunting the two conductors of a continuous transmission line. Here, the $S$-matrix is given by Eq. (4.6). If the load is a resonator, see Sec. 4.3, this is called a notch-type configuration. (c) Circuit diagram of a capacitively coupled microwave resonator. Inserting the total resonator impedance $Z_{res}$ as the load in Eq. (4.5) or Eq. (4.6) yields the $S$-matrix of the resonator circuit.

## 4.2 Scattering matrix formalism

An equivalent description of a microwave network using impedance is provided by the scattering matrix formalism. For an arbitrary network, Eq. (4.1) can be rewritten as [Poz11]

$$\boldsymbol{V}^- = S\boldsymbol{V}^+, \tag{4.3}$$

connecting in- ($\boldsymbol{V}^+$) to output voltage ($\boldsymbol{V}^-$). Analytically, the coefficients $S_{ij}$ are calculated by determining the outgoing voltage $V_i^-$ at port $i$ with an applied voltage $V_j^+$ to port $j$, i.e.,

$$S_{ij} = \frac{V_i^-}{V_j^+}. \tag{4.4}$$

Here, all other ports of the network are terminated by a fixed load $Z_0$, typically the standard $50\,\Omega$ impedance. In practice, the $S$-matrix can be measured more easily and is more intuitive to use than $Z$: $S_{ii}$ is the reflection coefficient $\Gamma_i$ of port $i$ and $S_{ij}$ is the transmission from port $j$ to $i$. For reciprocal networks, it is obvious that $S_{ij} = S_{ji}$ for all ports. In contrast to the transfer matrix, the scattering matrix is not linear: for a serial circuit, the total $S$-matrix is **not** a product of its constituents.

For example, using Kirchhoff's laws the $S$-matrices of a load $Z_L$ connected to a one-port transmission line, see Fig. 4.2(a) is calculated as

$$S^{\text{refl}} = S_{11} = \frac{Z_L - Z_0}{Z_L + Z_0} = \Gamma, \tag{4.5}$$

the reflection coefficient from Eq. (4.2). The $S$-matrix of a load, shunting a two-port transmission line, see Fig. 4.2(b) reads

$$S^{\text{notch}} = \begin{pmatrix} (1+\frac{2Z_L}{Z_0})^{-1} & (1+\frac{Z_0}{2Z_L})^{-1} \\ (1+\frac{Z_0}{2Z_L})^{-1} & (1+\frac{2Z_L}{Z_0})^{-1} \end{pmatrix}. \tag{4.6}$$

## 4.3 Microwave resonators

As elaborated in Sec. 3.3, the state readout of superconducting qubits is typically performed using harmonic resonators. The most prominent examples are microwave cavities and CPW resonators. Especially three-dimensional cavities provide a good isolation from the environment [Pai+11; Rig+12] and boast low internal losses. However, their large size hampers scaling up to larger systems. Coupling a single qubit to several resonators or shaping a mode spectrum also proves difficult. In two-dimensional cQED setups, such as those employed throughout this work, transmission line or lumped element resonators are used. While greater efforts are needed to achieve a low energy decay rate, they offer a good control and flexibility of all relevant parameters.

In this thesis, microwave resonators are employed for dispersive readout and as components in the analog quantum simulator described in chapter 6. Therefore, the basics tools needed to work with on-chip microwave resonators are presented in this section. Starting with their implementation, we discuss the definition of linewidth and quality factors, and the *S*-matrix of reflection- and notch-type resonators. Finally, the implementation of Purcell filters, see Sec. 3.3.2 on Purcell loss, is presented.

### 4.3.1 Planar resonators

On-chip microwave resonators are typically implemented as distributed or lumped element RLC-circuits, see Fig. 4.3(a, b). The frequency of a lumped element resonator is connected to its capacitance $C$ and inductance $L$ via

$$\omega_\mathrm{r} = \frac{1}{\sqrt{LC}}. \tag{4.7}$$

The more common, distributed or transmission line resonators consist of a simple metal strip, with a continuous field distribution along its length, similar to an antenna, see Fig. 4.3(c). Grounding either end of the strip forces a voltage node and current anti-node. This allows for the implementation of both $\lambda/2$- and $\lambda/4$-resonators. Their frequency

$$\frac{\omega_\mathrm{r}}{2\pi} = \frac{c_0}{\sqrt{\epsilon_\mathrm{eff}}}\frac{1}{xl} \tag{4.8}$$

depends on the strip length $l$ and effective dielectric constant $\epsilon_\mathrm{eff} \approx \left(\epsilon_\mathrm{r}^\mathrm{vac} + \epsilon_r^\mathrm{subst}\right)/2$, which is approximately the mean value of the vacuum and substrate dielectric constants [Göp+08]. The vacuum speed of light is denoted as $c_0$ and $x \in \{2, 4\}$

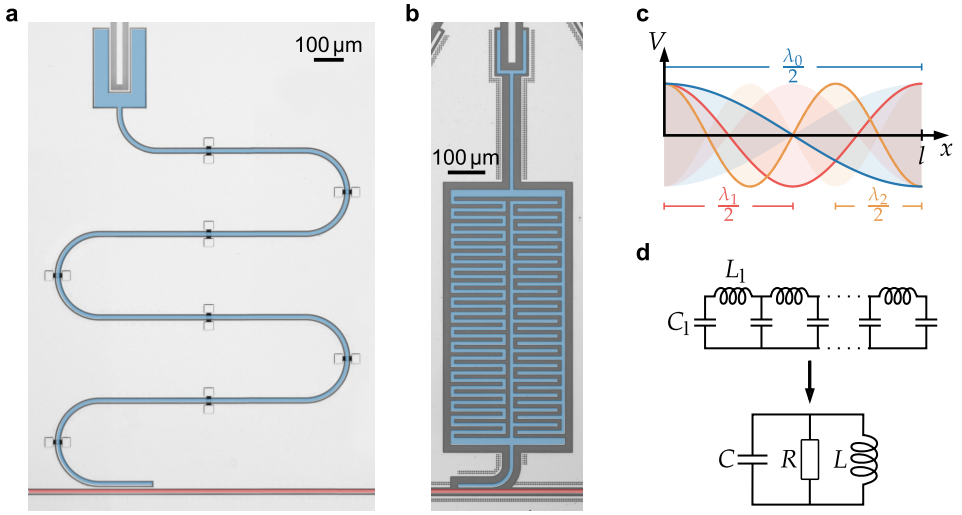


**Figure 4.3: Microwave resonators in a two-dimensional circuit architecture.** Optical micrograph of a distributed (a) and lumped element resonator (b) implemented in a CPW circuit. The resonators (blue) are coupled capacitively to a transmission line (red). (c) Spatially resolved voltage $V$ of a $\lambda/2$-transmission line resonator of length $l$ for the first three modes (blue, red, orange in ascending order). (d) Translation from a distributed to an effective lumped circuit. Here, the effective capacitance $C$ and inductance $L$ of the stripline resonator mainly depend on its length.

for a $\lambda/x$-resonator. In conjunction with the line impedance $Z = \sqrt{L_l/C_l}$ of the resonator, Eq. (4.8) can be used to assign an effective capacitance and inductance, translating the distributed resonator to an RLC-circuit, see Fig. 4.3(d). Whether this results in a parallel or series RLC-circuit depends on the coupling to the transmission line, which is discussed in Sec. 4.3.3. In stark contrast to (ideal) lumped element resonators, their distributed cousins also feature higher modes. Electric and magnetic fields are only fixed at the current or voltage nodes at the ends of the strip. Consequently, the circuit can accommodate additional resonances with a higher frequency and node number than the fundamental mode. If capacitance and inductance are linear and distributed homogeneously along the transmission line, the frequency $\omega_r^n$ of higher modes is given by

$$\omega_r^n = \omega_r^0 \left(1 + \frac{nx}{2}\right), \tag{4.9}$$

where $\omega_r^0$ is the fundamental frequency of the oscillator from Eq. (4.8). With increasing mode number $n$ an additional node is added and the wavelength decreases. This is illustrated in Fig. 4.3(c), which displays the first three resonances of a $\lambda/2$-transmission line resonator. Experimentally, higher modes are usually ignored, as they are far detuned from the lowest resonance frequency.

Finally, transmission line resonators can also host so-called slotline modes [Poz11]. These resonances live in the gap of a CPW resonator (neglecting the inner conductor). If they couple to the qubit, they introduce additional Purcell loss, see Sec. 3.3.2, which can be detrimental to the qubit's energy lifetime. Slotline modes are suppressed by ensuring a proper galvanic connection of the opposing ground planes of a CPW structure, for example, by using airbridges, see Sec. 5.2.

### 4.3.2 Resonator linewidth and quality factors

Generally, a transition subjected to energy decay suffers from spectral broadening. The linewidth $\kappa$ of the transition is then proportional to the decay rate. Especially if the latter is frequency-independent, this results in a Lorentzian line shape. For a full width at half maximum of $\kappa$, the decay rate is identified as $\kappa/2$, using Fourier transformation. The linewidth of microwave resonators comprises both irradiation loss into the transmission line and internal losses. This is captured by the quality factors $Q_\mathrm{i}$ and $Q_\mathrm{c}$ for internal and coupling loss, respectively, which are defined as [Poz11]

$$Q_n = \omega_\mathrm{r} \frac{\text{stored energy}}{\text{energy loss rate via channel } n} = \frac{\omega_\mathrm{r}}{\kappa_n}. \tag{4.10}$$

The stored energy is the sum of the (time-averaged) electric and magnetic field energies. The internal quality factor $Q_\mathrm{i}$ is calculated via the dissipation of the resistor $R$ in the circuit. Interpreting the resonator as a generator, $Q_\mathrm{c}$ is calculated from the power lost in the load of the transmission line.

Decay rates add up linearly. The total or loaded quality factor is therefore given by

$$Q_\mathrm{L} = \left( \frac{1}{Q_\mathrm{i}} + \frac{1}{Q_\mathrm{c}} \right)^{-1} = \frac{\omega_\mathrm{r}}{\kappa}. \tag{4.11}$$

It is clear that the ratio of $Q_\mathrm{i}$ and $Q_\mathrm{c}$ plays a major role in the frequency response of a resonating system. Here, $Q_\mathrm{i} < Q_\mathrm{c}$ is denoted as under-coupled and $Q_\mathrm{i} > Q_\mathrm{c}$ as over-coupled. At critical coupling $Q_\mathrm{i} = Q_\mathrm{c}$, a resonator dissipates all incoming photons, as the energy uptake rate is equal to the dissipation rate.[1]

[1] This is the optimal operation regime of an antenna.

### 4.3.3 Scattering coefficients of reflection- and notch-type resonators

The scattering matrix of a resonating circuit is independent of the resonator implementation, i.e., if it is a lumped or distributed circuit. Additionally, it remains largely unaffected by the coupling type to the transmission line: For example, an inductively coupled $\lambda/4$-resonator results in the same $S$-matrix as a capacitively coupled $\lambda/2$-resonator in an equivalent circuit. Overall, it proves more relevant to distinguish between the setup of the network, that is, if a resonator is embedded in a single- or two-port network. Here, it can be distinguished between reflection-, notch-type, and inline-resonators. In the context of this work, the latter do not find an application. For a more elaborate treatment, it is referred to the literature, e.g., Refs. [Poz11; Bra17].

As their name indicates, reflection-type resonators are coupled to a transmission line with a single port and addressed in reflection. Notch-type resonators are side-coupled to a continuous transmission line with two ports. Around the resonance frequency $\omega_\mathrm{r}$, their impedance can be approximated as [Bra17]

$$\begin{aligned} Z_\mathrm{refl}/Z_0 &= \frac{Q_\mathrm{c}}{Q_\mathrm{i}} + 2\mathrm{i}Q_\mathrm{c}\frac{\Delta\omega}{\omega_r} \\ Z_\mathrm{notch}/Z_0 &= \frac{Q_\mathrm{c}}{2Q_\mathrm{i}} + \mathrm{i}Q_\mathrm{c}\frac{\Delta\omega}{\omega_r}, \end{aligned} \tag{4.12}$$

with $\Delta\omega = \omega - \omega_\mathrm{r}$. Evidently, $Z_\mathrm{notch}$ is equal to $Z_\mathrm{refl}$ when $Q_\mathrm{c} \to Q_\mathrm{c}/2$. In contrast to the reflection-resonator, the notch-type can irradiate into two ports. Intuitively, the coupling relaxation rate is doubled, hence, reducing $Q_\mathrm{c}$ by a factor of 2.

By inserting Eq. (4.12) into Eq. (4.5) and 4.6, $S_{11}$ for a reflection- and $S_{21}$ for the notch-type resonator are calculated as

$$\begin{aligned} S_{11}^\mathrm{refl} &= 1 - \frac{2Q_\mathrm{L}/Q_\mathrm{c}}{1 + 2\mathrm{i}Q_\mathrm{L}\frac{\Delta\omega}{\omega_\mathrm{r}}}, \\ S_{21}^\mathrm{notch} &= 1 - \frac{Q_\mathrm{L}/Q_\mathrm{c}}{1 + 2\mathrm{i}Q_\mathrm{L}\frac{\Delta\omega}{\omega_\mathrm{r}}}. \end{aligned} \tag{4.13}$$

Figure 4.4 displays the absolute value or amplitude (a, d), phase (angle in the complex plane) (b, e), and complex-valued $S_{11}^\mathrm{refl}$ (c) and $S_{21}^\mathrm{notch}$ (f) for several values of $Q_\mathrm{L}/Q_\mathrm{c}$. In the complex plane, the $S$-parameter forms a circle with diameter $2Q_\mathrm{L}/Q_\mathrm{c}$ for reflection- and $Q_\mathrm{L}/Q_\mathrm{c}$ for notch-type resonators. In both cases, the square of the amplitude signal follows a Lorentzian line shape with a full width at half maximum of $\kappa$. Especially for notch-type resonators, it is tempting to extract the

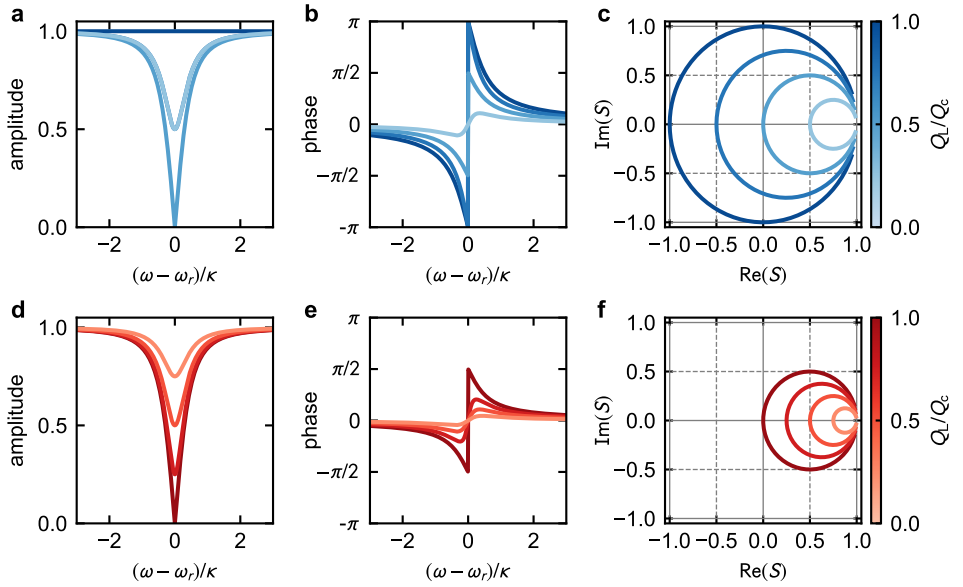


**Figure 4.4: Response $S_{11}{}^{\text{refl}}$ of reflection- (top, blue) and $S_{21}{}^{\text{notch}}$ of notch-type resonators (bottom, red) featuring various $Q_L/Q_c$.** The amplitude signal of both reflection- (a) and notch-type resonators (d) follows a Lorentzian shape. Due to energy conservation, the reflection signal is unity in the absence of internal losses ($Q_i = \infty$), whereas the input energy is fully dissipated at critical coupling. A lossless notch-type resonator achieves perfect reflection (i.e., no transmitted signal) on resonance, while dissipating $1/2$ of the input power at critical coupling. The phase roll-off of reflection-type resonator (b) is $2\pi$ for over-coupled resonators. At critical coupling, a discontinuous jump reduces the phase shift to $\pi$. Here, it becomes identical to that of a notch-type resonator (e) with $Q_i = \infty$. For increasing internal loss, the phase shift becomes less prominent (for both configurations) and vanishes at $Q_i = 0$, together with the amplitude signal. (c, f) In the complex plane, the $S$-parameter forms a circle with diameter $2Q_L/Q_c$ for $S_{11}^{\text{refl}}$ and $Q_L/Q_c$ for $S_{21}^{\text{notch}}$.

resonance frequency and quality factors from a simple one-dimensional fit of the Lorentzian function. However, a more reliable and accurate method is provided by the circle fit routine, which considers the full, complex-valued S-parameter [Pro+15].

Resonators for qubit state readout are preferably operated in the over-coupled regime. Here, more photons couple out of the resonator and therefore the signal-to-noise ratio (SNR) is greater. Due to the loss of their dc resistance, the internal quality factor of superconducting resonators is intrinsically high and over-coupled devices are achievable, even for large $Q_c$.

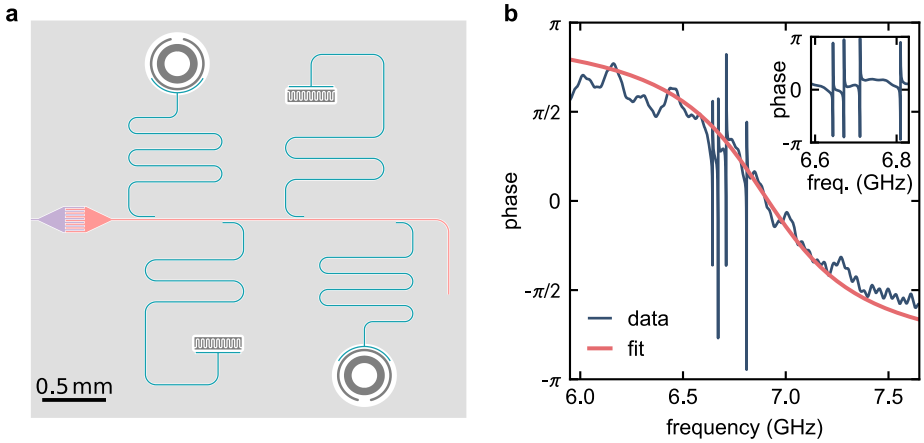


**Figure 4.5: Purcell filter for reflection measurements.** (a) Chip layout of a Purcell filter (pink) for reflection experiments. The linewidth of the filter has to be large enough to accommodate all four resonators (blue) at a sufficient frequency spacing. This is ensured by the large coupling capacitance to the input line (purple). The on-chip ground plane of the CPW is displayed in light gray, the qubit electrodes are colorized in dark gray. (b) Phase of the reflected signal. In the inset the signal around the four resonators is magnified. They are located comfortably in the center of the Purcell filter with a linewidth of $\kappa_\mathrm{f} = (689 \pm 10)\,\mathrm{MHz}$, extracted from a fit (pink), much larger than the linewidth of the individual resonators. The qubits (gray) are inactive in the experiment.

### 4.3.4 Purcell filters

As discussed in Sec. 3.3.2, Purcell loss significantly contributes to the energy relaxation of superconducting qubits, most notably for state of the art devices. However, it can be suppressed efficiently by employing Purcell filters [Jef+14]. As displayed in Fig. 4.5(a), the readout resonator is coupled to a broadband oscillator, acting as a bandpass. Thereby, the qubit is screened from the transmission line's mode spectrum while maintaining a fast state readout, see Fig. 4.5(b).

The effective decay rate seen by the readout resonator and qubit reads [SMK15]

$$\kappa_{\mathrm{r,q}}^{\mathrm{eff}} = \frac{4|G|^2}{\kappa_\mathrm{f}} \frac{1}{1 + \left(\left(\omega_{\mathrm{r,q}} - \omega_\mathrm{f}\right)/\kappa_\mathrm{f}\right)^2}, \tag{4.14}$$

where $\omega_\mathrm{f}$ and $\kappa_\mathrm{f}$ are the frequency and bandwidth of the filter and $G \ll \kappa_\mathrm{f}$ is the coupling strength between readout resonator and filter. Choosing $\omega_\mathrm{f} \approx \omega_\mathrm{r}$ results in a large decay rate $\kappa_\mathrm{r}^{\mathrm{eff}}$ of the resonator, while suppressing $\kappa_\mathrm{q}^{\mathrm{eff}}$ seen by the qubit. For a transmon qubit with low anharmonicity $\alpha$ compared to the detuning $\delta = \omega_\mathrm{q} - \omega_\mathrm{r}$, this leads to a Purcell decay rate of [SMK15]

$$\Gamma_\mathrm{P} \approx \kappa_\mathrm{r}^{\mathrm{eff}} \left(\frac{\kappa_\mathrm{f}}{\delta}\right)^2 \left(\frac{g}{\delta}\right)^2, \tag{4.15}$$

where $g$ is the coupling strength between qubit and readout resonator. The approximation holds for $\alpha, \kappa_f \ll \delta$. Compared to a setup without Purcell filter, $\Gamma_P$ is suppressed by an additional factor of $(\kappa_f/\delta)^2$. For transmon circuits in particular, Purcell filters are indispensable due to the weaker scaling of the dispersive shift, which demands a larger qubit-resonator coupling to achieve a strong readout signal.

## 4.4 Circuit design and tools

Apart from material science and cleanroom engineering, novel circuit designs such as the transmon, see Sec. 3.4, or fluxonium qubit have been crucial to the improvement of qubit life-, and coherence times. Modern qubit architectures can reach $T_1$ and $T_2$ times on the order of several hundred microseconds [Pai+11; Bar+13; Pop+14; Ner+19; Zha+20; Pla+20]. Here, clever circuit designs enable a resistance to some of the most relevant loss channels. Nevertheless, current designs are far from perfect: Nowadays, theoreticians and experimentalists work towards topologically protected qubits, virtually immune to external perturbations, for example, the $0-\pi$ qubit [Kit06; BKP13; Gye+19]. As of late, automated tools, quantifying the energy levels of a circuit based on its geometry, can be consulted when developing new qubit architectures [GS20]. Independent of the qubit architecture, an improperly designed environment can prove detrimental to the coherence of the system. Optimizing the coupling of a qubit to its readout and control circuitry is therefore essential.

This section outlines the most commonly used formalism to quantize a circuit (i.e., circuit quantization). Furthermore, it provides a set of tools and formulas, which help to design coherent qubit circuits.

### 4.4.1 From circuit to quantum Hamiltonian

In a given circuit, quantum properties can emerge if the thermal energy $k_B T$ is smaller than the energetically lowest (relevant) transition of the circuit. For superconducting circuits installed in a dilution cryostat, see Sec. 2.4, the base temperature of 20 mK corresponds to a frequency of $\sim 400$ MHz.[2] Additionally, a clear separation of the circuit's energy eigenstates is needed, which is typically

[2] Operating qubits with a lower frequency is only possible with additional cooling or outside of the thermal equilibrium, see, e.g., Ref. [Zha+20].

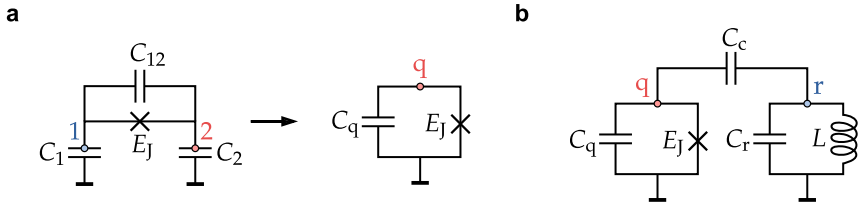


**Figure 4.6: Schematic circuits.** (a) Schematic circuit of a transmon qubit. Two floating electrodes with capacitance $C_1$ and $C_2$ to ground and a mutual capacitance $C_{12}$ are shunted via a Josephson junction with inductance $L_J$. Assuming that $q_1 = q_2$ for the node charges, one degree of freedom can be eliminated, yielding the effective qubit capacitance $C_q^{\text{eff}} = C_{12} + (1/C_1 + 1/C_2)^{-1}$. (b) Circuit diagram of a transmon qubit coupled to a microwave resonator. The capacitance $C_c$ determines the coupling strength $g$ between the two systems.

achieved by exploiting the non-linear current-phase relation of one or several Josephson junctions.

The Hamiltonian of a quantum device can be derived using circuit quantization, outlined in this section. For a detailed discussion, it is referred to the literature, e.g., Ref. [Dev97]. In principle, any classical circuit can be quantized: Each node of the network has a node charge and flux degree of freedom, summarized in the operators $\hat{\boldsymbol{q}}$ and $\hat{\boldsymbol{\phi}}$. The Hamiltonian takes the form [Dev97]

$$\hat{H} = \frac{1}{2}\hat{\boldsymbol{q}}C^{-1}\hat{\boldsymbol{q}} + \sum_{k,l} E_L^{k,l}(\hat{\phi}_k, \hat{\phi}_l, \Phi_{\text{ext}}^{k,l}), \tag{4.16}$$

where $C$ is the Maxwell capacitance matrix [Di 11]. The flux energy $E_L^{k,l}$ depends on the phase drop between nodes $k$ and $l$, thus also on the external flux $\Phi_{\text{ext}}^{k,l}$ enclosed by the loop. For example, a linear inductance $L$ connecting two nodes results in $E_L^{k,l} = (\hat{\phi}_k - \hat{\phi}_l + \Phi_{\text{ext}}^{k,l})^2/2L$, whereas a Josephson junction with Josephson energy $E_J$ yields $E_L^{k,l} = -E_J \cos(\hat{\phi}_k - \hat{\phi}_l + \Phi_{\text{ext}}^{k,l})$. Naturally, the external flux is zero in the absence of a closed loop or bias current.

Figure. 4.6 displays the circuit diagram of (a) a floating transmon qubit and (b) a transmon coupled capacitively to a resonator. Here, the $2 \times 2$ capacitance matrix is easily inverted, uncovering (a) the transmon Hamiltonian from Eq. (3.32) with the effective qubit capacitance $C_q^{\text{eff}} = C_{12} + (1/C_1 + 1/C_2)^{-1}$,[3] and (b) of a transmon coupled to a resonator

$$\hat{H} = \frac{q_q^2}{2C_q^{\text{eff}}} - E_J \cos\left(2\pi \frac{\phi_q}{\Phi_0}\right) + \frac{q_r^2}{2C_r^{\text{eff}}} + \frac{\phi_r^2}{2L} + \frac{q_q q_r}{C_c^{\text{eff}}}. \tag{4.17}$$

[3] Here $C_{12}$ includes the junction capacitance $C_J$

Here, $q_i$ is the charge on the effective capacitance $C_i^{\text{eff}}$. For $C_c \ll C_q, C_r$, the effective qubit, resonator, and coupling capacitance can be approximated as

$$C_q^{\text{eff}} \approx C_q + C_c, \quad C_r^{\text{eff}} \approx C_r + C_c \quad \text{and} \quad C_c^{\text{eff}} \approx \frac{C_q C_r}{C_c}. \tag{4.18}$$

After a short mathematical exercise, the Jaynes-Cummings Hamiltonian from Eq. (3.23) is recovered, see Appendix C.

Once a solution is found, it becomes a simple engineering problem to map the schematic onto a physical circuit. Using finite element method (FEM) solvers, for instance, Ansys Maxwell$^{\text{TM}}$, the Maxwell capacitance matrix of a model circuit can be simulated directly. The same applies for distributed inductances. Alternatively, microwave-simulations with Sonnet$^{\text{TM}}$ (2.5-dimensional model) or Ansys HFFS$^{\text{TM}}$ (3-dimensional model) directly yield the transition frequency of resonant systems. This is applicable to microwave resonators, but also allows to extract the effective capacitance $C_q^{\text{eff}}$ of transmon qubits, by replacing the Josephson junction with a lumped element with the inductance $L_J$, see Sec. 3.4.1. Especially CPW circuits benefit from this method: If the coupling capacitance does not disrupt the ground plane, adding, removing, or changing a coupler barely affects the total qubit capacitance.

### 4.4.2 Dispersive state readout with microwave resonators

Regardless of the resonator type, the $S$-parameter changes the most, when the dispersive shift $\chi$ and resonator linewidth $\kappa$ fulfill

$$\chi = \kappa/2, \tag{4.19}$$

which corresponds to two opposing sides of the circle in the complex plane. Since the linewidth is proportional to the photon decay rate, larger $\kappa$ allow for a faster state readout [Jef+14]. Additionally, a greater drive power can be applied without increasing the average photon number in the resonator, thus further improving the SNR. This of course comes at the cost of increased Purcell loss, see Eq. (3.31). Particularly for transmon qubits Eq. (4.19) imposes a fundamental lower limit of $\Gamma_P \approx \kappa^2/2\alpha$ to the Purcell decay rate, even at infinite detuning. Once again, this underlines the importance of Purcell filters for transmon qubits of a certain quality.

For a given $\kappa$, the qubit-resonator coupling is adjusted, such that Eq. (4.19) is fulfilled. The coupling strength $g$ is calculated using the Maxwell capacitance matrix or extracted by simulating the avoided crossing with the readout resonator,

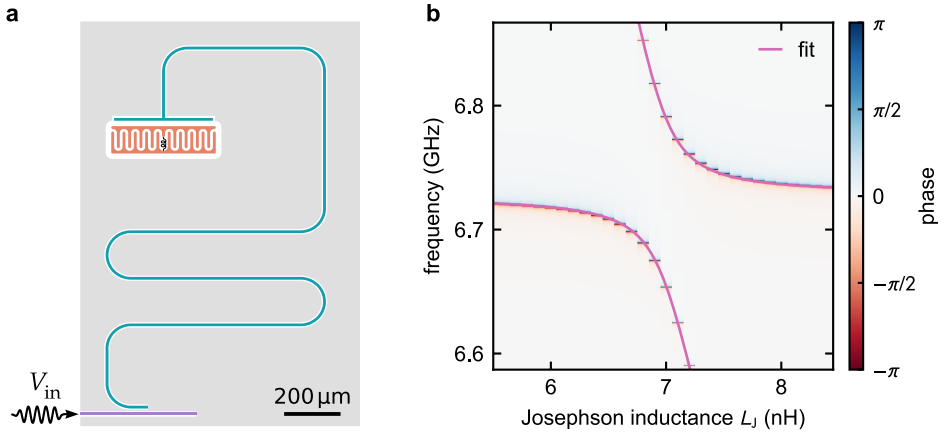


**Figure 4.7: Simulation of circuit parameters.** (a) Scheme of the circuit. In the simulation, the transmon (orange) qubit's Josephson junction is replaced by a lumped element inductance $L_J$. The (now harmonic) transmon is probed either directly to extract $C_q^{eff}$ from Eq. (4.7) or, as done here, is coupled to a resonator (blue). (b) Phase of the signal reflected at the input port (purple). By sweeping $L_J$, the qubit is tuned on resonance with the microwave resonator. The coupling strength $g_{sim}$ is extracted from the emerging avoided level crossing using Eq. (3.25), from a fit (pink).

see Fig. 4.7. Notably, $g$ is frequency-dependent for the transmon circuit displayed in Fig. 4.6(b), see Appendix C. Equation (C15) yields the target coupling strength

$$g_t \approx g_{sim}\sqrt{\frac{\omega_q}{\omega_r}}, \tag{4.20}$$

at the qubit's working point $\omega_q$ from the simulated coupling coefficient $g_{sim}$ at the resonator's frequency.

A proper mathematical treatment of pulsed dispersive readout shows that, for a given $\chi/\kappa$, optimal readout conditions also depend on the frequency and length of the readout tone [Sok16].

### 4.4.3 Qubit drive lines

Qubit drive lines are in principle one-port transmission lines, coupled only to the qubit. In comparison to qubit manipulation via the resonator port, a dedicated drive line mitigates crosstalk with other circuit elements. Furthermore, the field seen by the qubit is only perturbed by the transfer function of the cryostat wiring. In contrast, pulses routed via the readout line see the qubit through the resonator, which acts as a band-pass filter. However, coupling the qubit directly to the mode spectrum of the drive line also induces additional energy decay and decoherence

from thermal radiation [Kra+19]. The relaxation is comparable to $\kappa_c$ of a reflection-type resonator. For the qubit, this results in an additional energy relaxation rate of

$$\Gamma_d = \frac{\omega_q}{Q_c} = \frac{C_d^2 w_q^2 Z_0}{2C_q^{eff}}, \tag{4.21}$$

where $C_d$ is the capacitance between qubit and drive line, $Z_0$ is the line impedance, and $C_q^{eff}$ is the total qubit capacitance. A larger coupling capacitance allows for faster $xy$-gates at the same input power, see Sec. 3.1.2, but at the same time results in additional Purcell loss.

### 4.4.4 On-chip flux bias

Flux-tunable superconducting quantum circuits, e.g., the tunable transmon discussed in Sec. 3.4.2, require magnetic bias fields. Often, external coils are used to apply a flux bias to SQUIDs. Du its higher inductance, an external coil provides a more stable field than an on-chip coil, however, fast flux tuning is not possible. Impedance-matched on-chip coils, i.e., transmission lines shunted to ground, can carry both radio-frequency (rf) and dc current biases to tune a SQUID via its mutual inductance $M$ to the line. For thin conductors, the mutual inductance is in good approximation calculated with [Neu46]

$$M = \frac{\mu_0}{2\pi} \int_{C_{bias}} \oint_{C_{SL}} \frac{d\boldsymbol{x}_{SL} d\boldsymbol{x}_{bias}}{|\boldsymbol{x}_{SL} - \boldsymbol{x}_{bias}|}. \tag{4.22}$$

Here, $\mu_0$ is the vacuum permeability and the vector $\boldsymbol{x}_i$ traces the contour $C_i$, of SQUID loop (SL) and bias line, respectively.

## 4.5 Microwave packaging and measurement setup

After having discussed the optimization of on-chip circuitry, we also need to focus on the measurement setup and sample mounting to achieve a good performance of our quantum devices. Particularly, poorly filtered control lines and noisy electronics can be detrimental to qubit coherence. To prevent a deterioration of the performance of quantum circuits, it is important to optimize the sample mounting and cryostat wiring [Lie+19; Yan+18; Kri+19]. Even the measurement routines are designed to impair qubit performance as little as possible.

### 4.5.1 Sample mounting

Sample boxes are the immediate interface connecting a quantum chip with its control lines and the cryostat they reside in. A good thermal coupling to the cryostat's base stage ensures proper thermalization. High electrical conductivity reduces energy loss due to surface currents in the holder. For example, gold-plated copper offers both, good thermal and electrical conductivity [Lie+19]. Most importantly, the sample box should be free of resonances (in the relevant frequency range), which could result in additional Purcell loss.

Figure 4.8 displays the image of a typical sample holder used in this work. Here, we opted for superconducting aluminum sample boxes. While the thermal conductivity is lower than that of copper, they have a higher electrical conductivity. Intrinsically, they offer magnetic shielding due to the Meissner-Ochsenfeld effect when operated below the critical temperature of aluminum, see Sec. 2.1. Permalloy shields can provide additional protection, especially at $T > T_{\mathrm{c,\,Al}}$. Samples are glued to the holder using silver conductive paste and are connected to a copper-plated printed contact board (PCB) made of TMM® 10 with a relative permittivity of $\epsilon_{\mathrm{r}} = 9.2$ [Cor20]. Wire bonding ensures the galvanic connection of on-chip control lines and ground plane to their counterpart on the PCB. The latter is soldered to standard SMA connectors, linking the sample to the outside world.

### 4.5.2 Microwave measurement setup

#### Low temperature setup

Cryogenic control lines are the only interconnection of a quantum chip with the outside world. To preserve quantum coherence while still allowing to probe the system, this interaction has to be kept at a minimum. A photograph and schematic diagram of the microwave wiring of our setup is displayed in Fig. 4.8(b) and Fig. 4.9(b), respectively. The working principle of the cryostat is summarized in Sec. 2.4.

On the input lines, a sequence of attenuators on multiple temperature stages in conjunction with high-pass and infrared filters on the base stage is employed to shield the sample from photons outside the measurement band, including thermal radiation. The attenuation chain reduces incoming signals to the single-photon regime. Additionally, each attenuator thermally anchors the central conductor of the coaxial lines to the stage it is installed on. Thermal radiation can be a primary source of qubit dephasing [Yan+18]. Operating state of the art qubits at

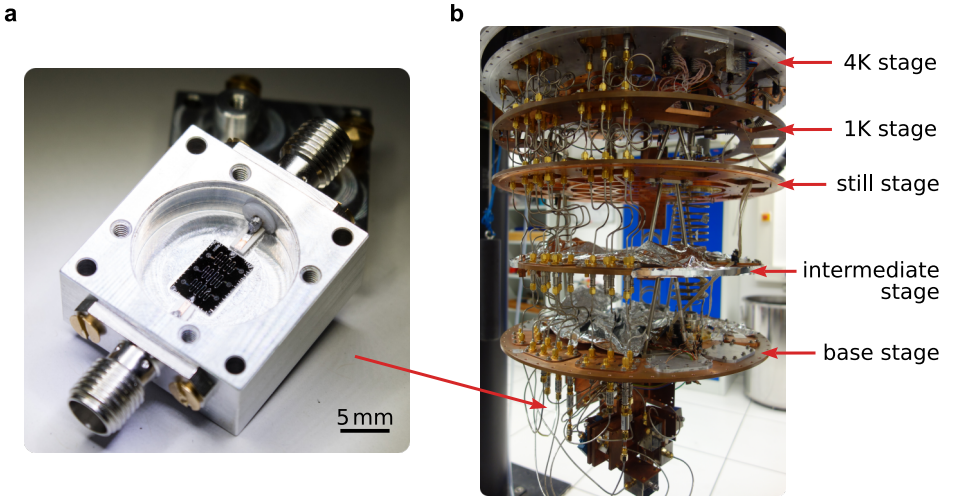


**Figure 4.8: Sample holder and cryogenic microwave setup.** (a) Microchip installed in an aluminum sample holder. Aluminum wire bonds ensure the galvanic connection of sample box and PCB with the on-chip ground plane and control lines. SMA plugs are soldered to the PCB, connecting the sample to the outside world. The thick lid ensures a small mode volume. In the experiment, the holder is installed on the base stage of the cryostat, indicated by the red arrow. (b) Microwave control lines in the cryostat. Attenuators on the 4 K, intermediate, and base stage protect the sample from thermal radiation.

the fundamental limit of $T_2 = 2T_1$, see Sec. 3.2.1, is only feasible with sufficient attenuation. Assuming perfect thermalization, the number of incident thermal photons $n_i$ at stage $i$ is calculated recursively from [Kri+19]

$$n_i = \frac{A_i - 1}{A_i} n_{\mathrm{BE}}(\omega, T_i) + \frac{n_{i-1}}{A_i}, \tag{4.23}$$

where $n_{\mathrm{BE}}(\omega, T)$ is the Bose-Einstein distribution at the working frequency $\omega$ and stage temperature $T_i$ and $A_i$ is the power attenuation coefficient. For the cryogenic microwave setup sketched in Fig. 4.9(b), a thermal photon number of $n_{\mathrm{base}} \approx 3 \cdot 10^{-4}$ is expected at $\omega = 5\,\mathrm{GHz}$. This corresponds to a noise temperature of $T_{\mathrm{noise}} = 20.14\,\mathrm{mK}$, i.e., only marginally above the nominal base temperature. Experimentally, the circuit temperature is slightly higher due to nonequilibrium effects [Jin+15; Ser+18; Sci+20].

Outgoing signals are typically only few photons strong. On the 4 K stage, a high-electron mobility transistor amplifier (HEMT) provides about 40 dB amplification. The sample is protected from thermal radiation and noise coming from the HEMT using high-pass filters together with non-reciprocal microwave circuits, such as circulators or isolators. Further amplification is provided by two 26 dB room temperature amplifiers.

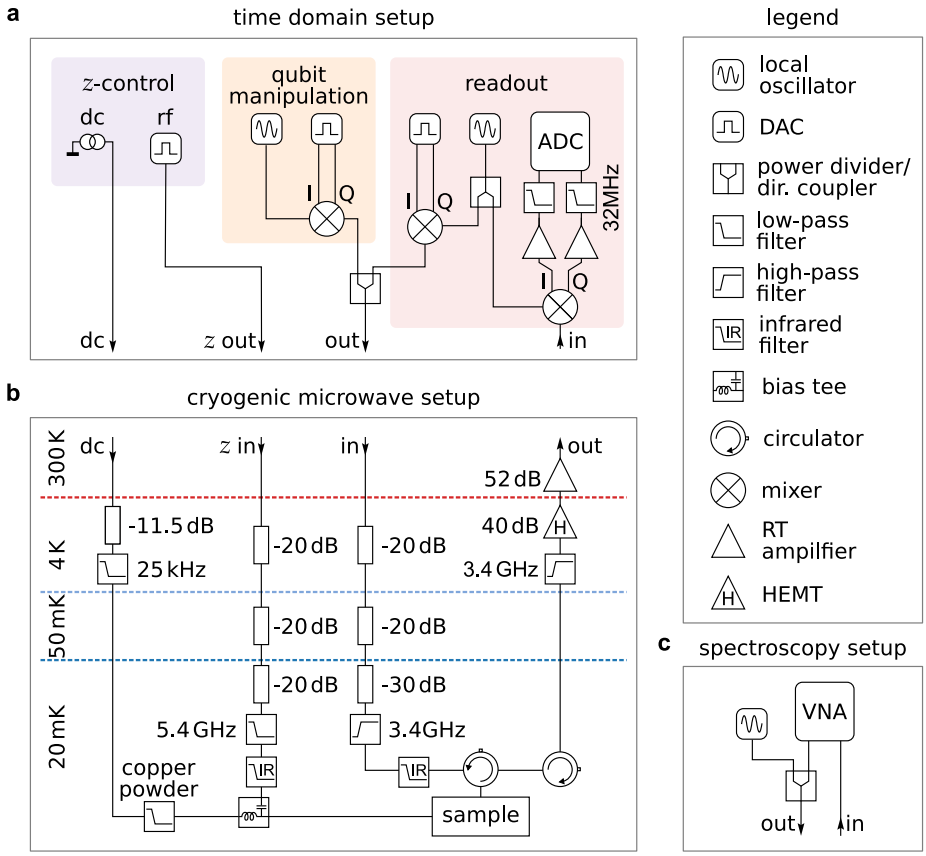


**Figure 4.9: Microwave measurement setups.** (a) Measurement setup for time domain experiments. rf and dc current biases for $z$-control are combined on the base stage using a bias tee. Single-sideband pulses for qubit manipulation and readout are synthesized using a continuous microwave tone and in-phase (I) and quadrature (Q) components of a pulse with a low carrier frequency in the MHz regime. This conversion is reverted before analyzing the returning signal. (b) Microwave setup inside the dilution refrigerator. Attenuators on three temperature stages mitigate thermal radiation from the $z$-control and input line. On the output line, two circulators and a high-pass filter protect the sample (measured in reflection) from thermal and HEMT noise. Incoming dc lines are low-pass filtered on 4 K and base stage with an RCR- and a copper powder filter, respectively. (c) Setup for two-tone qubit spectroscopy. Using the VNA, the dispersive shift of a readout resonator in response to an applied microwave tone can be monitored. This figure is adapted from our work in [Ste+20].

For tunable samples, bias currents are applied using dc lines with appropriate low-frequency filtering. They are attenuated at the 4 K stage using a current divider to ground. Large biases at room temperature lead to small currents at the sample, which helps to mitigate the noise of the current source. Additional capacitors to ground reduce high frequency noise. Additionally, an RCR T-filter eliminates high-frequency noise above 25 kHz. At the base stage, a copper powder filter fulfills the same purpose. Thereafter, a bias tee combines the constant bias with incoming rf pulses for fast qubit control.

**Spectroscopy setup**

Figure 4.9(c) displays a simple spectroscopy setup. A vector network analyzer (VNA), is employed to directly measure the transmission coefficient $S_{21}$ of the cryostat which, with proper wiring and sample packaging, is dominated by the response of the quantum chip. Additional drive tones can be routed to the sample using a directional coupler or power divider.

Particularly, two-tone experiments are vital tools for the characterization of qubit circuits. Here, the VNA is used to monitors the readout resonator's dispersive shift, while the frequency of a local oscillator (LO) is swept around the expected qubit transition. Once the LO's microwave tone comes in the vicinity of qubit frequency $\omega_q$, the average qubit population increases. The resulting dispersive shift of the readout resonator is registered by the VNA. An example hereof is displayed in Fig. 3.5(b) and Fig. 3.6(b).

**Time domain setup**

Many superconducting qubits, including the transmon, are operated in the GHz-regime. Unlike continuous drive tones, generating well-defined control pulses at these frequencies is challenging for semiconducting electronics. A workaround is provided by single-sideband mixing. In an $IQ$-mixer, a continuous microwave tone with the frequency $f_{LO}$ is multiplied with in-phase ($I$) and quadrature ($Q$) components of a pulse with a carrier frequency $f_{IQ}$ in the MHz-regime. Here, $Q$ is phase-shifted by 90° with respect to $I$. Choosing a common envelope for in-phase and quadrature results in an output pulse with the shared envelope and a carrier frequency of $f_{out} = f_{LO} + f_{IQ}$. In this scheme, power leakage is practically non-existent at the target frequency $f_{out}$ and strongly suppressed at $f_{LO}$.

A schematic diagram of the time domain setup used in this work is displayed in Fig. 4.9(a). We employ single-sideband mixing for both qubit state readout

($f_{\mathrm{IQ}}^{\mathrm{r}} = 30\,\mathrm{MHz}$) and manipulation ($f_{\mathrm{IQ}}^{\mathrm{q}} = 40\,\mathrm{MHz}$). Here, $I$ and $Q$ are produced with arbitrary waveform generators (AWGs). In the absence of a dedicated qubit drive line, qubit control and readout pulses are admitted via a common input line using a power divider or directional coupler. The analog-to-digital converter (ADC) monitoring incoming signals has a sampling rate of 500 MS/s. Therefore, the mixing has to be reverted before feeding the signal to the ADC. This process is less susceptible to errors when a common LO is employed for pulse generation and down-conversion, especially phase stability is ensured. Before signal acquisition, $I$ and $Q$ are filtered with a 32 MHz low-pass to remove higher harmonics and amplified.

All input/output devices comprising the time domain setup are connected to a common 10 MHz clock reference to ensure phase stability and operated by the home-made software package qKIT, freely available under Ref. [Qki20].

**Bias tee operation**

In this work, we employ a bias tee to combine dc and rf flux biases at the base stage. This allows for optimal filtering up until the sample of both input lines, tailored to their specific needs. Unfortunately, the capacitance $C$ on bias tee's rf input is accompanied by discharging effects, resulting in the decay of applied current pulses [Bra+16]. In the bias tee circuit, the capacitor discharges via the line resistance $R$, see Fig. 4.10(a).

Here, the goal is to find the voltage $V_{\mathrm{awg}}$ needed to drive a given current pulse $I$. Kirchhoff's law yields the the differential equation [Bra+16]

$$\dot{I} + \tau I = \frac{1}{R}\frac{\mathrm{d}}{\mathrm{d}t}V_{\mathrm{awg}} \tag{4.24}$$

for the current across the flux bias coil, with the time constant $\tau = 1/RC$. The general solution of the homogeneous differential equation reads $I_{\mathrm{p}} = I_0 \exp(t/\tau)$, where $I_0$ is arbitrary but constant. By inserting $I_{\mathrm{s}} = c(t) I_{\mathrm{p}}$ into Eq. (4.24), we infer

$$\frac{\mathrm{d}}{\mathrm{d}t}V_{\mathrm{awg}} = R I_{\mathrm{p}} \frac{\mathrm{d}}{\mathrm{d}t}\left(\frac{I_{\mathrm{s}}}{I_{\mathrm{p}}}\right). \tag{4.25}$$

Together with the solution of the homogeneous differential equation, the voltage needed to produce a given current pulse $I_{\mathrm{s}}$ at the sample is calculated from

$$V_{\mathrm{awg}} = R\left(I_{\mathrm{s}} + \frac{1}{\tau}\int I_{\mathrm{s}}\mathrm{d}t\right). \tag{4.26}$$

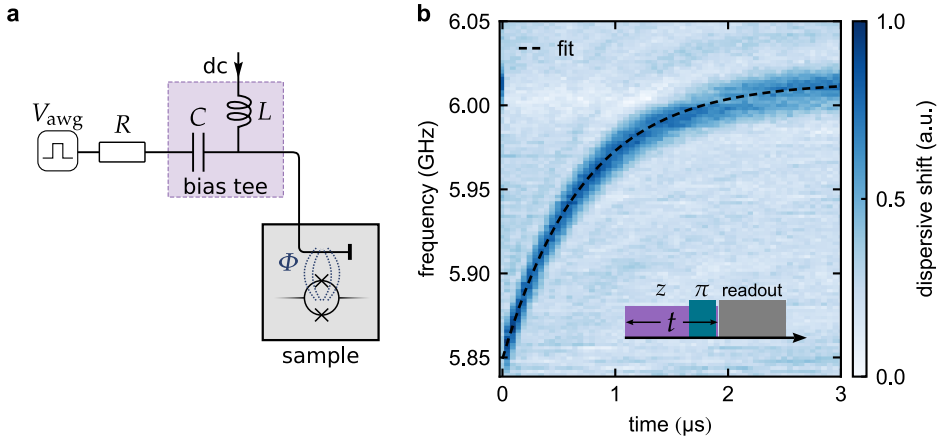


**Figure 4.10: Bias tee calibration.** (a) Circuit diagram of the bias tee. When applying a voltage $V_{\mathrm{awg}}$, the capacitor discharges via the inline resistance $R$. A large inductance $L$ is used to feed dc biases. This does not impair short pulses admitted via the rf line. (b) Measurement of the bias tee's time constant $\tau$. Applying a constant voltage results in an exponentially decaying current at the sample. We monitor the qubit frequency by probing the system with a $\pi$-pulse with variable frequency. The bias tee decay rate is inferred from the qubit frequency's trajectory as $\tau = (718 \pm 6)$ ns.

In the context of this work, two crucial special cases are

$$\begin{aligned} V_{\mathrm{awg}}^{\mathrm{c}} &= V_0 \frac{t}{\tau}, \\ V_{\mathrm{awg}}^{\mathrm{l}} &= v_0 \left( t + \frac{t^2}{2\tau} \right), \end{aligned} \tag{4.27}$$

which result in a constant and linearly increasing current bias, respectively. The total current through the on-chip coil is the sum of $I_{\mathrm{s}}$ and the dc current admitted to the bias tee.

Experimentally, there are several approaches to measure the time constant $\tau$ of the bias tee. For example, a constant voltage pulse can be applied to the bias tee, resulting in a current $I = I_{\mathrm{p}} + I_{\mathrm{dc}}$ at the sample. For a sufficiently linear dispersion (i.e., off sweet spot), the qubit frequency $\omega_{\mathrm{q}}$ follows an exponential function. The time constant $\tau$ can be extracted by monitoring $\omega_{\mathrm{q}}$, see Fig. 4.10. For the bias tee employed in this work, this yields $\tau = (718 \pm 6)$ ns. Particularly for "long" experiments (i.e., few micro-seconds), the voltage needed to maintain a constant electrical current exceeds the capabilities of the AWG. This can be a severe limiting factor.

# 5 Fabrication of quantum circuits with coherent Josephson junctions

A key ingredient for superconducting quantum circuits is a meticulous fabrication with a steadily growing library of techniques and materials. Qubit coherence can be improved drastically by optimizing the electrode material and growth, mitigating the detrimental influence of TLS. Currently, coherence times in the range of $10 - 300\,\mu s$ [Pai+11; Bar+13; Ner+19; Zha+20; Pla+20] allow for several hundred or thousand qubit gates [Kra+19; Kja+20]. Great efforts are also directed at establishing a scalable processing platform for quantum processors. This often boils down to streamlining the fabrication of Josephson junctions - the centerpiece of most superconducting qubits - while maintaining or improving qubit coherence [Wu+17; For+19b; Kre+20; Tsi+20].

I start this chapter with a brief introduction into basic cleanroom techniques needed to fabricate the quantum circuits presented in this work. Next, I summarize my implementation of airbridges, following the work of Chen *et al.* [Che+14], at our local cleanroom facility. Finally, I discuss the contents of Stehli *et al.* [Ste+20]: a scalable fabrication method for Josephson junctions developed in the context of this thesis.

## 5.1 Fabrication of thin film circuits

Many fabrication tools and techniques for superconducting circuits are adapted from well-established processes of the semiconductor industry, including film growth and patterning, which are discussed in this section. All samples measured in the context of this thesis were fabricated in the Nanostructure Service Laboratory with partial support from the technical staff.

### Film growth

Growing thin films of pristine quality is important to build superconducting qubits with low loss and decoherence rates, since impure or contaminated metals promote TLS. However, if proper precautions are taken to reduce residues, TLS are suppressed, to the benefit of qubit coherence and energy lifetime [Pla+20].

In this work, we utilize aluminum (Al), which is superconducting below 1.2 K, for all circuit elements including the Josephson junctions (JJ). Due to its reactivity, aluminum films (and bulk Al) immediately form an $AlO_x$ oxide layer, when exposed even to small quantities of oxygen. This makes aluminum ideal for generating the superconductor-insulator-superconductor (Al-$AlO_x$-Al) interface of a JJ. Furthermore, the inert oxide film acts as a protective layer for the film, preventing corrosion.

For film growth, our substrate of choice is c-plane sapphire ($\epsilon_r^c \approx 11.5$) at a thickness of $\sim 430\,\mu m$. We grow aluminum films in high vacuum ($\sim 10^{-8}$ mbar) in a Plassys$^{TM}$ MEB 550S shadow evaporation machine. Here, the Al is melted and evaporated from a crucible using an electron-beam. We ensure a clean metal-substrate interface by piranha cleaning the sapphire substrate before processing the wafer. The deposition rate of 1 nm/s is monitored by a quartz crystal oscillator. Apart from the obvious advantage of faster processing, a larger rate also results in more homogeneous aluminum films [Fri+19].

### Thin film patterning

Metal films can be structured with either lift-off or etching technologies, both of which rely on electron or optical lithography. Here, a polymer resist, comprising reactive components, is thin- and evenly spread across a chip with a spin coater. Exposure to either UV-light or an electron-beam activates a chemical reaction. Depending on the resist, this leads to poly- (negative resist) or de-polymerization (positive resist). By applying a developer short molecules are dissolved, leaving photo resist only at the exposed area (negative) or its counterpart (positive). A schematic diagram of optical lithography is displayed in Fig. 5.1(a). While electron-beam exposure is significantly slower and more expensive, the shorter wavelength enables smaller feature sizes. This is particularly important for structuring Josephson junctions. Technical details on optical and electron-beam lithography are listed in Appendix D.

In a lift-off process, the wafer is covered with metal after lithography. Subsequently, the resist is dissolved leaving a metallic negative of the mask, see Fig. 5.1(b). In

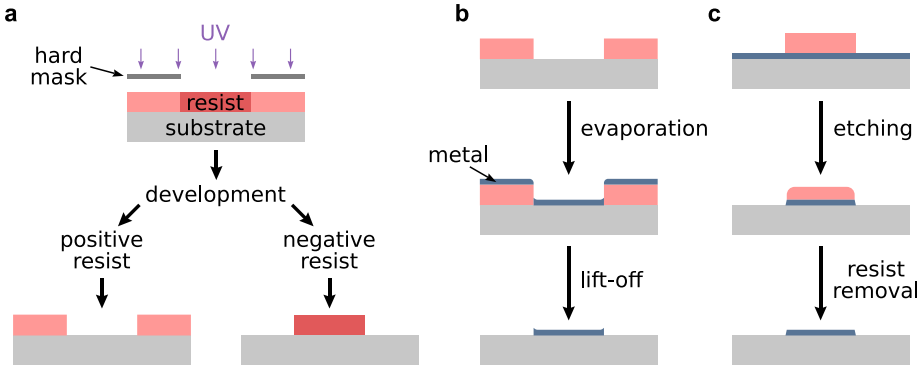


**Figure 5.1: Thin film patterning technologies.** (a) Flow diagram of optical lithography. Developing positive resist removes the polymers on exposed areas. For negative resist it is the opposite. Flow diagram of film patterning by lift-off (b) and etching (c).

**Table 5.1: Parameters for reactive ion etching**. Gas flow is given in $cm^3/min$. Rf-power for plasma generation ($P_{ICP}$) and acceleration ($P_{acc}$) are individually adjustable.

| type | Ar (sccm) | Cl (sccm) | $O_2$ (sccm) | $P_{ICP}$ (W) | $P_{acc}$ (W) |
|---|---|---|---|---|---|
| e-beam litho. | 15 | 2 | - | 100 | 100 |
| optical litho. | 15 | 3 | 1 | 100 | 100 |
| AB litho. | 12 | 2 | - | 100 | 100 |
| AB res. burn | 15 | - | 15 | 50 | 100 |

subtractive patterning, the film is applied first and removed by etching wherever it is not protected by the structured resist, see Fig. 5.1(c). Compared to lift-off, this results in more pristine substrate-metal interfaces, since no resist was present during the deposition.

Therefore, in this work, structures are transferred from resist masks by reactive ion etching, using an inductively coupled plasma, generated in an Oxford Instruments$^{TM}$ Plasmalab 100 ICP. Here, the plasma is generated and accelerated by a microwave-field with power $P_{ICP}$ and $P_{acc}$, respectively. It is composed of argon, chlorine, and, for optical lithography, oxygen ions. Table 5.1 comprises the parameters of the processes relevant to this work. After etching, resist residues are removed in acetone and N-ethyl-pyrrolidone (NEP) baths, assisted by ultrasonic cleaning. A detailed list of the parameters of the cleaning process can be found in Appendix D.

## 5.2 Airbridges for quantum circuits

As their name suggests, airbridges (ABs) are microscopic constructs connecting two metal slabs. They are employed to ensure a proper galvanic connection of the CPW ground planes. Therefore, they are a crucial ingredient for reducing crosstalk and suppressing unwanted slotline modes, see Sec. 4.3.1. This is especially important for densely packed circuits, such as those investigated in Sec. 6.

Our adaptation of ABs in the local cleanroom facility closely follows the work of Chen *et al.* [Che+14]. A flow diagram of the fabrication process is displayed in Fig. 5.2. The bridge pedestals are generated using optical lithography of a $\sim 3\,\mu m$ thick optical resist (AZ5214E). The bridge arc is shaped with a flow bake at 130 °C for 60 seconds. The ABs are formed from a 350 µm thick aluminum metallization. Here, galvanic contact to the ground plane is ensured by in-situ argon ion beam milling directly before metal deposition [Grü+17]. The resist mask for etching the bridge structure is generated again from a $\sim 3\,\mu m$ thick optical resist, which enhances the mask's uniformity. After the development, the ABs are defined with

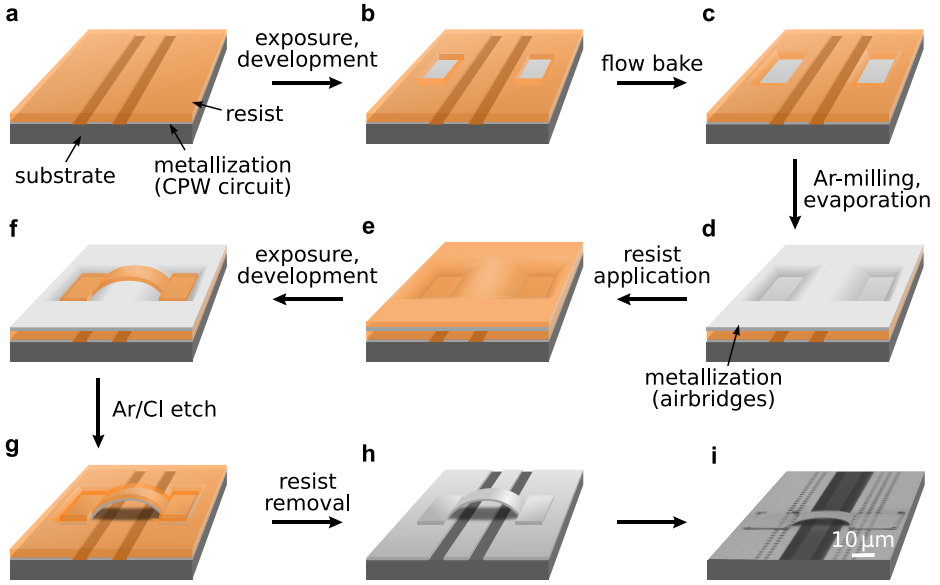


**Figure 5.2: Flow diagram for airbridge fabrication.** (b) The mask for the bridge pedestals and arc are formed from optical resist and shaped with a flow bake (c). (d) The galvanic connection of the 350 µm thick aluminum metallization producing the air bridge is ensured by an argon milling process [Grü+17]. (e,f) Using optical lithography, the mask for the bridge is patterned and transferred to the metal with an Ar/Cl plasma (g). (h) The remaining resist is removed in a heated bath NEP.

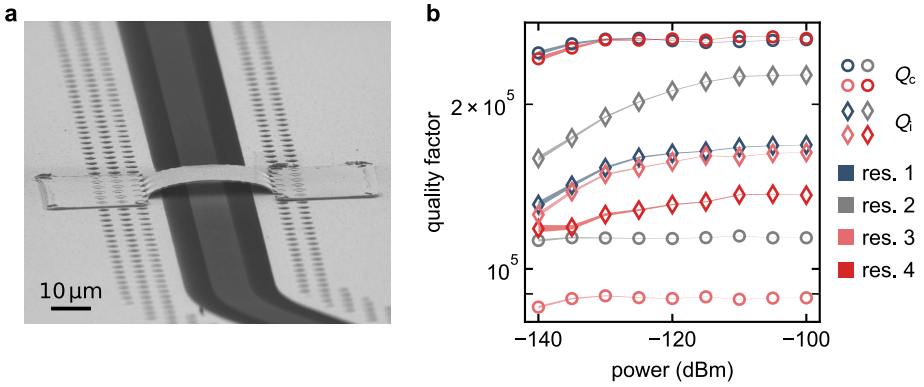


**Figure 5.3: Airbridges in the experiment.** (a) SEM image of an airbridge. ABs ensure a galvanic connection of the ground plane(s) next to a CPW resonator. During the electron microscopy, the (floating) $\lambda/2$-resonator accumulates charges, reducing its brightness compared to the ground plane. (b) Coupling and internal quality factors of CPW resonators. Fit errors from the circle fit, see Sec. 4.3.3, are indicated by the shaded areas. Since $Q_c$ is solely determined by the geometry, it is approximately power independent. Due to the saturation of surface TLS, $Q_i$ improves slightly with increasing input power.

an AR/Cl plasma etch. The resist is removed using an Ar/O plasma in the same device, followed by a 90 °C NEP bath for several hours. The process parameters of the etch process for patterning and resist removal are listed in table 5.1.

Utilizing scanning electron microscopy (SEM), we confirm that the resist is completely removed by the cleaning procedure, both under and on top of the bridge, see Fig 5.3(a). The ABs are extremely stable: Across multiple samples, we have yet to find a single broken or collapsed bridge. In low temperature measurements, we investigate the quality factors of five resonators with airbridges, see Fig 5.3(b). Here, we find decent $Q_i$, which are enhanced for increasing input power. A likely cause is the saturation of surface TLS [Bre+17]. The presented results are comparable to those of our resonators without airbridges.

## 5.3 Coherent superconducting qubits from a subtractive junction fabrication process

*"Josephson tunnel junctions are the centerpiece of almost any superconducting electronic circuit, including qubits. Typically, the junctions for qubits are fabricated using shadow evaporation techniques to reduce dielectric loss contributions from the superconducting film interfaces. In recent years, however, sub-micron scale overlap junctions have started to attract attention. Compared to shadow mask techniques, neither an angle dependent deposition nor free-standing bridges or overlaps are needed, which are significant limitations for wafer-scale processing. This comes at the cost of breaking the vacuum during fabrication, but simplifies integration in multi-layered circuits, implementation of vastly different junction sizes, and enables fabrication on a larger scale in an industrially-standardized process. In this work, we demonstrate the feasibility of a subtractive process for fabrication of overlap junctions. In an array of test contacts, we find low aging of the average normal state resistance of only 1.6% over 6 months. We evaluate the coherence properties of the junctions by employing them in superconducting transmon qubits. In time domain experiments, we find that both, the qubit life- and coherence time of our best device, are on average greater than 20 µs. Finally, we discuss potential improvements to our technique. This work paves the way towards a more standardized process flow with advanced materials and growth processes, and constitutes an important step for large-scale fabrication of superconducting quantum circuits."* - Stehli *et al.* [Ste+20]

### 5.3.1 Josephson junction fabrication

Josephson junctions (JJ) are the centerpiece of almost all superconducting quantum circuits. In qubits, these nonlinear elements are used to isolate two distinct energy levels, usually ground and first excited state, which are then operated as logical states for quantum computation or simulation. Currently, all technologies used to produce the superconductor-insulator-superconductor interface of the JJ rely on lift-off processes. The widespread shadow-evaporation techniques exploit free-standing bridges [Dol77] or overhangs [Lec+11] in conjunction with multi-angle evaporation to generate the JJ in situ.

In the commonly used shadow-evaporation processes, free-standing bridges [Dol77] or overhangs [Lec+11], and multi-angle evaporation are exploited to generate the desired interface in situ in a single process step. Due to the angle-dependence, the direction the material is evaporated from is critical. Thus, only point-like evaporation sources with inhomogeneous deposition can be utilized, limiting the applicable JJ materials. Typically, polymer resist masks are used in favor of hard

masks [Dol+03; Tsi+20]. Therefore, only superconductors with low melting points are applicable. Additionally, outgassing of the resist mask can deteriorate the JJ. Last but not least, shadow-evaporation processes (with a point-like source) come at the cost of a systematic angle-dependent parameter spread. Especially for larger wafers, great efforts are needed to mitigate this effect [For+19b; Kre+20].

An alternative technology are overlap JJ generated in a two-step process. Historically, dielectric loss in superconducting qubits with micron sized overlap JJ was a severe limiting factor to qubit life- and coherence times [Ste+06; Wei+11b; Bra+15]. This had initially motivated the application of electron-beam lithography, also for shadow-evaporation techniques, which enables JJ with smaller feature size and therefore lower loss [Mar+05; Wei+11a]. Recently, it was shown that qubits with nanoscaled overlap contacts are indeed competitive with in situ fabricated JJ from angle-dependent processes [Wu+17]. However, this process established by Wu and colleagues still relies on lift-off patterning which can impair the fabrication yield and is a potential source of contamination of the Josephson junction [Pop+12; Qui+14].

Structuring the JJ subtractively rather than by lift-off has several merits: First of all, resist is completely eliminated from the processing chamber and the JJ vicinity. Particularly, the superconductor-insulator-superconductor interface is generated in complete absence of polymer resist. This opens the door to previously disregarded deposition methods, like the addition of reactive gases to the evaporation chamber. With the removal of both angle-dependence and the restrains on temperature, the choice of material is practically free of restrictions. The same goes for their growth mode: For example, epitaxial growth of the JJ can be explored [Fri+19]. Especially in the light of recent studies, it becomes evident that superconducting qubits can still benefit from exploring new types of materials [Pla+20]. Generally, subtractive patterning concurrently allows for smaller, more coherent, as well as larger JJ. On the one hand, etching can result in a reduced feature size compared to lift-off technologies. On the other hand, unlike for shadow evaporation techniques, there is no upper limit for junctions with a large area, which are typically employed in quantum amplifiers [Roc+12; Mac+15; Win+20]. In principle, small and large contacts can even be patterned on a common wafer and in parallel by the same process steps. In conjunction with the angle-independence, this enables full scalability and integration into a streamlined and large-scale processing platform for arbitrary quantum circuits.

### 5.3.2 Subtractive Al-AlO$_x$-Al Josephson junctions

In the context of this thesis, we implemented a subtractive fabrication process and demonstrated its capabilities at hand of Al-AlO$_x$-Al Josephson junctions. Due to its compatibility with standardized nanofabrication methods, our process constitutes an important ingredient for large-scale fabrication of superconducting quantum processors [Ste+20].

Figure 5.4 displays a flow diagram of our JJ fabrication process. First, a sapphire wafer is prepared as described in Sec. 5.1, with a 50 nm aluminum film. From this Al layer both, the JJ bottom electrode and the main structures of the circuit are defined. This is beneficial for two reasons: First of all, it saves time, since an additional evaporation step can be omitted. Secondly, without preceding process steps, the first metal layer on the wafer has the highest quality. Particularly, the capacitor electrodes, where most a circuit's electrical field accumulates, profit from a low TLS density. For patterning the bottom electrode of the JJ, electron-beam lithography with a $\sim 180$ nm thick PMMA resist provides a polymer mask for the subsequent subtractive process. In principle, the choice of resist is flexible, if it musters a sufficiently large resistance to the etch-plasma. However, employing a positive resist decreases electron-beam writing times. As described in Sec. 5.1, an Ar/Cl-plasma is used to transfer the structures from the resist to the aluminum film, followed by ultrasonic cleaning in an NEP bath. A proper removal of resist residues is crucial for high quality JJ.

The top electrode is applied in a Plassys$^{\text{TM}}$ MEB550S, capable of milling and oxidizing the bottom layer in situ before evaporation. Any remaining resist residuals are incinerated by an Ar/O plasma. For a controlled growth of the tunnel barrier, it is crucial to remove the native oxide of the first Al layer, which is achieved by Ar sputtering for 180 seconds [Grü+17]. The tunnel barrier is grown in quick succession by admitting a continuous flow of 12 sccm $O_2$ to the load lock, while keeping a chamber pressure of $p_{\text{LL}} \approx 0.0195$ mbar. This yields a rough estimation of the oxidation time needed to achieve a given critical current [KMM95]. Next, an 80 nm thick aluminum layer is deposited, as described in Sec. 5.1. The top electrode of the JJ is structured using electron-beam lithography and an Ar/Cl plasma. Apart from the duration of the plasma, this process is identical to the patterning of the bottom layer. Finally, larger circuit elements of the sample can be structured from the first Al layer, for example, utilizing optical lithography. Note that the process also introduces a stray junction to the sample. The additional dielectric loss and coupling to TLS can impair qubit life-, and coherence times [Lis+19]. This effect is reduced by shorting the stray JJ with a bandaging technique [Dun+17].

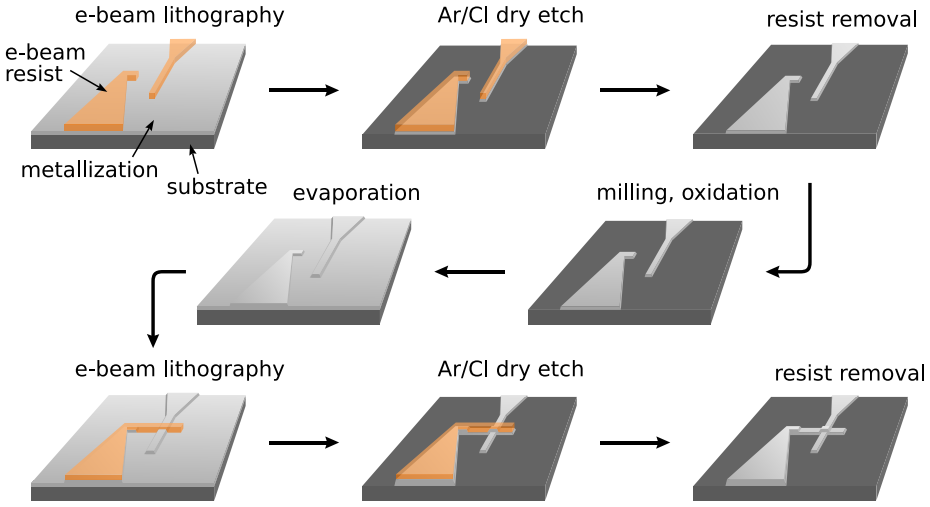


**Figure 5.4: Flow diagram of the subtractive JJ fabrication process.** We pattern both JJ electrodes using electron-beam lithography and an Ar/Cl plasma. Before depositing the top electrode, we perform argon ion milling to remove native oxides. This allows us to grow the $AlO_x$-tunnel barrier in a controlled environment. Figure adapted from Ref. [Ste+20].

Finally, structuring the JJ electrodes with electron-beam lithography, needed to achieve small feature sizes, is both expensive and time-consuming. However, in contrast to shadow-evaporation techniques, our processing platform is ab initio compatible with modern fabrication tools, such as the extreme ultraviolet lithography used in the semiconductor industry [Bak08]. This makes our technique ideal for large scale fabrication of superconducting quantum circuits.

### 5.3.3 Room temperature characterization

Figure 5.6(d) displays an SEM micrograph of a JJ, fabricated from our subtractive process. In comparison to the design parameters, we find a process bias of $\sim 10\%$ towards reduced junction edge width. A likely cause is isotropic etching of the film due to the chlorine, resulting in sloped side-walls and under-etching of the aluminum films. Employing thinner metal films would reduce the exposure to the Ar/Cl-plasma and thereby mitigate the aforementioned effects. As a result, thinner masks with reduced etch resistance can be used. This allows for a better resolution and smaller feature size, reducing loss in the junction.

As described in Sec. 2.2, a Josephson junction's normal state resistance $R_\mathrm{n}$ at $T = 0$ is inversely proportional to its critical current $I_\mathrm{c}$, see Eq. (2.4). Here, $R_\mathrm{n}$ is dominated

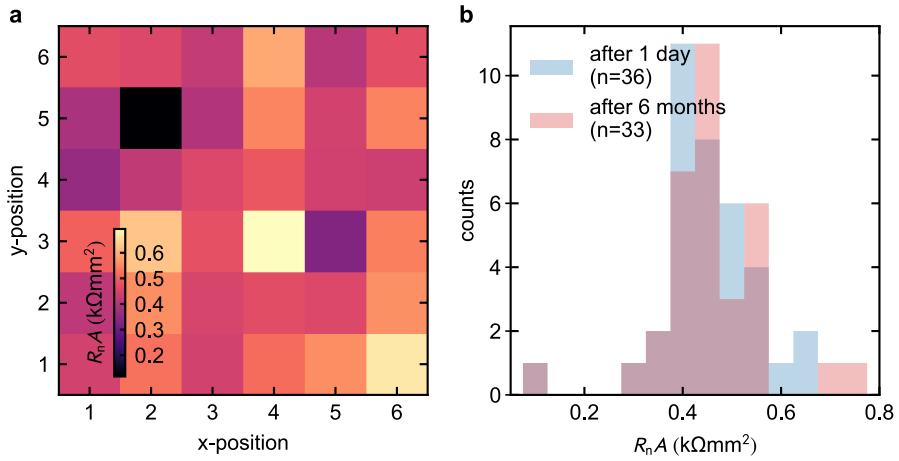


**Figure 5.5: Room temperature resistance the test JJ.** (a) Resistance variations of the test junctions across the wafer. The resistance is normalized to the JJ area which is varied from 150 nm to 300 nm in 50 nm increments. We find a slight gradient from the top left to bottom right corner of the wafer. Potential causes are an unisotropic oxidation, development, or variations during electron-beam writing [Kre+20]. (b) Histogram of the resistance area product ($R_nA$). After $\sim$ 6 months of aging in ambient conditions, $R_nA$ increases by only 1.6%, indicating a clean JJ barrier. Figure adapted from Ref. [Ste+20].

by the tunnel resistance of the JJ and thus approximately temperature independent. Therefore, room temperature characterization is an established method to estimate a junction's critical current and its spread across a wafers.

For this purpose, we prepared a test wafer featuring a $6 \times 6$ grid of JJ, fabricated in the same batch as the qubits, see Sec. 5.3.4. The JJ area was varied from 150 nm to 300 nm in 50 nm increments, which are evenly distributed across the array. Due to the large resistance of our JJ ($> 4\,\mathrm{k}\Omega$), a two-point measurement provides sufficient accuracy to determine $R_n$. Across the 36 test contacts, we find an average normal state resistance times area product of $R_nA = (0.474 \pm 0.099)\,\Omega\,\mathrm{mm}^2$. A slight gradient across the wafer indicates inhomogeneities, see Fig. 5.5(a), potentially caused by unisotropic oxidation, development, or variations during electron-beam writing [Kre+20]. Otherwise, the resistance spread is comparable to established technologies, before a meticulous optimization of the process parameters. The $\sim$ 20% spread in the normal state resistance is likely caused by the under-etching, in particular, the nonuniformity it introduces to the edges of the JJ. Due to the relatively large film thickness, these edges constitute $\sim 25 - 40\%$ of the total JJ area. Again, this effect can be addressed by employing thinner metal films for both, top and bottom electrode.

Another vital aspect is JJ aging, that is, unwanted drifts of a junction's critical current with time. Figure 5.5(b) shows a histogram of the normal state resistance, immediately after fabrication and after $\sim 6$ months of aging in ambient conditions. Neglecting measurement inaccuracies, we find $R_\mathrm{n}A = (0.482 \pm 0.108)\,\mathrm{k\Omega\,mm^2}$ on average, which amounts to an increase of $R_\mathrm{n}$ of only 1.6% over this period. Aging is presumed to be driven by resist residues within the JJ [Pop+12]. The low aging observed in our devices is a strong indicator of clean JJ interfaces. This long-term stability further promotes our platform for the fabrication quantum processors on a larger scale. The low aging is confirmed by the long-term stability of our qubits' transition frequencies, see Appendix E.

### 5.3.4 Qubit measurements

We prepared a sample comprising a total of four transmon qubits, embedded in a coplanar microwave environment. All qubit junctions are fabricated using the subtractive process described in Sec. 5.3.2. However, the top electrode is applied only in a small window above the JJ, using a lift-off process with S1805 (optical) resist. Thereby, electron-beam exposure time is reduced. Furthermore, an internal $AlO_x$-layer in all structures which could be detrimental to qubit coherence and the readout resonators' $Q_\mathrm{i}$ is avoided. We note that the lift-off step is not mandatory, as the same result can be achieved by utilizing a negative tone resist. In any case, the edges of the optical window are far away from the JJ. The main structures, including resonators, transmission line, and qubit electrodes are patterned with optical lithography using S1805 resist and an Ar/Cl/O-plasma, for details, see Sec. 5.1. Here, the resist mask also protects the JJ from exposure to the plasma. Airbridges ensure a good galvanic connection of the ground plane and suppress slotline modes.

An overview of the sample is displayed in Fig. 5.6(a). Here, two of the qubits feature an interdigitated capacitor (devices $q_1$ and $q_2$), see Fig. 5.6(b), while the other two are of a concentric design [Bra+16] (devices $q_3$ and $q_4$), see Fig. 5.6(c). Each qubit is capacitively coupled to a dedicated $\lambda/4$-resonator for dispersive state readout, which is addressed in reflection measurements. The parameters of the underlying Jaynes-Cummings model are summarized in table 5.2.

In time domain measurements, see Sec. 4.5.2 for a schematic diagram of the setup, we characterize the lifetime $T_1$, Ramsey decay time $T_2^*$, and spin-echo decay time $T_2$ of all qubits. Here, we implement an interleaved measurement scheme where the data is taken simultaneously, alternating between the three experiments. This allows us to resolve fluctuations of the qubit frequencies, life-, and coherence times, slower than the repetition rate [Sch+19; Bur+19; Hon+20]. Here, $10^3$ point averages

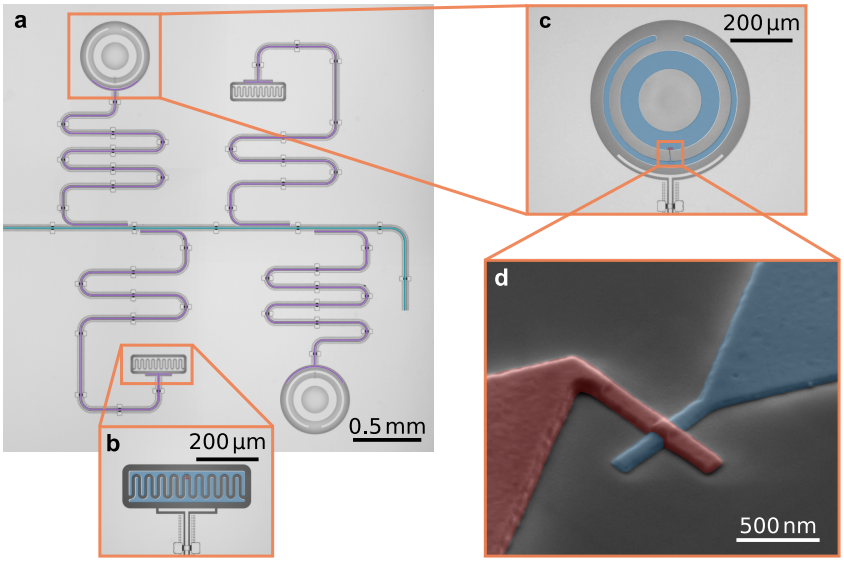


**Figure 5.6: Qubit microchip.** (a) Overview of the sample. Each qubit is capacitively coupled to a microwave resonator for dispersive state readout via the on-chip transmission line. In total, the sample comprises two transmon qubits with interdigitated capacitors (b) and two concentric transmons (c). The qubit capacitors and bottom electrode are structured from the same metal layer (blue). (d) SEM micrograph of the overlap junction. The JJ electrodes (blue and red) are 180 nm wide, which is $\sim$ 10% less than the designed value. Figure adapted from Ref. [Ste+20].

**Table 5.2: Device parameters in MHz.** This includes the qubits' first transition frequency $\omega_q$ and the frequencies $\omega_r$ and linewidths $\kappa_r$ of the readout resonators. For each device, the qubit anharmonicity $\alpha$ is determined from a spectroscopy measurement. The coupling strength $g$ to the first qubit transition is calculated from the decoupling shift $\chi_{01}$ of the readout resonator, see Eq. 3.41. Data published in Ref. [Ste+20].

| device | $\omega_r/2\pi$ | $\kappa_r/2\pi$ | $\omega_q/2\pi$ | $\alpha/2\pi$ | $\chi_{01}/2\pi$ | $g/2\pi$ |
|---|---|---|---|---|---|---|
| $q_1$ | 6460 | 1.579 | 3548 | −257 | 0.915 | 47.5 |
| $q_2$ | 6632 | 0.524 | 3950 | −262 | 0.514 | 45.6 |
| $q_3$ | 6462 | 1.306 | 3161 | −294 | 0.350 | 50.6 |
| $q_4$ | 6457 | 0.184 | 3324 | −300 | 0.774 | 49.3 |

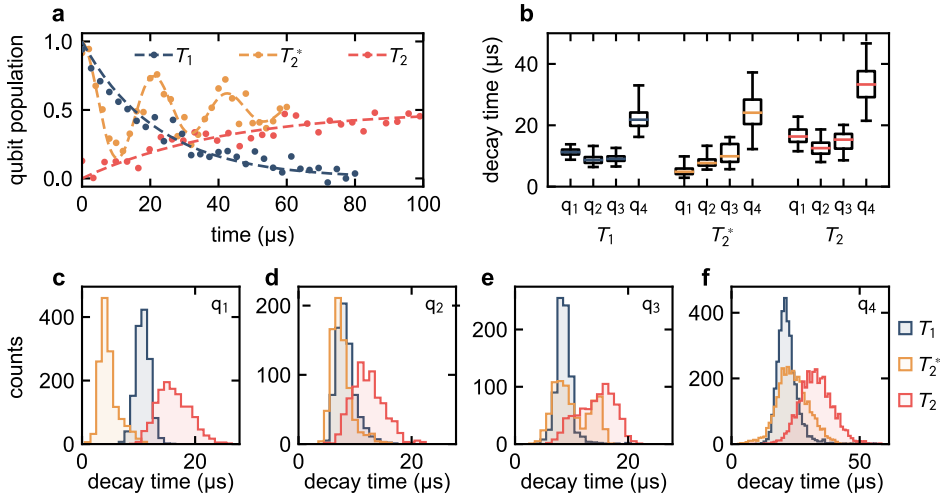


**Figure 5.7: Qubit performance in time domain experiments.** (a) Qubit population of a typical measurement set for $T_1$, $T_2^*$, and $T_2$. From fits (dashed lines), we find a lifetime of $T_1 = (22.0 \pm 0.9)$ µs, and coherence times $T_2^* = (30.1 \pm 3.7)$ µs (Ramsey experiment) and $T_2 = (42.3 \pm 2.9)$ µs (spin-echo experiment). (b) Box plot of each qubit's life-, and coherence times, collected over several hours. The box encloses the second and third quartile, whereas the whiskers indicate $2\sigma$, i.e., 95% of the data. The median of each data set is indicated by a colored line. (c-f) Histograms of the qubits' life-, and coherence times. Decay times of devices $q_1$, $q_2$, and $q_4$ approximately follow a normal distribution. Two meta-stable states, one with low and another with high coherence, indicate the presence of a TLS close to the resonance frequency of $q_3$. Figure adapted from Ref. [Ste+20].

**Table 5.3: Parameters of the time domain measurements.** Overview of the measurement duration, total number of measurements $N_{\text{tot}}$, and successful number of measurements $N$. Data published in Ref. [Ste+20].

| device | measurement duration (h) | $N_{\text{tot}}$ | $N$ |
|---|---|---|---|
| $q_1$ | 29.8 | 1700 | 1589 |
| $q_2$ | 17.6 | 2000 | 1382 |
| $q_3$ | 35.3 | 2502 | 1744 |
| $q_4$ | 69.6 | 10337 | 7013 |

result in an acquisition time of $\sim$ 30s for a measurement set of $T_1$, $T_2^*$ and $T_2$, see Fig. 5.7(a) for a typical time trace.

We monitor the coherence properties of each qubit for an extended time ($> 16$ h), see table 5.3. In the analysis, we exclude unphysical data sets, where $T_2, T_2^* > 2T_1$ or $T_2^* > T_2$. Likely causes are fast qubit fluctuations during the measurement or fit errors due to a low SNR. Additionally, data sets with a fit uncertainty exceeding

**Table 5.4: Average qubit performance.** Overview of the qubits' median lifetime $\tilde{T}_1$, and median coherence times $\tilde{T}_2^*$, and $\tilde{T}_2$ in µs, extracted from the data displayed in Fig. 5.7(b). Data published in Ref. [Ste+20].

| device | $\tilde{T}_1$ | $\tilde{T}_2^*$ | $\tilde{T}_2$ |
|---|---|---|---|
| $q_1$ | 11.3 | 4.9 | 16.3 |
| $q_2$ | 8.7 | 7.7 | 12.5 |
| $q_3$ | 9.0 | 9.9 | 15.3 |
| $q_4$ | 21.8 | 24.1 | 33.3 |

50% are excluded.[1] The accumulated results are displayed in Fig. 5.7(b) as a box plot. We find decent life-, and coherence times of all qubits, on the order of several microseconds, see table 5.4. For each qubit, Fig. 5.7(c-f) displays histograms of $T_1$, $T_2^*$, and $T_2$, which mostly follow a normal distribution. The coherence time distribution of $q_3$ hint towards the existence of two states, one with high and another one with low coherence. This is an indicator for a TLS in close proximity (in frequency space) to the qubit's transition frequency [Sch+19; Bur+19].

Regarding qubit performance, life-, and coherence times of transmon $q_4$ are significantly higher than those of $q_1 - q_3$. With optical microscopy, we identify aluminum residues in the JJ vicinity as a probable cause. Otherwise, the coherence properties of our best device ($q_4$) approach those of qubits with JJ stemming from a lifted overlap or shadow evaporation technique. State of the art transmons still perform better by a factor of $\sim 5 - 10$. Closing the gap needs further improvements of our circuits, for example, a reduction of surface loss [Gam+17], shunting the stray JJ with a bandaging technique [Dun+17], or an optimization of the qubit electrode material [Pla+20].

### 5.3.5 Qubit identification

Due to a sizable deviation of the experiment from the microwave simulations, it proves challenging to identify which readout resonator belongs to which qubit. On another sample from the same fabrication run, we shifted the frequency of the readout resonators, thereby identifying the corresponding qubit. For this purpose, a droplet of varnish was applied on top of the resonator, see Fig. 5.8(a). The large electric permittivity of the varnish increases the capacitance of the resonator, reducing its frequency. Figure 5.8(b, c) displays the reflection spectrum of the

[1] This mostly affects data sets with extremely long $T_1$ or $T_2$

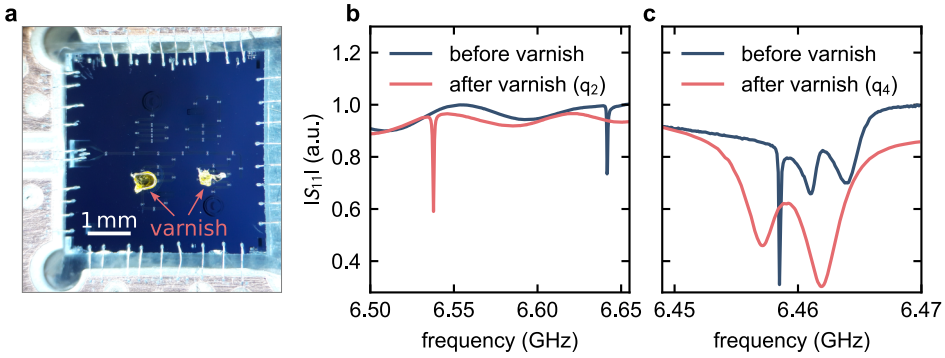


**Figure 5.8: Varnish induced shift of the readout resonator frequencies.** (a) In order to identify the the qubits, we shift the frequency of one readout resonator by applying a drop of varnish and identify the change in the reflection coefficient $|S_{11}|$. (b) Shift of the highest frequency resonator. The varnish was applied to the readout resonator of a qubit with interdigitated capacitor. (c) Subsequently, the lowest frequency resonator was shifted, thereby revealing that the corresponding qubit is a concentric transmon. Figure adapted from Ref. [Ste+20].

sample with and without the varnish, which is applied, one resonator at a time, in consecutive cooldowns. We repeated this process for two resonators and inferred the remaining qubit-resonator pairs from the qubit anharmonicity, see table 5.2.

### 5.3.6 Conclusion

In this chapter, we present a subtractive fabrication platform for coherent Josephson junctions. As described in Sec. 5.3.1, subtractive patterning of the JJ has several advantages over lifted overlaps or shadow evaporation: Our process has no restrictions on the junction size and is angle independent, which is integral for a scalable fabrication platform. A negligible aging of our JJ indicates clean superconductor-insulator-superconductor interfaces, which is owed to the elimination of a resist mask in close proximity to the junctions during the evaporation. Therefore, material deposition at elevated temperatures or in reactive gases becomes possible. This can be exploited to investigate different growth modes and materials, other than the ubiquitous Al-$AlO_x$-Al stacks, for the JJ electrodes, with potential benefits to qubit coherence. While the contacts presented in this work are of average size, subtractive patterning in general allows for smaller and, thereby, more coherent JJ compared to lift-off processes.

Qubits made with our process feature life-, and coherence times competitive with existing technologies, which we establish at hand of four transmon qubits, in an extended time domain characterization. On average, both energy loss and

decoherence time of our best device exceed 20 µs. In conjunction with its scalability, this makes our technology an important ingredient for a streamlined and large scale fabrication of superconducting quantum circuits.

# 6 Quantum simulation of the multistate Landau-Zener model

Universal quantum computing promises an exponential computational advantage at selected tasks, compared to current computers based on classical logic. While these devices are still a long way down the road, noisy intermediate-scale quantum (NISQ) technologies offer a quantum advantage over classical systems in the near future [Pre18]. Particularly, analog quantum simulation (AQS) has advanced rapidly over the last years and can, even with today's imperfect qubits, tackle problems which are hard to solve, even for modern supercomputers [Ber+17; Zha+17]. Open quantum systems are of exceptional interest for AQS: In nature, any quantum system is coupled to its environment, resulting in energy decay and decoherence of the quantum state [Man20]. AQS can be used to model these open quantum systems and thereby gain unique insights into the underlying loss mechanisms. Furthermore, the simulation of open quantum systems offers a platform to study non-Markovian physics [OIL13; Pue+19]. Last but not least they are a challenging problem, even for digital quantum computers [GRM20]. The multistate Landau-Zener model is such a system, where a two-level atom traverses several or a continuum of bosonic modes, forming its spectral environment.

This chapter begins with a short introduction to AQS, especially in the context of open quantum systems. Thereafter, I briefly introduce the Landau-Zener model, which, when expanded to the multistate case, is a special case of the Spin-Boson model. In the following sections, I pave the way towards the AQS of this model, starting with the simulation device and its characterization in spectroscopy and time domain measurements. Experimentally, the multistate Landau-Zener model, in particular the qubit's time evolution, is studied depending on the system initialization. Throughout this chapter, the experimental results are backed with numerical simulations. Finally, I conclude the chapter with a summary of the findings and give a short outlook on future plans of AQS of open quantum systems.

## 6.1 Analog quantum simulation of open quantum systems

AQS is in stark contrast to quantum computation. Rather than employing gate-based operations to derive the result of a calculation, analog simulators rely on the intrinsic time evolution dictated by the Schrödinger equation. The principle is rather simple, see Fig. 6.1(a): An analog simulator synthesizes a Hamiltonian, which maps onto that of the quantum system under investigation. Ideally, the simulator can be prepared in an arbitrary initial state and a projective measurement yields its current state at any given time. By reversing the mapping, the time evolution of the simulated system is inferred [GAN14]. This approach is particularly relevant if the original system is hard or impossible to measure. Although analog quantum simulators can be susceptible to external perturbations and suffer from inaccuracies with respect to the implemented model, they allow for solid qualitative studies, especially of universal effects [Pre18]. This makes AQS ideal to study open quantum systems.

Every real quantum system couples to an environment of some sort and is therefore an open quantum system. The goal of open quantum theory is to describe the dynamics of a system of interest, without having to solve the equation of motion

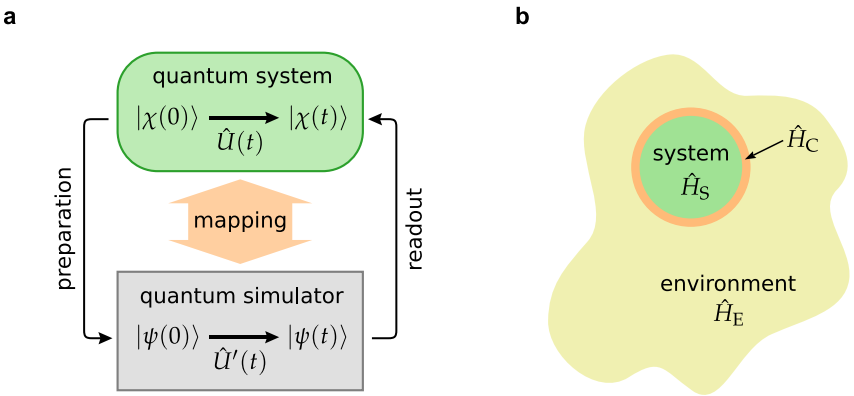


**Figure 6.1: AQS of open quantum systems.** (a) Flow diagram of AQS. The Hamiltonian of the simulator maps onto that of the model system it synthesizes, which is therefore also true for the time evolution with the operator $\hat{U}'$ and $\hat{U}$, respectively. State preparation and readout of the quantum simulator in conjunction with the mapping allows to infer the time evolution of the system of interest and to study its properties. (b) Schematic diagram of an open quantum system. The system of interest ($\hat{H}_S$) is coupled to its environment ($\hat{H}_E$) via the Hamiltonian $\hat{H}_C$. In open quantum theory, the time evolution of the environment is truncated. For example, this introduces effective dissipation rates for energy and coherence to the eigenstates of $\hat{H}_S$, see Sec. 3.2.1.

of the surrounding environment [Man20]. This problem, sketched in Fig. 6.1(b), is often addressed by the Lindblad equation, see Sec. 3.2.1. By using AQS, a system of interest, e.g., a qubit, can be directly studied in the presence of a tailored environment. Herewith, a more profound understanding of the loss mechanisms and dynamics in real systems can be gained. Depending on the coupling regime, AQS also offers the possibility to simulate challenging and exciting open systems phenomena. For example, a simulator with ultra-strong coupling [Lep+18; For+19a] between a qubit and several bosonic modes enables the investigation of the Kondo effect [Leg+87; Le 12; Gol+13], proton transfer reactions in the presence of solvents [CM89], and allows to study non-Markovian physics [Pue+19].

## 6.2 The Landau-Zener model

The Landau-Zener model describes the transition dynamics of at least two coupled quantum states, where an order parameter is used to tune the energy separation of the states linearly with time [Lan32; Zen32; Stü32]. Due to its simplicity and generality, the model has a wide range of applications. For example, it is used to model molecular collisions [Chi96] and chemical reaction dynamics [Nit06]. It is also ubiquitous in cQED, where the underlying Jaynes-Cummings model produces an avoided crossing of qubit and readout resonator [Bla+04; Wal+04]. This can be expanded to the interaction with not one, but several bosonic modes. The Hamiltonian of the multi-mode system reads

$$\frac{\hat{H}_{\mathrm{LZ}}}{\hbar} = \frac{vt}{2}\hat{\sigma}_z + \sum_n \omega_n \hat{a}_n^\dagger \hat{a}_n + g_n \hat{\sigma}_x \left(\hat{a}_n^\dagger + \hat{a}_n\right), \tag{6.1}$$

where $v$ is the Landau-Zener velocity and $g_n$ is the coupling strength to the $n$-th bosonic mode with frequency $\omega_n$ and creation operator $\hat{a}_n^\dagger$. This is schematically displayed in Fig. 6.2(a). Generally, the Schrödinger equation of a time-dependent system is hard to solve, especially if $[\hat{H}(t), \hat{H}(t')] \neq 0$ for $t \neq t'$, as is the case for $\hat{H}_{\mathrm{LZ}}$ in Eq. 6.1. Nevertheless, a closed expression for the Landau-Zener tunneling probability $P_{\mathrm{LZ}}$ (probability to remain in the initial state) was found for a two-level crossing in the limit of $t \to \infty$, as $P_{\mathrm{LZ}} = \exp\left(-2\pi g^2/|v|\right)$ [Lan32; Zen32]. In several more recent works, this was expanded for an arbitrary number of crossings [Shy04; Wub+06; Sai+07]:

$$P_{\mathrm{LZ}} = \prod_n \exp\left(-\frac{2\pi}{|v|} g_n^2\right). \tag{6.2}$$

Each avoided crossing can be interpreted as a beamsplitter for incoming photons [Oli+05]. Therefore, multiple crossings consecutively reduce the probability of the excitation to remain in the initial mode, see Fig. 6.2(a). It is also intuitive that

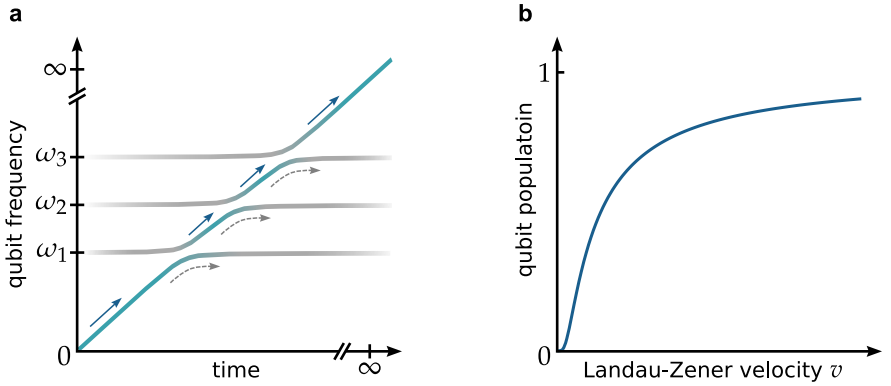


**Figure 6.2: Multistate Landau-Zener model.** (a) Sketch of the energy levels in the single-photon manifold of a qubit coupled to three bosonic modes. At resonance, a transverse coupling to the oscillators results in avoided crossings with the qubit. In the Landau-Zener Hamiltonian, each crossing acts as a beamsplitter for the photon stored in the qubit. (b) Qubit population at $t \to \infty$ as a function of the Landau-Zener velocity $v$, see Eq. (6.2). A fast transit of the bosonic modes results in a low probability to transfer the photon. In the opposing adiabatic limit of $v \to 0$, the qubit is depopulated with an efficiency approaching unity.

the probability to traverse the crossing without changing the initial state is lower for a larger level splitting $2g_n$ and a low Landau-Zener velocity, which corresponds to the adiabatic limit. On the other hand, large $v$ increase the probability to remain in the initial state, in accord with the sudden approximation [Sch07], see Fig. 6.2(b). In many systems, for example magnetic molecular clusters [WS99], the splitting $2g$ of two quantum states can be extracted experimentally by capitalizing on the strong dependence of $P_{\mathrm{LZ}}$ on the coupling strength. In a cQED setup, the Landau-Zener tunneling was utilized upon to realize fast and high-fidelity C-phase gates and Bell state preparation between two transmon qubits coupled via a three-stage microwave filter [McK+15].

Across the two branches of the beamsplitter given by a single avoided crossing of two states $|0\rangle$ and $|1\rangle$, a phase of

$$\Theta(t) = \int_{t_0}^{t} (\omega_0(t) - \omega_1(t))\,\mathrm{d}t \tag{6.3}$$

is gathered [Oli+05]. Here, $\omega_i$ is the eigenfrequency of state $i$ and $t_0$ marks the moment in time when the two levels cross. Therefore, repetitive transitions of the avoided crossing lead to an interference, similar to Mach-Zehnder interferometry. For example, in superconducting flux [Oli+05; Ber+08] and charge qubits [Sil+06], but also in semiconductor qubits [PLG10; OHM18] and nitrogen-vacancies in diamond [CM10; Fuc+11], this Landau-Zener-Stückelberg interferometry can be

exploited for fast quantum state preparation. The time dynamics of a single Landau-Zener transition has also found great interest in theoretical works [Vit99; ZHK08; OIL10; OIL13]. Experimentally, the coherent oscillations emerging during the transition of the avoided crossing have been studied to some extend at hand of Helium Rydberg atoms [YSK92], superconducting flux qubits [Ber+08], accelerated optical latices [Zen+09], and single electronic spins [Hua+11].

In this work, we employ a superconducting circuit to study the transient dynamics of the Landau-Zener model with multiple modes, each corresponding to an independent beamsplitter. As described in the following section, the underlying cQED architecture offers good control of both, Landau-Zener velocity $v$ (in situ control) and coupling coefficients $g_n$ (fixed by the circuit design).

## 6.3 The quantum simulation device

In this work, an analog quantum simulation of the multistate Landau-Zener model was performed. Due to their tailored functionality, flexibility, and good control of all circuit parameters, superconducting quantum devices are an ideal platform to implement the Hamiltonian of Eq. 6.1. The three main ingredients are an ensemble of bosonic modes, a tunable two-level system, which interacts via a transverse coupling with the ensemble, and a dedicated resonator for dispersive readout of the qubit state.

Figure 6.3 displays a micrograph of the simulation device. Here, a transmon qubit takes the role of the two-level system. The dispersive readout scheme is implemented with a capacitively coupled $\lambda/4$-resonator. Excess photon loss due to strong coupling to the readout resonator is mitigated with a Purcell-filter, see Sec. 4.3.4. The qubit's dc SQUID, and thereby its frequency, is tunable via magnetic flux induced by an on-chip flux bias line, see Sec. 4.4.4. A dedicated drive port, as described in Sec. 4.4.3, reduces crosstalk of the applied qubit gates with other circuit elements. From FEM simulations, we extract the coupling quality factor between drive port and qubit. This yields a contribution of $\Gamma_{\mathrm{P,d}} \approx 1/281\,\mu\mathrm{s}^{-1}$ to Purcell loss.

The bosonic modes in the model are emulated by, in this case five, lumped element oscillators. Choosing lumped element over distributed CPW resonators facilitates to engineer a dense and even spacing of their resonance frequencies, which is on the order of the coupling strength $g_n$ to the qubit. Direct characterization and state preparation of the bosonic modes is realized by a common transmission line. By

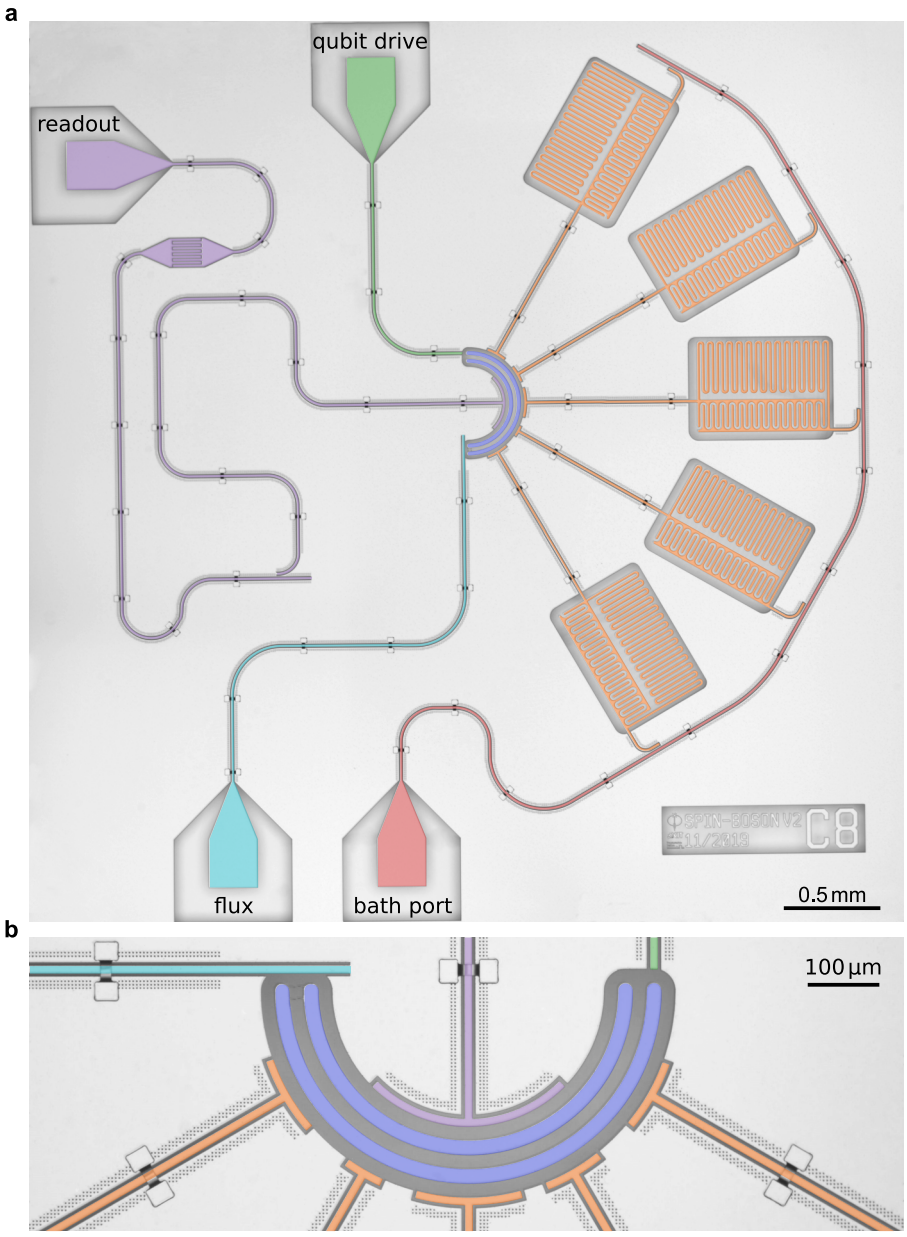


**Figure 6.3: Micrograph of the measurement device.** (a) Overview of the chip (stitched image). An ensemble of five lumped element resonators (orange) with a dedicated transmission line (red) is coupled capacitively to a transmon qubit (blue). Fast tunability is achieved with an impedance matched flux bias line (cyan) coupled to the SQUID of the qubit. Ac and dc flux bias are decoupled using a bias tee. Qubit gates are admitted to the qubit via a dedicated drive port (green). Purcell loss through the readout line (purple) is mitigated by a broadband Purcell filter. The qubit state is measured dispersively, using a $\lambda/4$-resonator. (b) Closeup of the qubit and its control lines.

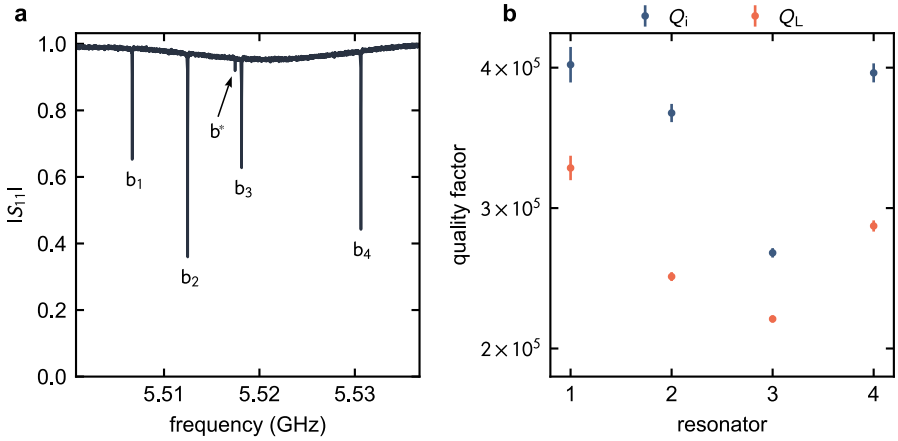


**Figure 6.4: Characterization of the bosonic mode ensemble.** (a) Amplitude signal of the reflection measurement. Two out of the five lumped element resonators seem to have hybridized, likely due to a fabrication error. This is indicated by the weak coupling of the $b^*$ mode to the waveguide. (b) Quality factors of the bosonic modes, excluding $b^*$.

choosing large coupling quality factors $Q_c$ additional Purcell-loss is kept at a minimum and unwanted resonator-resonator crosstalk is reduced. Nevertheless, a finite resonator-resonator interaction remains, especially due to the coupling capacitance to the qubit, which mediates the transverse coupling in the Landau-Zener model. By design, the $g_n$ increase with decreasing frequency of the corresponding bosonic mode. The amplitude signal of a reflection measurement on the bath-port, where the qubit is far detuned from the ensemble, is displayed in Fig. 6.4(a). Four of the five modes, labeled $b_1$-$b_4$, are clearly visible. Their parameters, extracted from a circle fit to the complex reflection signal [Pro+15], are shown in Fig. 6.4(b) and listed in table 6.1. The fifth mode, however, couples only weakly to the transmission line. It is conceivable that two of the microwave resonators are close in frequency space and have hybridized, owed to the indirect and weak but non-vanishing resonator-resonator coupling. Here, the $\sim 180^\circ$ phase-shifted dipole of the antisymmetric mode strongly suppresses the coupling quality factor. A small, but finite interaction with the transmission line is retained, due to the phase-difference between the resonators with respect to a photon traveling through the waveguide.

Obviously, this also affects the coupling to the qubit, since the antisymmetric mode barely interacts with the transmon. In a two-tone experiment, see Fig. 6.5(a), the transmon is tuned on resonance with the resonator ensemble, revealing the mode spectrum of the single-photon manifold of the underlying Jaynes-Cummings model.

**Table 6.1: Properties of the resonator ensemble.** These parameters are also employed throughout all numerical QuTiP simulations.

| resonator | $\omega_r/2\pi$ (GHz) | $Q_i$ $(\times 10^3)$ | $Q_L$ $(\times 10^3)$ | $g_n/2\pi$ (MHz) |
|---|---|---|---|---|
| $b_1$ | 5.507 | 402 | 329 | 14.6 |
| $b_2$ | 5.513 | 368 | 251 | 12.1 |
| $b_3$ | 5.518 | 268 | 221 | 14.4 |
| $b_4$ | 5.531 | 396 | 287 | 6.3 |

In a two-tone experiment, see Fig. 6.5(a), the dispersive shift of the readout resonator is monitored while a second microwave tone is admitted via the qubit drive port. When the transmon is tuned in and out of resonance with the resonator ensemble, the mode spectrum of the single-photon manifold of the underlying Jaynes-Cummings model is revealed by the dispersive shift of the readout resonator. The transverse interaction of bath and qubit results in four avoided level crossings. The coupling coefficients are extracted by a fit to the avoided crossing [Qki20] and are summarized in table 6.1. Since they are on the same order as the frequency spacing of the modes, the hybridized states are collective excitations of the qubit and/or several resonators. Naturally, the contribution of each mode depends on the qubit frequency. At certain frequencies the photonic excitation in the system is exclusively shared between the resonators while the qubit remains in the ground state. Therefore, the resulting dark states are no longer detectable by dispersive qubit state readout. Figure 6.5(b) displays a similar measurement, however, at a higher sample temperature. This is realized by removing (some of the) attenuators on the base stage. Higher transitions of the thermally excited system become visible. Additionally, the linewidth is generally larger, due to the increased relaxation rate.

From spectroscopic measurements we find the transmon qubit's flux sweet spot at $\omega_q^{\max}/2\pi = 10.56\,\text{GHz}$, see Fig. 3.6. A power scan reveals the two-photon transition from ground to second excited state and thereby yields a qubit anharmonicity of $\alpha/2\pi = -241\,\text{MHz}$, see Fig. 3.5. The working point of the qubit at $\sim 5.3\,\text{GHz}$, situated close to the bosonic bath, lies considerably lower in frequency than the sweet spot. The steep slope of the dispersion makes the qubit extremely susceptible to flux noise. Most likely, the flux noise is the limiting factor of our low qubit coherence time $T_2 \approx 0.2\,\mu\text{s}$, which is not limited by the energy relaxation time $T_1 \approx 6\,\mu\text{s}$. On the bright side, this is accompanied by a large qubit tunability, even for small bias currents. As described in Sec. 4.5.2, fast flux tunability is achieved with a bias tee, installed on the cryostat's base stage. At the working point, the qubit is rf tunable over a frequency range of $\sim$ 400 MHz. On the scale of the bath-qubit coupling strength, this is large enough to tune the qubit to the other

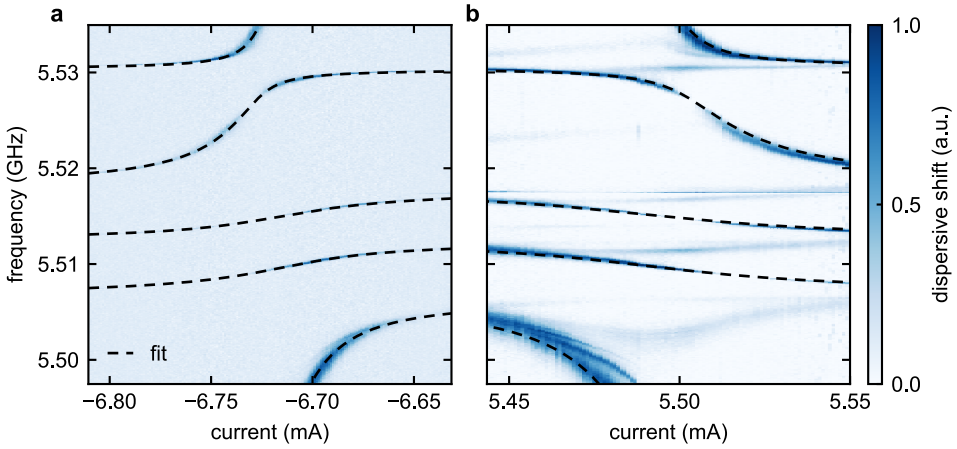


**Figure 6.5: Avoided level crossings of the qubit and resonator ensemble.** (a) Energy transitions in the single-photon manifold, measured with two-tone spectroscopy, as a function of the bias current at the flux coil. The coupling coefficients to the mode ensemble are extracted from a fit to the characteristic line shape of the avoided crossing (black dashed lines). At several points, some of the modes seem to disappear. In these dark states, the photonic excitation is exclusively shared between the resonators while the qubit remains unpopulated. Therefore, the state becomes "invisible" to the dispersive readout. (b) Measurement at an elevated temperature. The effective sample temperature is increased by removing attenuators on the base stage. Therefore, single-photon transitions of higher photon-manifolds become visible.

side of the resonator ensemble, i.e., at $\sim 5.7\,\mathrm{GHz}$, while retaining a small dressing at both minimum and maximum qubit frequency.

## 6.4 Swap spectroscopy of the bosonic mode ensemble

Another interesting experiment to characterize the bosonic bath, is a swap spectroscopy, oftentimes used to identify TLS in a qubit chip [Sha+10; MCL19]. Initially, the qubit with a frequency $\omega_\mathrm{i}$ is prepared in the excited state using a $\pi$-pulse. Thereafter, a fast $z$-pulse is employed to tune the qubit, more or less instantaneously, to a frequency $\omega$, where it can interact with its surroundings for a time $t$. Finally, the qubit is biased to a frequency $\omega_\mathrm{f}$ (which can be identical to $\omega_\mathrm{i}$) to halt the time evolution. Notably, the qubit Hamiltonian at $\omega_{\mathrm{i,f}}$ should feature a negligible coupling to the environment, to ensure that the qubit is initially prepared in the excited state (at $\omega_\mathrm{i}$) and stops to evolve (at $\omega_\mathrm{f}$).

In the Jaynes-Cummings model with a single resonator, this would lead to vacuum Rabi oscillations: Due to the similarity of the Jaynes-Cummings and the Rabi Hamiltonian in Eq. 3.11, coherent oscillations of the qubit population emerge. In contrast to the Rabi cycle displayed in Fig. 3.2, the qubit starts in the excited state[1] and the coupling strength $g$ between qubit and resonator takes the role of the drive strength $\Omega_0$.

This situation can change drastically when more than one bosonic mode is involved. Figure 6.6 displays numerical simulations of vacuum Rabi oscillations between an ideal two-level system and two bosonic modes. In our simulations, we find that the behavior of the system dramatically depends on the ratio $\xi = g/\Delta\omega_\mathrm{r}$ of mean coupling strength $g$ (here, equal for both resonators) to the frequency spacing $\Delta\omega_\mathrm{r}$ of the modes. For small $\xi$, there is practically no interplay of the two single-photon Fock-states the qubit couples to and the resonators can be distinguished clearly, see Fig. 6.6(a). For larger $\xi$ interference effects start to occur, most notable in the region around $\xi \approx 0.5$, where the two pattern start to merge. Initially, this gives the impression that the qubit "skips" a beat when tuned to $\omega_\mathrm{r}$, see Fig. 6.6(b). If the coupling strength is increased even further, the modes are almost indistinguishable by the qubit and the suppressed oscillation becomes brighter, see Fig. 6.6(c). Finally, for $\xi = 2$ most of the interference effects have receded, see Fig. 6.6(d). Here, the vacuum Rabi oscillations resemble those of a qubit coupled to a single bosonic mode with an enhanced coupling strength of $\sqrt{2}g$. This is the typical $\sqrt{n}$-enhancement, which is also observed in the Tavis-Cummings model [Aga84; Yan+20]. In its essence, the observed interference effects are similar to the collapse and revival dynamics in the Jaynes-Cummings model, where higher Fock states play the role of our circuit's multi-mode structure [Gea90]. In the simulations displayed in Fig. 6.6, the bosonic modes were truncated at the three-photon state to reduce the simulation time. Furthermore, energy relaxation and decoherence were neglected.

Figure 6.7(a) displays the swap spectroscopy measurement of the qubit with the resonator ensemble. In contrast to the preceding numerical analysis, four modes with a non-uniform frequency spacing interact with the qubit, each with a different coupling strength. While a quantitative interpretation becomes challenging, we are qualitatively in the regime of $\xi \gtrsim 1$. Here, the ensemble already starts to act more uniformly and strong interference effects are suppressed. Nevertheless, the interplay of multiple Fock states leads to intricate features such as bright and dark spots, and the coalescence of Rabi fringes. This is accompanied by a much higher effective coupling strength $g_\mathrm{eff}/2\pi \approx 25\,\mathrm{MHz}$. We find good agreement with a

[1] qubit population is the inverse of that in Eq. 3.15

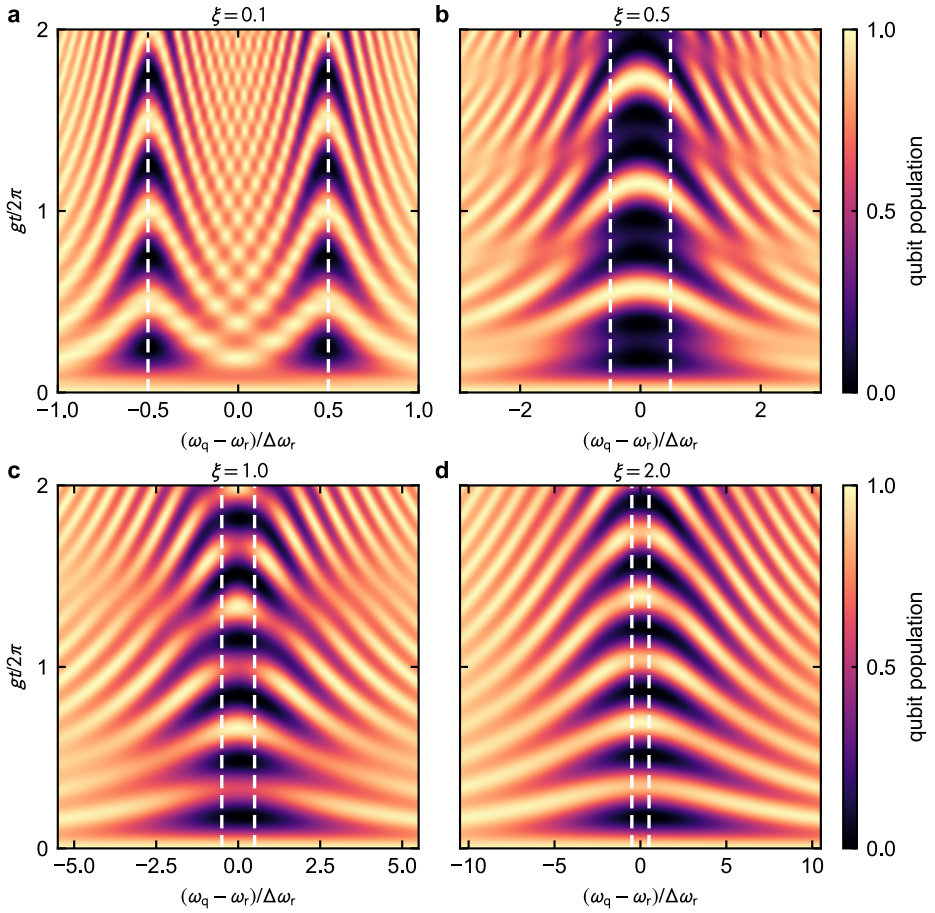


**Figure 6.6: Numerical simulations of vacuum Rabi oscillations with two bosonic modes.** The simulations show oscillations of the qubit population as a function of time and detuning from central frequency $\omega_r$ of the two resonators. The coupling strength $g$ to the qubit is equal for both modes. The time evolution critically depends on the ratio $\xi = g/\Delta\omega_r$, where $\Delta\omega_r$ is the spacing of the resonators. Their frequency is indicated by dashed white lines. (a) For $\xi = 0.1$, the interference pattern of the two modes can be distinguished clearly, each closely resembling that of vacuum Rabi oscillations with a single mode. (b) At $\xi = 0.5$, the two oscillation pattern have already started to merge. Here, interference effects are most prominent. (c) As the two modes close in on each other, these effects become more subtle, here shown for $\xi = 1$. (d) At $\xi = 2$, interference effects have receded almost completely. The observed vacuum Rabi oscillations closely resemble those of a qubit coupled to a single mode with an increased coupling strength $g_{\mathrm{eff}} = \sqrt{2}g$.

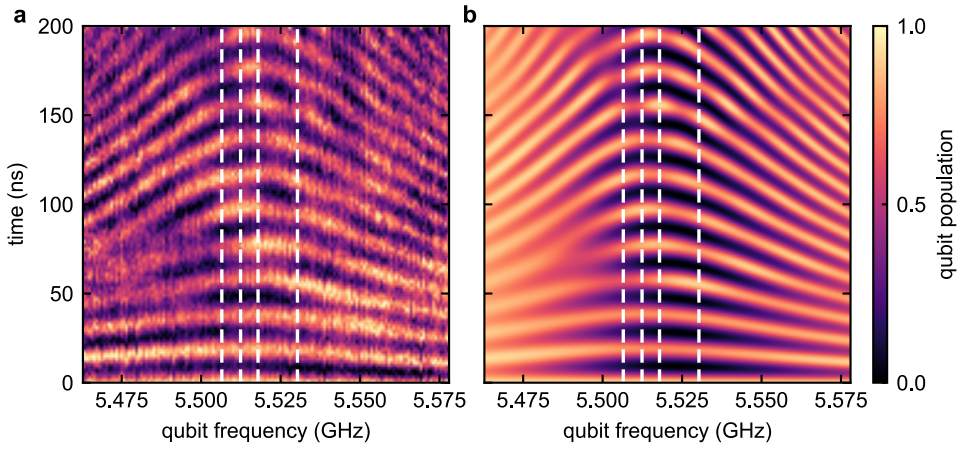


**Figure 6.7: Vacuum Rabi oscillations between the qubit and resonator ensemble.** (a) The qubit is prepared in the excited state and tuned in (or close to) resonance with the bosonic bath. It evolves freely until the evolution is stopped by biasing it to a different frequency, far away from the ensemble (relative to the $g_n$). For each resonator, a white dashed line indicates its bare transition frequency, listed in table 6.1. Interference of the qubit with multiple Fock states leads to several intricate features such as bright and dark spots, and the coalescence of Rabi fringes. (b) We verify our results by QuTiP simulations. Most of the features in the numerical results are also identified in the experiment. In the plot, both, measured and simulated qubit population were interpolated numerically.

numerical QuTiP simulation, see Fig. 6.7(b). This indicates a sufficient precision of our sample characterization, see Sec. 6.3, and emphasizes the accuracy of the employed model Hamiltonian.

## 6.5 Experimental simulation of the multistate Landau-Zener model

In this work, the Landau-Zener model is directly emulated by the hardware, thus no complex driving schemes are needed to run the simulation. The simulation scheme follows the simple algorithm of system state preparation, time evolution by tuning the qubit, and finally qubit state readout. Initially, the qubit resides roughly 200 MHz below the lowest resonator at $\omega_\mathrm{q} = \omega_\mathrm{i}$. Due to the large detuning from the transmon's flux sweet spot, a flux bias increasing linearly with time results in a linear increase of the qubit frequency. The final (i.e., maximum) frequency $\omega_\mathrm{f}$ of the qubit is determined by the experimental constraints imposed by the bias tee. The Landau-Zener velocity in Eq. 6.1 is given by $v = (\omega_\mathrm{f} - \omega_\mathrm{i})/t_\mathrm{rise}$, where

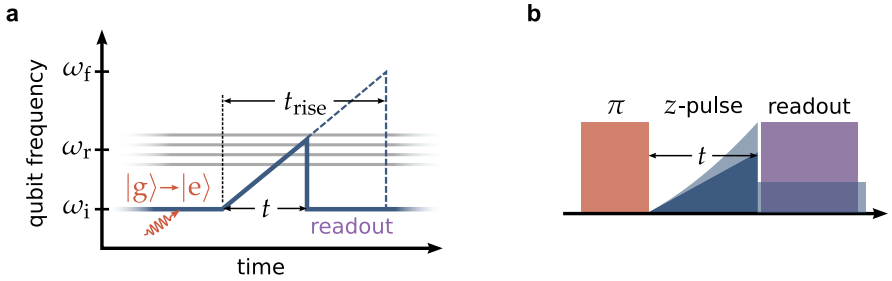


**Figure 6.8: Schematic diagram of the simulation protocol and pulse sequence.** (a) Protocol of the quantum simulation of the Landau-Zener model. Initially, the system is prepared in an arbitrary quantum state, for example, by applying a $\pi$-pulse (orange) to the qubit or by pumping the bath resonators. The qubit frequency (blue line) is increased linearly for a time $t$, before returning to $\omega_i$, where state readout is performed. The Landau-Zener velocity $v$ is determined by the time $t_{rise}$ needed to reach the maximum qubit frequency $\omega_f$. From repeated measurements for various values of $t$ (blue dashed line indicates $t = t_{rise}$), the time resolved qubit population along the Landau-Zener transition is inferred. (b) Pulse sequence of the experiment. The $z$-pulse tuning the qubit frequency (blue) is adjusted to account for the decay of the voltage across the bias tee (light blue), see Sec. 4.5.2. After the time $t$, the qubit is returned to $\omega_i$, where it remains until state readout (purple) is concluded.

$t_{rise}$ is the time needed to tune the qubit (linearly) from $\omega_i$ to $\omega_f$. We determine the qubit population at several time points along its trajectory. For state readout the qubit is returned to $\omega_i$, halting the time evolution. In the spirit of the sudden approximation [Sch07], Landau-Zener-Stückelberg interference should only have a minor impact on the results. Experimentally, the time resolution is limited to 1 ns by the ADC generating the tuning pulse. Figure 6.8 displays a schematic diagram of the simulation protocol and the necessary pulse sequence for emulating the Landau-Zener model with our device.

In this work, we looked at the Landau-Zener model from different perspectives. While we are restricted to measuring the qubit population only, we have several options regarding the initial state preparation of the system. For example, we can populate the qubit in the excited state and monitor its time evolution. Additionally, owing to the dedicated drive line of the resonator ensemble, we can also pump the resonators before the Landau-Zener transition. Furthermore, we have full control over the Landau-Zener velocity $v$ by altering $t_{rise}$.

### 6.5.1 Scattering an excited qubit

In the first Landau-Zener experiment presented in this chapter, we initialize the system in the first excited state, i.e., roughly the qubit's first excited state, by

applying a weak $\pi$-pulse ($\sim 140\,\mathrm{ns}$ length) to the qubit. This way, we ensure that the time evolution is dominated by the dynamics of the Landau-Zener model, rather than stemming from the preparation in a non-eigenstate. The experimental results of the quantum simulation are displayed in Fig. 6.9, in conjunction with numerical simulations of the system, in good agreement with the measurements. Here, we convert the simulation time $t$ to a frequency using $\omega_\mathrm{q} = \omega_\mathrm{i} + vt$. This enables a better comparability between traces with a different rise time $t_\mathrm{rise}$. In order to reduce the computational complexity in the numerical simulation, we truncate each resonator at the second Fock state (i.e., $n > 1$). Qualitatively and quantitatively the results should remain unaffected, since the experiment is also restricted to the single-photon manifold.

In the experiment, we observe coherent oscillations of the qubit's population, emerging after it has traversed the mode ensemble. In terms of the qubit frequency, the periodicity of the oscillations decreases for larger $t_\mathrm{rise}$, see Fig. 6.9(a, c). As expected from Eq. 6.3, the oscillation frequency increases with time $t$. Figure 6.9(b) comprises a quantitative comparison of quantum and numerical simulation for different rise times. We find a good agreement after accounting for a small offset of 5.2 ns to $t_\mathrm{rise}$ in the experiment, likely caused by a distortion of the tuning pulse after traversing the microwave lines to the sample. Particularly for large $t_\mathrm{rise}$, the decay of the coherent oscillations with time $t$, that is, increasing qubit frequency, becomes visible. Notably, this is not caused by the limited life-, and coherence times of our simulation device. Rather, the qubit population becomes increasingly static, approaching the Landau-Zener tunneling probability $P_\mathrm{LZ}$. The initial oscillation amplitude also decreases towards a smaller Landau-Zener velocity, corresponding to large $t_\mathrm{rise}$, as the transition becomes adiabatic.

The qubit population at the final frequency $\omega_\mathrm{f}$ is displayed in Fig. 6.9(d), where we compare it with the numerical simulation and the analytical formula for $P_\mathrm{LZ}$, see Eq. 6.2. Apart from the remnants of Stückelberg oscillations in the measurement, our data agrees well with the analytical formula. As predicted, the qubit remains in the excited state for $t_\mathrm{rise} = 0$ and exponentially approaches the ground state in the adiabatic limit of $t_\mathrm{rise} \to \infty$. For short rise times in the experiment ($t_\mathrm{rise,\,exp} \approx$ 5-10 ns), we observe an overshoot of the qubit population. Here, the the finite time response of fast flux lines, particularly the bias tee, likely results in a distortion of the $z$-pulses. Additionally, constructive Landau-Zener-Stückelberg interference, which is not accounted for by the classical simulation, could play a role.

The multistate character of the model is manifested mainly in the Landau-Zener tunneling probability $P_\mathrm{LZ}$, see Eq. 6.2. Effects to the transient dynamics, are more subtle and only play a quantitative role. In contrast to other experiments on the Jaynes-Cummings model with a static qubit frequency, the most relevant energy and

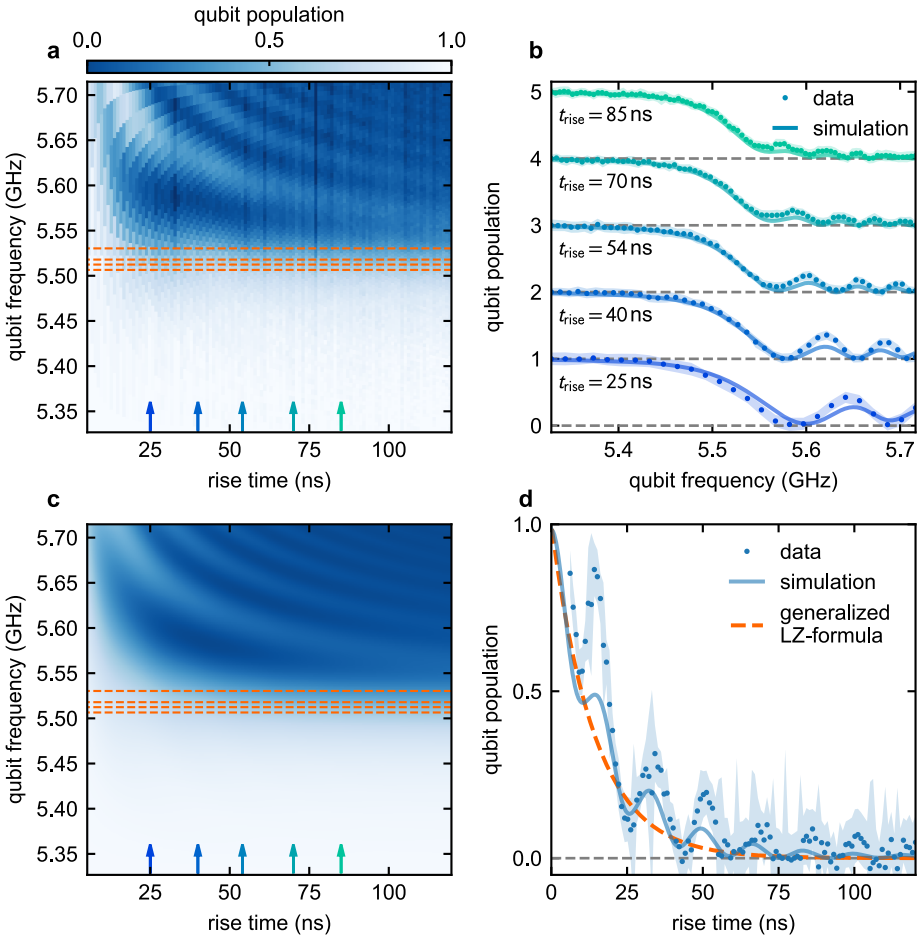


**Figure 6.9: Quantum simulation of the transient dynamics of the Landau-Zener model.** Quantum (a) and numerical simulation (c) of the qubit population during the transit of the bosonic mode ensemble, indicated by the dashed orange lines, as a function of the qubit frequency $\omega_q(t) = \omega_i + vt$ and rise time needed to reach the maximum qubit frequency. The initially constant qubit population undergoes a steep drop after traversing the mode ensemble, followed by the onset of coherent state oscillations. Their amplitude and periodicity diminish towards the final state frequency $\omega_f$. (b) Quantitative comparison of the experiment (dots) and numerical simulation (lines) for different rise times, indicated by blue arrows in (a, c). Within the uncertainty of the experimental data, indicated by the shaded areas, measurement and numerical simulation are in good agreement. Neighboring traces are shifted by 1 to improve visibility. (d) Qubit population at $\omega_f$ as a function of the rise time. While oscillations persist in measurement and simulation, the final qubit population is well approximated by the generalized Landau-Zener formula, see Eq. 6.2.

timescale is given by the Landau-Zener velocity $v$. The coupling strength $g$ mainly determines the amplitude of the coherent oscillations in the transient dynamics and $P_{\mathrm{LZ}}$. Compared to $v$, the mode ensemble has a high density, i.e. a low frequency spacing $\Delta\omega_{\mathrm{r}}$, acting more or less like a continuum or single mode. This leads to a $\sqrt{n}$-scaling of the effective coupling strength in the Landau-Zener tunneling probability, see Eq. 6.2. Qualitative features of the multistate character appear when the frequency[2] $v/\Delta\omega_{\mathrm{r}}$ approaches $\Delta\omega_{\mathrm{r}}$. In the current device, this cannot be observed: The large coupling coefficients $g_n$ result in a high photon transfer probability to the bosonic modes. Therefore, when increasing $v$ we reach the adiabatic limit before (qualitative) effects of the multistate system are observable.

### 6.5.2 Scattering on an excited bath

Additionally, our experimental setup allows for a preparation of the bosonic modes in an excited state. Since we cannot easily prepare the resonators in a Fock state, we admit a short drive pulse to one of the resonators, rather than the qubit. As discussed in the previous section, the coupling strength to the qubit determines the amplitude of the Landau-Zener tunneling. For a longer duration $t_{\mathrm{p}}$ of the initialization pulse, higher levels of the resonator are (partially) populated.[3] In the Jaynes-Cummings model, the coupling coefficient of the resonator prepared in an $n$-photon Fock state $|n\rangle$ to the qubit scales with $\sqrt{n}$, see Sec. 3.3.1. Consequently, the Landau-Zener tunneling probability increases for larger $t_{\mathrm{p}}$. This is most evident in Fig. 6.10(a), where we monitor the qubit population for a fixed $v$ ($t_{\mathrm{rise}} = 50\,\mathrm{ns}$) while increasing $t_{\mathrm{p}}$ of a pulse applied to resonator $\mathrm{b}_1$. Again, we observe coherent oscillations of the qubit population once it traverses the mode ensemble. Initially, the oscillation amplitude becomes more prominent for larger $t_{\mathrm{p}}$. For very long pump tones and, thereby, large coupling coefficients, the transition becomes adiabatic and the coherent oscillations are suppressed. Figure 6.10 displays the transients dynamics for an 80 ns (b) and 160 ns pump tone (c) applied to $\mathrm{b}_1$ as a function of the Landau-Zener velocity, which are qualitatively similar. Here, we refrain from a comparison with numerical simulations: The contribution of Fock states with $n > 1$ exponentially increases the Hilbert space and thereby the time of numerical calculations. The experiments indicate that the quantum simulation remains, for a low average photon number, qualitatively unimpaired by the population of higher levels of the bath resonators.

[2] $v$ has the unit of frequency per time, i.e., $1/\mathrm{s}^2$

[3] For $t_{\mathrm{p}} \gg 1/\Gamma_{\mathrm{r}}$, the resonator is prepared in a coherent state, where $\alpha$ depends on the power of the pulse.

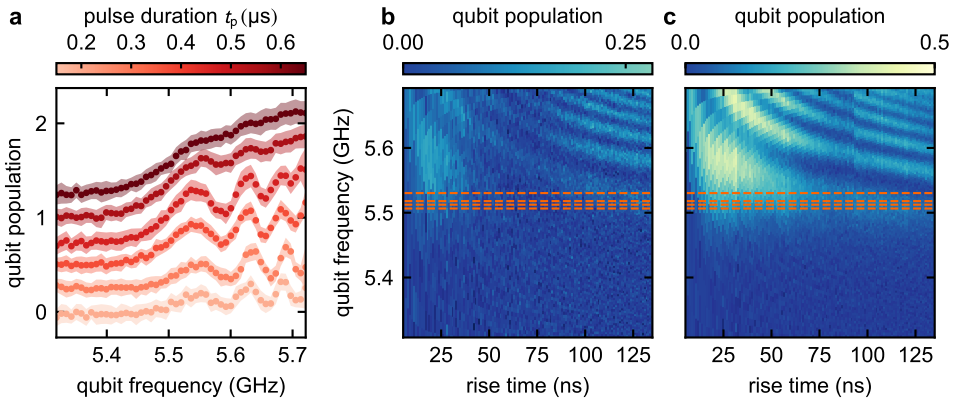


**Figure 6.10: Transient dynamics with an excited resonator mode: pump tone sweep.** (a) Transient dynamics for $t_{\mathrm{rise}} = 50\,\mathrm{ns}$ depending on the duration $t_{\mathrm{p}}$ of the drive applied to resonator $\mathrm{b}_1$. Starting at $t_{\mathrm{p}} = 150\,\mathrm{ns}$, the pulse length is increased in increments of 100 ns. For longer $t_{\mathrm{p}}$, higher Fock states with photon number $n$ are populated, which have a $\sqrt{n}$-enhanced coupling strength to the qubit. This results in a larger qubit population and more pronounced oscillations thereof. For very long $t_{\mathrm{p}}$, the transition becomes adiabatic and the oscillatory behavior is suppressed. Neighboring traces are shifted by 0.25 to improve visibility. (b,c) Transient dynamics as a function of the rise time for $t_{\mathrm{p}} = 80\,\mathrm{ns}$ (b) and $t_{\mathrm{p}} = 160\,\mathrm{ns}$ (c). The bath resonators are indicated by dashed orange lines.

Figure 6.11 displays the experimental quantum (a-d) and classical QuTiP simulations (e-h) of the transient time dynamics, depending on which bath mode is excited. Here, we employed a resonator drive with a fixed tone length of $t_{\mathrm{p}} = 80\,\mathrm{ns}$. In the QuTiP simulations, we initialize the corresponding resonator in a one-photon Fock state and restrict all bosonic modes to two energy levels, once again, to reduces the computation time. In agreement with the argument above, we find good qualitative agreement with the experiment. Similar to the results discussed in the previous section, we observe coherent oscillations of the qubit population after it traverses the bath. The "center of mass" with respect to $t_{\mathrm{rise}}$ and amplitude of these oscillations increases with the resonator frequency. This is captured best in the picture of multiple consecutive beamsplitters: The qubit population, depends on the reflected amplitude $P_i = \exp(2\pi g_i^2/|v|)$ of the first beamsplitter, i.e., the Landau-Zener tunneling probability of the $i$-th resonator, where the photon is initially injected. Obviously, a larger $P_i$ increases the expected qubit population. However, each consecutive beamsplitter reduces the qubit photon number, regulated by the transmission amplitude $1 - P_j$, where $P_j$ is the tunneling probability of the $j$-th resonator. Therefore, the maximal qubit population depends on the number of beamsplitters after the incipient photon injection and of course all tunneling probabilities. The comparatively low transfer probability when pumping $\mathrm{b}_4$ is owed to the significantly lower coupling strength to the qubit.

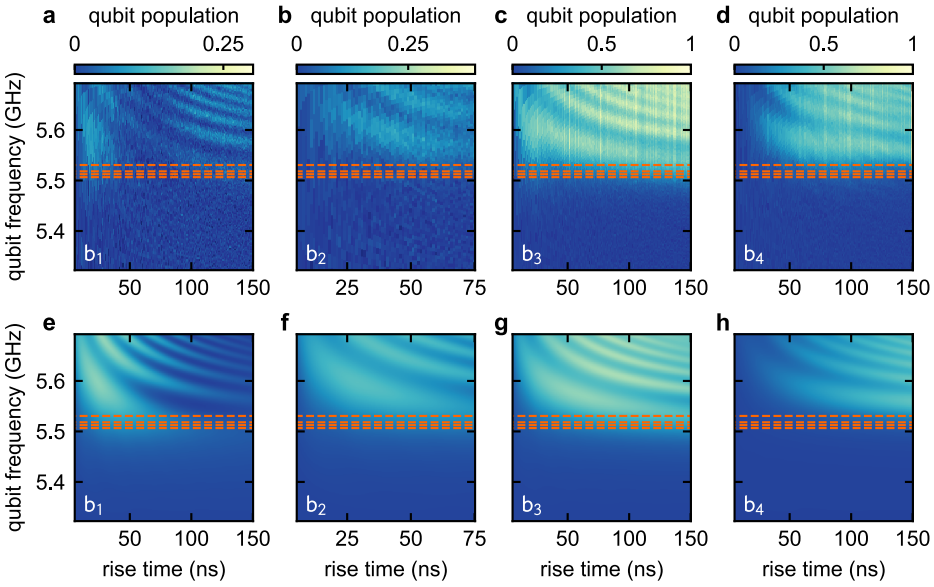


**Figure 6.11: Transient dynamics with an excited resonator mode for different initial states.** Each row of the panel corresponds to a different initial state. Dashed orange lines indicate the frequencies of the resonators constituting the mode ensemble. (a-d) In the experiment, the qubit starts in the ground state and traverses the bosonic modes, one of which is pumped with an 80 ns pulse. From (a)-(d), the resonators are excited in ascending order, starting with $b_1$. (e-f) QuTiP simulation of the time evolution (compare a to e, etc.). Computational time is reduced by initializing the bosonic mode in a one-photon Fock state and by limiting the Hilbert space to two states for each resonator. The color bar is shared between experiment and simulation. The amplitude of the emerging coherent oscillations of the qubit population strongly depend on the initially excited resonator.

In the adiabatic limit, the Landau-Zener tunneling can be used to exchange single photons between neighboring resonators. The diabatic limit allows for the preparation of entangled states between the mode ensemble and qubit.

## 6.6 Conclusion

In this chapter, I gave a short introduction to analog quantum simulation and its application to open quantum systems. The large Hilbert space provided by multiple bosonic modes is challenging problem to simulate with classical computers. Subsequently, I introduced one such system: the multistate Landau-Zener model. It describes several natural phenomena, such as molecular collision and chemical

reaction dynamics, and has recently seen a renewed interest, due to is application in cQED and the underlying Jaynes-Cummings model.

I presented our implementation of a quantum simulator of the multistate Landau-Zener model based on a superconducting quantum circuit. Using this device, we studied vacuum-Rabi oscillations of the multistate system. We performed an analog quantum simulation of the multistate Landau-Zener model, where we observed the transient dynamics in the vicinity of the bosonic mode ensemble depending on the system's initial state. Our experimental quantum simulations are in good agreement with numerical QuTiP simulations. In contrast to previous studies on the topic, the hallmark of our experiments is the multistate character of the Landau-Zener model and the exploration of the transient dynamics for different initial states of the system.

# 7 Conclusion and outlook

The goal of this thesis was to build an analog quantum simulator, comprising a superconducting qubit coupled to several bosonic modes and employ it to emulate the multistate Landau-Zener model. For this purpose, we established a scalable and flexible fabrication platform for nanoscaled and coherent Josephson junctions applicable to superconducting qubits.

At the beginning of this work, a subtractive junction fabrication process was developed [Ste+20]. This technology relies solely on etching the deposited metal films in order to structure the nanoscaled electrodes of the Josephson junction, see Fig. 7.1(a). In contrast to the common shadow evaporation techniques, the presented method is angle-independent and thus more scalable. The key feature of our process is the elimination of polymer resist and hard masks from the evaporation chamber. As a consequence, the superconductor-insulator-superconductor interfaces of the contacts are free of residues. This leads to a low aging of the junctions critical current, which we confirmed experimentally by comparing the normal state resistance of test contacts and the frequency of several qubits before and after $\sim$ 6 months of aging in ambient conditions, see Fig. 7.1(b). This long-term stability of the circuit parameters is certainly advantageous, especially for devices with a large number of Josephson junctions. Furthermore, we fabricated four transmon qubits using our subtractive processing platform and systematically characterized their energy loss rates and coherence properties. Albeit, there is room for improvement, the observed life-, and coherence times are competitive with those of qubits fabricated from existing technologies. Particularly, the energy loss and coherence times of our best device on average exceed 20 µs, see Fig. 7.1(c).

In conclusion, we established a scalable process for Josephson junction fabrication, compatible with standardized nanofabrication methods, and confirmed its ability to produce coherence qubits.

In the future, we expect that our processing platform constitutes a crucial ingredient for the streamlined, large-scale fabrication of superconducting quantum circuits. The elimination of resist and angle-dependence enables the investigation of different materials and growth modes for Josephson junctions. Furthermore, deposition at elevated temperature and in reactive gases becomes possible. This

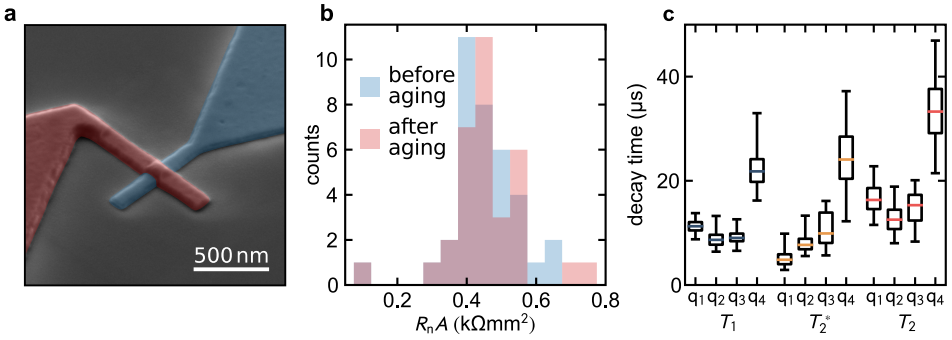


**Figure 7.1: Coherent superconducting qubits from a subtractive junction fabrication process [Ste+20].** (a) SEM micrograph of a Josephson contact fabricated with the subtractive process developed in this work. (b) The low aging of the junctions normal state resistances indicates clean superconductor-insulator-superconductor interfaces and results in a long-term stability of the circuit parameters. (c) Qubits fabricated from our process feature high lifetimes and good coherence properties.

opens a broad field of material research for qubit junctions, which may further advance the coherence properties of tomorrow's superconducting qubits. Additionally, our method is also applicable to all other areas of research where Josephson junctions are employed.

Using our junction fabrication technology, we built an analog quantum simulator of the multistate Landau-Zener model. This model describes the scattering processes of several interacting quantum states. Especially, it is employed to model chemical reaction dynamics [Nit06] and molecular collisions [Chi96]. Moreover, due to its generality, it finds application in any system with interacting quantum states and intersecting energy levels.

The simulation device, see Fig. 7.2(a), features a transmon qubit coupled to five bosonic modes, four of which couple to the qubit. We observed vacuum Rabi oscillations of the multi-mode system, which reveal the intricate dynamics of de- and re-phasing of multiple Fock-states. Furthermore, we employed our device to emulate the multistate Landau-Zener model. In particular, we studied the transient dynamics of the system, when the qubit is in the vicinity of the bosonic mode ensemble. The determining factor for the system's time evolution is the Landau-Zener velocity, which is equivalent to the time derivative of the qubit frequency. Experimentally, we can control this parameter, via the external flux applied to the qubit's SQUID. We studied the time evolution for different initial states of the system. Here, the circuit design enables the excited state preparation of the qubit or the bosonic modes. We observed coherent oscillations of the qubit population as a function of time, see Fig. 7.2(b). Both, amplitude and frequency of these oscillations

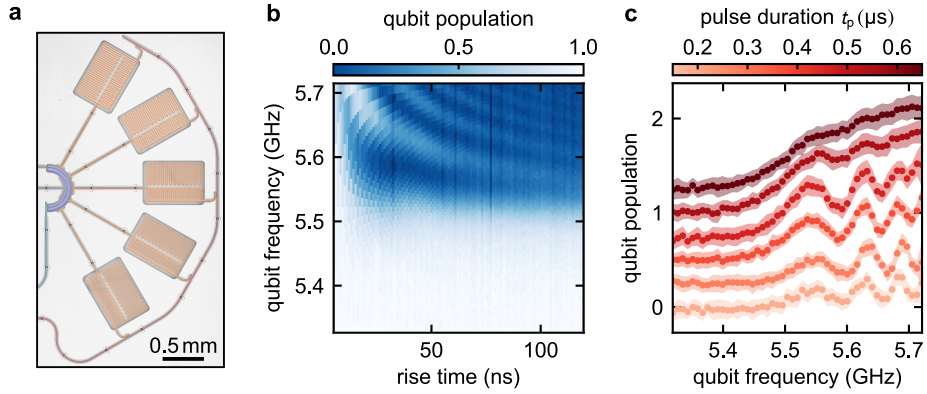


**Figure 7.2: Analog quantum simulation of the multistate Landau-Zener model.** (a) Optical micrograph of the simulation device. The transmon qubit is coupled capacitively to the microwave oscillators, emulating the bosonic modes in the model. (b) Transient dynamics of the system, where the qubit was initially prepared in the excited state. The qubit population evolution depends on the Landau-Zener velocity, which is anti-proportional to the rise time. (c) Time evolution of the qubit, depending on time $t_p$ of a drive tone applied to the lowest frequency bosonic mode. The behavior transitions to an adiabatic transit without coherent oscillations for large $t_p$.

are mainly determined by the Landau-Zener velocity. Numerical QuTiP simulations are in good qualitative agreement with our experimental quantum simulation.

When the qubit is initially prepared in the excited state, we also found good quantitative agreement of the quantum and classical simulation. We verified the accuracy of our quantum simulation by comparing the experimental data with the well-known analytical results valid in the limit of $t \to \infty$.

Additionally, we studied the behavior of the system depending on the average number of photons in an initially excited bosonic mode. Here, we observed the transition from a coherent to an adiabatic transit of the qubit-resonator avoided crossing, see Fig. 7.2(c). We identified the $\sqrt{n}$-enhancement of the coupling strength between qubit and bosonic mode as the source of this effect, where $n$ is the number of photons in the resonator.

In conclusion, we successfully built an analog quantum simulator of the multistate Landau-Zener model. In contrast to previous studies on the topic, the hallmark of our experiments is the multi-mode character, which is visible both qualitatively and quantitatively, particularly in the exploration of the transient dynamics for different initial states.

In upcoming experiments, our simulation device can be used to study several other exciting aspects of the Landau-Zener model. This includes the time evolution at elevated temperatures or for a non-linear Landau-Zener velocity. Furthermore,

diabatic transitions can be employed to prepare entangled states between the qubit and resonators or just among several resonators. In the adiabatic limit, multiple transitions of the bath could be used to exchange a single photon between neighboring resonators, which may be interesting in the context of quantum memories [Nee+08; Rea+16; Kra+19].

Due to the flexibility of the simulation device, it can also be employed to emulate the multi-mode quantum Rabi model. This becomes particularly interesting in the ultra-strong coupling regime, which can be emulated simply by adding several microwave drive tones to the simulation scheme [Bal+12; Bra+17; Lep+18]. Our experimental demonstration of a densely-packed resonator ensemble paves the way for building devices featuring dozens of oscillators forming a well-controlled mode continuum. The resulting spin boson Hamiltonian is the go-to model when describing decoherence in quantum systems [Leg+87; SMS02] and maps onto a multitude of fascinating problems, such as the Kondo-effect [Leg+87; Le 12; Gol+13]. Furthermore, it is hard to simulate for classical computers, especially in the ultra-strong coupling regime [Pue+19]. Therefore, this work marks an important step towards future experiments on more complex systems with a definitive quantum advantage over classical devices.

# Bibliography


[Aga84] G. S. Agarwal: *Vacuum-Field Rabi Splittings in Microwave Absorption by Rydberg Atoms in a Cavity*. Physical Review Letters **53**.18 (1984), pp. 1732–1734. DOI: 10.1103/PhysRevLett.53.1732 (cit. on p. 80).

[AB63] V. Ambegaokar and A. Baratoff: *Tunneling Between Superconductors*. Physical Review Letters **11**.2 (1963), pp. 104–104. DOI: 10.1103/PhysRevLett.11.104 (cit. on p. 7).

[Aru+19] F. Arute, K. Arya, R. Babbush, D. Bacon, J. C. Bardin, R. Barends, R. Biswas, S. Boixo, F. G. Brandao, D. A. Buell, B. Burkett, Y. Chen, Z. Chen, B. Chiaro, R. Collins, W. Courtney, A. Dunsworth, E. Farhi, B. Foxen, A. Fowler, C. Gidney, M. Giustina, R. Graff, K. Guerin, S. Habegger, M. P. Harrigan, M. J. Hartmann, A. Ho, M. Hoffmann, T. Huang, T. S. Humble, S. V. Isakov, E. Jeffrey, Z. Jiang, D. Kafri, K. Kechedzhi, J. Kelly, P. V. Klimov, S. Knysh, A. Korotkov, F. Kostritsa, D. Landhuis, M. Lindmark, E. Lucero, D. Lyakh, S. Mandrà, J. R. McClean, M. McEwen, A. Megrant, X. Mi, K. Michielsen, M. Mohseni, J. Mutus, O. Naaman, M. Neeley, C. Neill, M. Y. Niu, E. Ostby, A. Petukhov, J. C. Platt, C. Quintana, E. G. Rieffel, P. Roushan, N. C. Rubin, D. Sank, K. J. Satzinger, V. Smelyanskiy, K. J. Sung, M. D. Trevithick, A. Vainsencher, B. Villalonga, T. White, Z. J. Yao, P. Yeh, A. Zalcman, H. Neven, and J. M. Martinis: *Quantum supremacy using a programmable superconducting processor*. Nature **574**.7779 (2019), pp. 505–510. DOI: 10.1038/s41586-019-1666-5 (cit. on pp. 2, 13).

[Asp+05] A. Aspuru-Guzik, A. D. Dutoi, P. J. Love, and M. Head-Gordon: *Simulated Quantum Computation of Molecular Energies*. Science **309**.5741 (2005), pp. 1704–1707. DOI: 10.1126/science.1113479 (cit. on pp. 3, 13).

[Aum20] J. Aumentado: *Superconducting Parametric Amplifiers: The State of the Art in Josephson Parametric Amplifiers*. IEEE Microwave Magazine **21**.8 (2020), pp. 45–59. DOI: 10.1109/MMM.2020.2993476 (cit. on p. 24).

[Bak08] V. Bakshi: *EUV Lithography*. Ed. by V. Bakshi. SPIE, 2008. DOI: 10.1117/3.769214 (cit. on p. 63).

[Bal+12] D. Ballester, G. Romero, J. J. García-Ripoll, F. Deppe, and E. Solano: *Quantum simulation of the ultrastrong-coupling dynamics in circuit quantum electrodynamics*. Physical Review X **2**.2 (2012), pp. 1–6. DOI: 10.1103/PhysRevX.2.021007 (cit. on p. 94).

[Bal+19] E. Ballico, A. Bernardi, I. Carusotto, S. Mazzucchi, and V. Moretti, eds.: *Quantum Physics and Geometry*. Vol. 25. Lecture Notes of the Unione Matematica Italiana. Cham: Springer International Publishing, 2019. DOI: 10.1007/978-3-030-06122-7 (cit. on p. 20).

[BCS57] J. Bardeen, L. N. Cooper, and J. R. Schrieffer: *Theory of Superconductivity*. Physical Review **108**.5 (1957), pp. 1175–1204. DOI: 10.1103/PhysRev.108.1175 (cit. on pp. 5, 6).

[Bar+13] R. Barends, J. Kelly, A. Megrant, D. Sank, E. Jeffrey, Y. Chen, Y. Yin, B. Chiaro, J. Mutus, C. Neill, P. O'Malley, P. Roushan, J. Wenner, T. C. White, A. N. Cleland, and J. M. Martinis: *Coherent josephson qubit suitable for scalable quantum integrated circuits*. Physical Review Letters **111**.8 (2013), pp. 1–5. DOI: 10.1103/PhysRevLett.111.080502 (cit. on pp. 27, 44, 55).

[Ber+17] H. Bernien, S. Schwartz, A. Keesling, H. Levine, A. Omran, H. Pichler, S. Choi, A. S. Zibrov, M. Endres, M. Greiner, V. Vuletić, and M. D. Lukin: *Probing many-body dynamics on a 51-atom quantum simulator*. Nature **551**.7682 (2017), pp. 579–584. DOI: 10.1038/nature24622 (cit. on pp. 3, 71).

[Ber+08] D. M. Berns, M. S. Rudner, S. O. Valenzuela, K. K. Berggren, W. D. Oliver, L. S. Levitov, and T. P. Orlando: *Amplitude spectroscopy of a solid-state artificial atom*. Nature **455**.7209 (2008), pp. 51–57. DOI: 10.1038/nature07262 (cit. on pp. 3, 4, 74, 75).

[Bil+20] A. Bilmes, A. Megrant, P. Klimov, G. Weiss, J. M. Martinis, A. V. Ustinov, and J. Lisenfeld: *Resolving the positions of defects in superconducting quantum bits*. Scientific Reports **10**.1 (2020), p. 3090. DOI: 10.1038/s41598-020-59749-y (cit. on p. 23).

[Bla+04] A. Blais, R. S. Huang, A. Wallraff, S. M. Girvin, and R. J. Schoelkopf: *Cavity quantum electrodynamics for superconducting electrical circuits: An architecture for quantum computation*. Physical Review A **69**.6 (2004), p. 62320. DOI: 10.1103/PhysRevA.69.062320 (cit. on pp. 23–25, 27, 73).

[Blo08] I. Bloch: *Quantum coherence and entanglement with ultracold atoms in optical lattices*. Nature **453**.7198 (2008), pp. 1016–1022. DOI: 10.1038/nature07126 (cit. on p. 1).

[Boi+18] S. Boixo, S. V. Isakov, V. N. Smelyanskiy, R. Babbush, N. Ding, Z. Jiang, M. J. Bremner, J. M. Martinis, and H. Neven: *Characterizing quantum supremacy in near-term devices*. Nature Physics **14**.6 (2018), pp. 595–600. DOI: 10.1038/s41567-018-0124-x (cit. on p. 1).

[Bra17] J. Braumüller: *Quantum simulation experiments with superconducting circuits*. PhD thesis. Karlsruhe Institute of Technology, 2017, p. 149. DOI: 10.5445/IR/1000080698 (cit. on p. 41).

[Bra+15] J. Braumüller, J. Cramer, S. Schlör, H. Rotzinger, L. Radtke, A. Lukashenko, P. Yang, S. T. Skacel, S. Probst, M. Marthaler, L. Guo, A. V. Ustinov, and M. Weides: *Multiphoton dressing of an anharmonic superconducting many-level quantum circuit*. Physical Review B **91**.5 (2015), p. 54523. DOI: 10.1103/PhysRevB.91.054523 (cit. on p. 61).

[Bra+20] J. Braumüller, L. Ding, A. P. Vepsäläinen, Y. Sung, M. Kjaergaard, T. Menke, R. Winik, D. Kim, B. M. Niedzielski, A. Melville, J. L. Yoder, C. F. Hirjibehedin, T. P. Orlando, S. Gustavsson, and W. D. Oliver: *Characterizing and Optimizing Qubit Coherence Based on SQUID Geometry*. Physical Review Applied **13**.5 (2020), p. 054079. DOI: 10.1103/PhysRevApplied.13.054079 (cit. on p. 23).

[Bra+17] J. Braumüller, M. Marthaler, A. Schneider, A. Stehli, H. Rotzinger, M. Weides, and A. V. Ustinov: *Analog quantum simulation of the Rabi model in the ultra-strong coupling regime*. Nature Communications **8**.1 (2017), p. 779. DOI: 10.1038/s41467-017-00894-w (cit. on pp. 13, 24, 94).

[Bra+16] J. Braumüller, M. Sandberg, M. R. Vissers, A. Schneider, S. Schlör, L. Grünhaupt, H. Rotzinger, M. Marthaler, A. Lukashenko, A. Dieter, A. V. Ustinov, M. Weides, and D. P. Pappas: *Concentric transmon qubit featuring fast tunability and an anisotropic magnetic dipole moment*. Applied Physics Letters **108**.3 (2016). DOI: 10.1063/1.4940230 (cit. on pp. 53, 65).

[Bre+17] J. D. Brehm, A. Bilmes, G. Weiss, A. V. Ustinov, and J. Lisenfeld: *Transmission-line resonators for the study of individual two-level tunneling systems*. Applied Physics Letters **111**.11 (2017), p. 112601. DOI: 10.1063/1.5001920 (cit. on p. 59).

[Bre+21] J. D. Brehm, A. N. Poddubny, A. Stehli, T. Wolz, H. Rotzinger, and A. V. Ustinov: *Waveguide bandgap engineering with an array of superconducting qubits*. npj Quantum Materials **6**.1 (2021), p. 10. DOI: 10.1038/s41535-021-00310-z (cit. on p. 13).

[BKP13] P. Brooks, A. Kitaev, and J. Preskill: *Protected gates for superconducting qubits*. Physical Review A **87**.5 (2013), p. 052306. DOI: 10.1103/PhysRevA.87.052306 (cit. on p. 44).

[BK12] W. Buckel and R. Kleiner: *Supraleitung*. Weinheim, Germany: Wiley-VCH Verlag GmbH & Co. KGaA, 2012, pp. 296–296. DOI: 10.1002/9783527668670 (cit. on pp. 5–7).

[Bur+19] J. J. Burnett, A. Bengtsson, M. Scigliuzzo, D. Niepce, M. Kudra, P. Delsing, and J. Bylander: *Decoherence benchmarking of superconducting qubits*. npj Quantum Information **5**.1 (2019), p. 54. DOI: 10.1038/s41534-019-0168-5 (cit. on pp. 23, 65, 68).

[Cao+19] Y. Cao, J. Romero, J. P. Olson, M. Degroote, P. D. Johnson, M. Kieferová, I. D. Kivlichan, T. Menke, B. Peropadre, N. P. D. Sawaya, S. Sim, L. Veis, and A. Aspuru-Guzik: *Quantum Chemistry in the Age of Quantum Computing*. Chemical Reviews **119**.19 (2019), pp. 10856–10915. DOI: 10.1021/acs.chemrev.8b00803 (cit. on pp. 3, 13).

[Cat+11] G. Catelani, J. Koch, L. Frunzio, R. J. Schoelkopf, M. H. Devoret, and L. I. Glazman: *Quasiparticle Relaxation of Superconducting Qubits in the Presence of Flux*. Physical Review Letters **106**.7 (2011), p. 077002. DOI: 10.1103/PhysRevLett.106.077002 (cit. on p. 23).

[Cat+12] G. Catelani, S. E. Nigg, S. M. Girvin, R. J. Schoelkopf, and L. I. Glazman: *Decoherence of superconducting qubits caused by quasiparticle tunneling*. Physical Review B **86**.18 (2012), pp. 1–17. DOI: 10.1103/PhysRevB.86.184514 (cit. on p. 23).

[Che] Chemandy: *Coplanar Waveguide With Ground Characteristic Impedance Calculator*. URL: https://chemandy.com/calculators/coplanar-waveguide-with-ground-calculator.htm (visited on 12/07/2020) (cit. on p. 36).

[Che+14] Z. Chen, A. Megrant, J. Kelly, R. Barends, J. Bochmann, Y. Chen, B. Chiaro, A. Dunsworth, E. Jeffrey, J. Mutus, P. O'Malley, C. Neill, P. Roushan, D. Sank, A. Vainsencher, J. Wenner, T. C. White, A. N. Cleland, and J. M. Martinis: *Fabrication and Characterization of Aluminum Airbridges for Superconducting Qubit Circuits*. Bulletin of the American Physical Society **59**.1 (2014), p. M36.12. DOI: 10.1063/1.4863745 (cit. on pp. 55, 58).

[Chi96] M. S. Child: *Molecular collision theory*. Courier Corporation, 1996 (cit. on pp. 3, 73, 92).

[CM10] L. Childress and J. McIntyre: *Multifrequency spin resonance in diamond*. Physical Review A **82**.3 (2010), p. 033839. DOI: 10.1103/PhysRevA.82.033839 (cit. on pp. 3, 74).

[CZ95] J. I. Cirac and P. Zoller: *Quantum Computations with Cold Trapped Ions*. Physical Review Letters **74**.20 (1995), pp. 4091–4094. DOI: 10.1103/PhysRevLett.74.4091 (cit. on pp. 1, 13).

[Col+01] B. E. Cole, J. B. Williams, B. T. King, M. S. Sherwin, and C. R. Stanley: *Coherent manipulation of semiconductor quantum bits with terahertz radiation*. Nature **410**.6824 (2001), pp. 60–63. DOI: 10.1038/35065032 (cit. on p. 13).

[Cor20] R. Corporation: *TMM® 10 Laminates*. (2020). URL: https://www.rogerscorp.com/Advanced-Connectivity-Solutions/TMM-Laminates/TMM-10-Laminates (visited on 10/12/2020) (cit. on p. 49).

[CM89] R. I. Cukier and M. Morillo: *Solvent effects on proton-transfer reactions*. The Journal of Chemical Physics **91**.2 (1989), pp. 857–863. DOI: 10.1063/1.457137 (cit. on p. 73).

[Dev97] M. H. Devoret: "Quantum Fluctuations in Electrical Circuits". *Quantum Fluctuations*. Saclay, 1997, pp. 351–386 (cit. on pp. 7, 8, 45).

[Di 11] E. Di Lorenzo: *The Maxwell Capacitance Matrix*. Matrix March (2011), pp. 1–3. URL: https://www.fastfieldsolvers.com/Papers/The%7B%5C_%7DMaxwell%7B%5C_%7DCapacitance%7B%5C_%7DMatrix%7B%5C_%7DWP110301%7B%5C_%7DR02.pdf (cit. on p. 45).

[Dol77] G. J. Dolan: *Offset masks for lift-off photoprocessing*. Applied Physics Letters **31**.5 (1977), pp. 337–339. DOI: 10.1063/1.89690 (cit. on pp. 2, 60).

[Dol+03] R. Dolata, H. Scherer, A. B. Zorin, and J. Niemeyer: *Single electron transistors with Nb/AlO$_x$/Nb junctions*. Journal of Vacuum Science & Technology B: Microelectronics and Nanometer Structures **21**.2 (2003), p. 775. DOI: 10.1116/1.1560213 (cit. on p. 61).

[Dun+17] A. Dunsworth, A. Megrant, C. Quintana, Z. Chen, R. Barends, B. Burkett, B. Foxen, Y. Chen, B. Chiaro, A. Fowler, R. Graff, E. Jeffrey, J. Kelly, E. Lucero, J. Y. Mutus, M. Neeley, C. Neill, P. Roushan, D. Sank, A. Vainsencher, J. Wenner, T. C. White, and J. M. Martinis: *Characterization and reduction of capacitive loss induced by sub-micron Josephson junction fabrication in superconducting qubits*. Applied Physics Letters **111**.2 (2017), p. 022601. DOI: 10.1063/1.4993577 (cit. on pp. 23, 62, 68).

[EH05] C. Enss and S. Hunklinger: *Low-Temperature Physics*. Berlin/Heidelberg: Springer-Verlag, 2005. DOI: 10.1007/b137878 (cit. on p. 11).

[EDM86] D. Esteve, M. H. Devoret, and J. M. Martinis: *Effect of an arbitrary dissipative circuit on the quantum energy levels and tunneling of a Josephson junction*. Physical Review B **34**.1 (1986), pp. 158–163. DOI: 10.1103/PhysRevB.34.158 (cit. on p. 23).

[Fag06] R. L. Fagaly: *Superconducting quantum interference device instruments and applications*. Review of Scientific Instruments **77**.10 (2006), p. 101101. DOI: 10.1063/1.2354545 (cit. on p. 5).

[Fey82] R. P. Feynman: *Simulating physics with computers*. International Journal of Theoretical Physics **21**.6-7 (1982), pp. 467–488. DOI: 10.1007/BF02650179 (cit. on p. 1).

[For+19a] P. Forn-Díaz, L. Lamata, E. Rico, J. Kono, and E. Solano: *Ultrastrong coupling regimes of light-matter interaction*. Reviews of Modern Physics **91**.2 (2019), p. 025005. DOI: 10.1103/RevModPhys.91.025005 (cit. on p. 73).

[For+19b] N. Foroozani, C. Hobbs, C. C. Hung, S. Olson, D. Ashworth, E. Holland, M. Malloy, P. Kearney, B. O'Brien, B. Bunday, D. DiPaola, W. Advocate, T. Murray, P. Hansen, S. Novak, S. Bennett, M. Rodgers, B. Baker-O'Neal, B. Sapp, E. Barth, J. Hedrick, R. Goldblatt, S. S. P. Rao, and K. D. Osborn: *Development of transmon qubits solely from optical lithography on 300 mm wafers*. Quantum Science and Technology **4**.2 (2019), p. 025012. DOI: 10.1088/2058-9565/ab0ca8 (cit. on pp. 2, 13, 55, 61).

[Fri+19] S. Fritz, L. Radtke, R. Schneider, M. Weides, and D. Gerthsen: *Optimization of Al/$AlO_x$/Al-layer systems for Josephson junctions from a microstructure point of view*. Journal of Applied Physics **125**.16 (2019), p. 165301. DOI: 10.1063/1.5089871 (cit. on pp. 56, 61).

[Fuc+11] G. D. Fuchs, G. Burkard, P. V. Klimov, and D. D. Awschalom: *A quantum memory intrinsic to single nitrogen-vacancy centres in diamond*. Nature Physics **7**.10 (2011), pp. 789–793. DOI: 10.1038/nphys2026 (cit. on pp. 3, 74).

[GCS17] J. M. Gambetta, J. M. Chow, and M. Steffen: *Building logical qubits in a superconducting quantum computing system*. npj Quantum Information **3**.1 (2017), p. 2. DOI: 10.1038/s41534-016-0004-0 (cit. on p. 5).

[Gam+17] J. M. Gambetta, C. E. Murray, Y.-K.-K. Fung, D. T. McClure, O. Dial, W. Shanks, J. W. Sleight, and M. Steffen: *Investigating Surface Loss Effects in Superconducting Transmon Qubits*. IEEE Transactions on Applied Superconductivity **27**.1 (2017), pp. 1–5. DOI: 10.1109/TASC.2016.2629670 (cit. on pp. 23, 68).

[GRM20] G. García-Pérez, M. A. C. Rossi, and S. Maniscalco: *IBM Q Experience as a versatile experimental testbed for simulating open quantum systems*. npj Quantum Information **6**.1 (2020), p. 1. DOI: 10.1038/s41534-019-0235-y (cit. on pp. 3, 71).

[Gea90] J. Gea-Banacloche: *Collapse and Revival of the State Vector in the Jaynes-Cummings Model*. Phys. Rev. Lett. **65**.27 (1990), pp. 3421–3424. URL: https://journals.aps.org/prl/pdf/10.1103/PhysRevLett.65.3385 (cit. on p. 80).

[GS20] M. F. Gely and G. A. Steele: *QuCAT: quantum circuit analyzer tool in Python*. New Journal of Physics **22**.1 (2020), p. 013025. DOI: 10.1088/1367-2630/ab60f6 (cit. on p. 44).

[GAN14] I. M. Georgescu, S. Ashhab, and F. Nori: *Quantum simulation*. Reviews of Modern Physics **86**.1 (2014), pp. 153–185. DOI: 10.1103/RevModPhys.86.153 (cit. on pp. 13, 72).

[GKK05] C. Gerry, P. Knight, and P. L. Knight: *Introduction to quantum optics*. Campbridge university press, 2005, p. 332 (cit. on pp. 17, 19, 20, 24, 25).

[Gol+13] M. Goldstein, M. H. Devoret, M. Houzet, and L. I. Glazman: *Inelastic Microwave Photon Scattering off a Quantum Impurity in a Josephson-Junction Array*. Physical Review Letters **110**.1 (2013), p. 017002. DOI: 10.1103/PhysRevLett.110.017002 (cit. on pp. 73, 94).

[Göp+08] M. Göppl, A. Fragner, M. Baur, R. Bianchetti, S. Filipp, J. M. Fink, P. J. Leek, G. Puebla, L. Steffen, and A. Wallraff: *Coplanar waveguide resonators for circuit quantum electrodynamics*. Journal of Applied Physics **104**.11 (2008), p. 113904. DOI: 10.1063/1.3010859 (cit. on p. 38).

[Gra+17] S. E. de Graaf, A. A. Adamyan, T. Lindström, D. Erts, S. E. Kubatkin, A. Y. Tzalenchuk, and A. V. Danilov: *Direct Identification of Dilute Surface Spins on $Al_2O_3$: Origin of Flux Noise in Quantum Circuits*. Physical Review Letters **118**.5 (2017), p. 057703. DOI: 10.1103/PhysRevLett.118.057703 (cit. on p. 23).

[Gra+12] G. J. Grabovskij, T. Peichl, J. Lisenfeld, G. Weiss, and A. V. Ustinov: *Strain Tuning of Individual Atomic Tunneling Systems Detected by a Superconducting Qubit*. Science **338**.6104 (2012), pp. 232–234. DOI: 10.1126/science.1226487 (cit. on p. 23).

[GM12] R. Gross and A. Marx: *Festkörperphysik*. München: Oldenbourg Wissenschaftsverlag Verlag, 2012. DOI: 10.1524/9783486714869 (cit. on p. 6).

[Gro96] L. K. Grover: *A fast quantum mechanical algorithm for database search*. *Proceedings of the twenty-eighth annual ACM symposium on Theory of computing - STOC '96*. New York, New York, USA: ACM Press, 1996, pp. 212–219. DOI: 10.1145/237814.237866 (cit. on pp. 1, 13).

[Grü+17] L. Grünhaupt, U. Von Lüpke, D. Gusenkova, S. T. Skacel, N. Maleeva, S. Schlör, A. Bilmes, H. Rotzinger, A. V. Ustinov, M. Weides, and I. M. Pop: *An argon ion beam milling process for native AlOx layers enabling coherent superconducting contacts*. Applied Physics Letters **111**.7 (2017), p. 072601. DOI: 10.1063/1.4990491 (cit. on pp. 58, 62).

[Gu+17] X. Gu, A. F. Kockum, A. Miranowicz, Y.-x. Liu, and F. Nori: *Microwave photonics with superconducting quantum circuits*. Physics Reports **718-719** (2017), pp. 1–102. DOI: 10.1016/j.physrep.2017.10.002 (cit. on p. 35).

[Gye+19] A. Gyenis, P. S. Mundada, A. Di Paolo, T. M. Hazard, X. You, D. I. Schuster, J. Koch, A. Blais, and A. A. Houck: *Experimental realization of an intrinsically error-protected superconducting qubit* (2019). URL: http://arxiv.org/abs/1910.07542 (cit. on pp. 22, 44).

[Hen+19] F. Henriques, F. Valenti, T. Charpentier, M. Lagoin, C. Gouriou, M. Martínez, L. Cardani, M. Vignati, L. Grünhaupt, D. Gusenkova, J. Ferrero, S. T. Skacel, W. Wernsdorfer, A. V. Ustinov, G. Catelani, O. Sander, and I. M. Pop: *Phonon traps reduce the quasiparticle density in superconducting circuits*. Applied Physics Letters **115**.21 (2019), p. 212601. DOI: 10.1063/1.5124967 (cit. on p. 23).

[Hon+20] S. S. Hong, A. T. Papageorge, P. Sivarajah, G. Crossman, N. Didier, A. M. Polloreno, E. A. Sete, S. W. Turkowski, M. P. Da Silva, and B. R. Johnson: *Demonstration of a parametrically activated entangling gate protected from flux noise*. Physical Review A **101**.1 (2020), pp. 1–8. DOI: 10.1103/PhysRevA.101.012302 (cit. on p. 65).

[Hou+07] A. A. Houck, D. I. Schuster, J. M. Gambetta, J. A. Schreier, B. R. Johnson, J. M. Chow, L. Frunzio, J. Majer, M. H. Devoret, S. M. Girvin, and R. J. Schoelkopf: *Generating single microwave photons in a circuit*. Nature **449**.7160 (2007), pp. 328–331. DOI: 10.1038/nature06126 (cit. on p. 30).

[Hua+11] P. Huang, J. Zhou, F. Fang, X. Kong, X. Xu, C. Ju, and J. Du: *Landau-Zener-Stückelberg Interferometry of a Single Electronic Spin in a Noisy Environment*. Physical Review X **1**.1 (2011), p. 011003. DOI: 10.1103/PhysRevX.1.011003 (cit. on pp. 4, 75).

[Hut+17] M. D. Hutchings, J. B. Hertzberg, Y. Liu, N. T. Bronn, G. A. Keefe, M. Brink, J. M. Chow, and B. L. Plourde: *Tunable Superconducting Qubits with Flux-Independent Coherence*. Physical Review Applied **8**.4 (2017), pp. 1–13. DOI: 10.1103/PhysRevApplied.8.044003 (cit. on p. 31).

[Jef+14] E. Jeffrey, D. Sank, J. Y. Mutus, T. C. White, J. Kelly, R. Barends, Y. Chen, Z. Chen, B. Chiaro, A. Dunsworth, A. Megrant, P. J. J. O'Malley, C. Neill, P. Roushan, A. Vainsencher, J. Wenner, A. N. Cleland, and J. M. Martinis: *Fast Accurate State Measurement with Superconducting Qubits*. Physical Review Letters **112**.19 (2014), p. 190504. DOI: 10.1103/PhysRevLett.112.190504 (cit. on pp. 27, 43, 46).

[JW06] F. Jelezko and J. Wrachtrup: *Single defect centres in diamond: A review*. physica status solidi (a) **203**.13 (2006), pp. 3207–3225. DOI: 10.1002/pssa.200671403 (cit. on p. 1).

[Jin+15] X. Y. Jin, A. Kamal, A. P. Sears, T. Gudmundsen, D. Hover, J. Miloshi, R. Slattery, F. Yan, J. Yoder, T. P. Orlando, S. Gustavsson, and W. D. Oliver: *Thermal and Residual Excited-State Population in a 3D Transmon Qubit*. Physical Review Letters **114**.24 (2015), p. 240501. DOI: 10.1103/PhysRevLett.114.240501 (cit. on p. 50).

[Jos62] B. Josephson: *Possible new effects in superconductive tunnelling*. Physics Letters **1**.7 (1962), pp. 251–253. DOI: 10.1016/0031-9163(62)91369-0 (cit. on p. 6).

[Kat+06] N. Katz, M. Ansmann, R. C. Bialczak, E. Lucero, R. McDermott, M. Neeley, M. Steffen, E. M. Weig, A. N. Cleland, M. M. John, and A. N. Korotkov: *Coherent State Evolution in a Superconducting Qubit from Partial-Collapse Measurement*. Science **312**.5779 (2006), pp. 1498–1500. DOI: 10.1126/science.1126475 (cit. on p. 21).

[Kit06] A. Kitaev: *Protected qubit based on a superconducting current mirror* (2006), pp. 1–6. URL: http://arxiv.org/abs/cond-mat/0609441 (cit. on p. 44).

[Kja+20] M. Kjaergaard, M. E. Schwartz, J. Braumüller, P. Krantz, J. I.-J. Wang, S. Gustavsson, and W. D. Oliver: *Superconducting Qubits: Current State of Play*. Annual Review of Condensed Matter Physics **11**.1 (2020), pp. 369–395. DOI: 10.1146/annurev-conmatphys-031119-050605 (cit. on pp. 2, 13, 28, 30, 55).

[KMM95] A. Kleinsasser, R. Miller, and W. Mallison: *Dependence of critical current density on oxygen exposure in Nb-AlO$_x$-Nb tunnel junctions*. IEEE Transactions on Appiled Superconductivity **5**.1 (1995), pp. 26–30. DOI: 10.1109/77.384565 (cit. on p. 62).

[Koc+07] J. Koch, T. M. Yu, J. Gambetta, A. A. Houck, D. I. Schuster, J. Majer, A. Blais, M. H. Devoret, S. M. Girvin, and R. J. Schoelkopf: *Charge-insensitive qubit design derived from the Cooper pair box*. Physical Review A **76**.4 (2007), p. 42319. DOI: 10.1103/PhysRevA.76.042319 (cit. on pp. 22, 23, 27, 28, 30, 32).

[Kra+19] P. Krantz, M. Kjaergaard, F. Yan, T. P. Orlando, S. Gustavsson, and W. D. Oliver: *A quantum engineer's guide to superconducting qubits*. Applied Physics Reviews **6**.2 (2019), p. 021318. DOI: 10.1063/1.5089550 (cit. on pp. 13–15, 18, 21, 24, 31, 48, 55, 94).

[Kre+20] J. M. Kreikebaum, K. P. O'Brien, A. Morvan, and I. Siddiqi: *Improving wafer-scale Josephson junction resistance variation in superconducting quantum coherent circuits*. Superconductor Science and Technology **33**.6 (2020), 06LT02. DOI: 10.1088/1361-6668/ab8617 (cit. on pp. 2, 13, 55, 61, 64).

[Kri+19] S. Krinner, S. Storz, P. Kurpiers, P. Magnard, J. Heinsoo, R. Keller, J. Lütolf, C. Eichler, and A. Wallraff: *Engineering cryogenic setups for 100-qubit scale superconducting circuit systems*. EPJ Quantum Technology **6**.1 (2019), p. 2. DOI: 10.1140/epjqt/s40507-019-0072-0 (cit. on pp. 48, 50).

[Kri+20] M. Kristen, A. Schneider, A. Stehli, T. Wolz, S. Danilin, H. S. Ku, J. Long, X. Wu, R. Lake, D. P. Pappas, A. V. Ustinov, and M. Weides: *Amplitude and frequency sensing of microwave fields with a superconducting transmon qudit*. npj Quantum Information **6**.1 (2020), p. 57. DOI: 10.1038/s41534-020-00287-w (cit. on p. 24).

[Kum+16] P. Kumar, S. Sendelbach, M. A. Beck, J. W. Freeland, Z. Wang, H. Wang, C. C. Yu, R. Q. Wu, D. P. Pappas, and R. McDermott: *Origin and Reduction of 1/f Magnetic Flux Noise in Superconducting Devices*. Physical Review Applied **6**.4 (2016), p. 041001. DOI: 10.1103/PhysRevApplied.6.041001 (cit. on p. 23).

[Lam+18] L. Lamata, A. Parra-Rodriguez, M. Sanz, and E. Solano: *Digital-analog quantum simulations with superconducting circuits*. Advances in Physics: X **3**.1 (2018), p. 1457981. DOI: 10.1080/23746149.2018.1457981 (cit. on p. 13).

[Lan32] L. D. Landau: *On the theory of transfer of energy at collissions II*. Phys. Z. Sowjetunion **2**.46 (1932), p. 118 (cit. on pp. 3, 73).

[Lan17] K. Landsman: *Foundations of Quantum Theory*. Vol. 188. Fundamental Theories of Physics. Cham: Springer International Publishing, 2017. DOI: 10.1007/978-3-319-51777-3 (cit. on p. 16).

[Le 12] K. Le Hur: *Kondo resonance of a microwave photon*. Physical Review B **85**.14 (2012), p. 140506. DOI: 10.1103/PhysRevB.85.140506 (cit. on pp. 73, 94).

[Lec+11] F. Lecocq, I. M. Pop, Z. Peng, I. Matei, T. Crozes, T. Fournier, C. Naud, W. Guichard, and O. Buisson: *Junction fabrication by shadow evaporation without a suspended bridge*. Nanotechnology **22**.31 (2011), p. 315302. DOI: 10.1088/0957-4484/22/31/315302 (cit. on pp. 2, 60).

[Leg+87] A. J. Leggett, S. Chakravarty, A. T. Dorsey, M. P. A. Fisher, A. Garg, and W. Zwerger: *Dynamics of the dissipative two-state system*. Reviews of Modern Physics **59**.1 (1987), pp. 1–85. DOI: 10.1103/RevModPhys.59.1 (cit. on pp. 73, 94).

[Lep+18] J. Leppäkangas, J. Braumüller, M. Hauck, J.-M. Reiner, I. Schwenk, S. Zanker, L. Fritz, A. V. Ustinov, M. Weides, and M. Marthaler: *Quantum simulation of the spin-boson model with a microwave circuit*. Physical Review A **97**.5 (2018), p. 052321. DOI: 10.1103/PhysRevA.97.052321 (cit. on pp. 73, 94).

[Lie+19] B. Lienhard, S. Gustavsson, W. D. Oliver, J. Braumuller, W. Woods, D. Rosenberg, G. Calusine, S. Weber, A. Vepsalainen, K. O'Brien, and T. P. Orlando: *Microwave Packaging for Superconducting Qubits*. *2019 IEEE MTT-S International Microwave Symposium (IMS)*. Vol. 2019-June. IEEE, 2019, pp. 275–278. DOI: 10.1109/MWSYM.2019.8701119 (cit. on pp. 48, 49).

[LS91] K. Likharev and V. Semenov: *RSFQ logic/memory family: a new Josephson-junction technology for sub-terahertz-clock-frequency digital systems*. IEEE Transactions on Applied Superconductivity **1**.1 (1991), pp. 3–28. DOI: 10.1109/77.80745 (cit. on p. 5).

[Lis+19] J. Lisenfeld, A. Bilmes, A. Megrant, R. Barends, J. Kelly, P. Klimov, G. Weiss, J. M. Martinis, and A. V. Ustinov: *Electric field spectroscopy of material defects in transmon qubits*. npj Quantum Information **5**.1 (2019), p. 105. DOI: 10.1038/s41534-019-0224-1 (cit. on p. 62).

[Mac+15] C. Macklin, K. O'Brien, D. Hover, M. E. Schwartz, V. Bolkhovsky, X. Zhang, W. D. Oliver, and I. Siddiqi: *A near-quantum-limited Josephson traveling-wave parametric amplifier*. Science **350**.6258 (2015), pp. 307–310. DOI: 10.1126/science.aaa8525 (cit. on pp. 2, 24, 61).

[MSS01] Y. Makhlin, G. Schön, and A. Shnirman: *Quantum-state engineering with Josephson-junction devices*. Reviews of Modern Physics **73**.2 (2001), pp. 357–400. DOI: 10.1103/RevModPhys.73.357 (cit. on pp. 2, 13).

[Man+09] V. E. Manucharyan, J. Koch, L. I. Glazman, and M. H. Devoret: *Fluxonium: Single Cooper-Pair Circuit Free of Charge Offsets*. Science **326**.5949 (2009), pp. 113–116. DOI: 10.1126/science.1175552 (cit. on p. 22).

[Man20] D. Manzano: *A short introduction to the Lindblad master equation*. AIP Advances **10**.2 (2020), p. 025106. DOI: 10.1063/1.5115323 (cit. on pp. 3, 20, 71, 73).

[Mar+05] J. M. Martinis, K. B. Cooper, R. McDermott, M. Steffen, M. Ansmann, K. D. Osborn, K. Cicak, S. Oh, D. P. Pappas, R. W. Simmonds, and C. C. Yu: *Decoherence in Josephson Qubits from Dielectric Loss*. Physical Review Letters **95**.21 (2005), p. 210503. DOI: 10.1103/PhysRevLett.95.210503 (cit. on pp. 23, 61).

[McA+20] S. McArdle, S. Endo, A. Aspuru-Guzik, S. C. Benjamin, and X. Yuan: *Quantum computational chemistry*. Reviews of Modern Physics **92**.1 (2020), p. 015003. DOI: 10.1103/RevModPhys.92.015003 (cit. on pp. 3, 13).

[McK+16] D. C. McKay, S. Filipp, A. Mezzacapo, E. Magesan, J. M. Chow, and J. M. Gambetta: *Universal Gate for Fixed-Frequency Qubits via a Tunable Bus*. Physical Review Applied **6**.6 (2016), p. 064007. DOI: 10.1103/PhysRevApplied.6.064007 (cit. on p. 27).

[McK+15] D. C. McKay, R. Naik, P. Reinhold, L. S. Bishop, and D. I. Schuster: *High-contrast qubit interactions using multimode cavity QED*. Physical Review Letters **114**.8 (2015), pp. 1–5. DOI: 10.1103/PhysRevLett.114.080501 (cit. on p. 74).

[McR+20] C. R. H. McRae, H. Wang, J. Gao, M. Vissers, T. Brecht, A. Dunsworth, D. Pappas, and J. Mutus: *Materials loss measurements using superconducting microwave resonators* (2020). URL: http://arxiv.org/abs/2006.04718 (cit. on p. 23).

[Mes06] D. Meschede: *Gerthsen Physik*. Ed. by D. Meschede. Springer-Lehrbuch. Berlin/Heidelberg: Springer-Verlag, 2006. DOI: 10.1007/3-540-29973-4 (cit. on p. 36).

[Min+19] Z. K. Minev, S. O. Mundhada, S. Shankar, P. Reinhold, R. Gutiérrez-Jáuregui, R. J. Schoelkopf, M. Mirrahimi, H. J. Carmichael, and M. H. Devoret: *To catch and reverse a quantum jump mid-flight*. Nature **570**.7760 (2019), pp. 200–204. DOI: 10.1038/s41586-019-1287-z (cit. on p. 21).

[MK13] C. Monroe and J. Kim: *Scaling the Ion Trap Quantum Processor*. Science **339**.6124 (2013), pp. 1164–1169. DOI: 10.1126/science.1231298 (cit. on pp. 1, 13).

[Mon+95] C. Monroe, D. M. Meekhof, B. E. King, W. M. Itano, and D. J. Wineland: *Demonstration of a Fundamental Quantum Logic Gate*. Physical Review Letters **75**.25 (1995), pp. 4714–4717. DOI: 10.1103/PhysRevLett.75.4714 (cit. on pp. 1, 13).

[Mos+17] S. Mostame, J. Huh, C. Kreisbeck, A. J. Kerman, T. Fujita, A. Eisfeld, and A. Aspuru-Guzik: *Emulation of complex open quantum systems using superconducting qubits*. Quantum Information Processing **16**.2 (2017), p. 44. DOI: 10.1007/s11128-016-1489-3 (cit. on p. 3).

[MCL19] C. Müller, J. H. Cole, and J. Lisenfeld: *Towards understanding two-level-systems in amorphous solids: insights from quantum circuits*. Reports on Progress in Physics **82**.12 (2019), p. 124501. DOI: 10.1088/1361-6633/ab3a7e (cit. on pp. 23, 30, 79).

[Nee+08] M. Neeley, M. Ansmann, R. C. Bialczak, M. Hofheinz, N. Katz, E. Lucero, A. O'Connell, H. Wang, A. N. Cleland, and J. M. Martinis: *Process tomography of quantum memory in a Josephson-phase qubit coupled to a two-level state*. Nature Physics **4**.7 (2008), pp. 523–526. DOI: 10.1038/nphys972 (cit. on p. 94).

[Ner+19] A. Nersisyan, E. A. Sete, S. Stanwyck, A. Bestwick, M. Reagor, S. Poletto, N. Alidoust, R. Manenti, R. Renzas, C.-V. Bui, K. Vu, T. Whyland, and Y. Mohan: *Manufacturing low dissipation superconducting quantum processors*. *2019 IEEE International Electron Devices Meeting (IEDM)*. Vol. 2019-Decem. IEEE, 2019, pp. 31.1.1–31.1.4. DOI: 10.1109/IEDM19573.2019.8993458 (cit. on pp. 2, 23, 44, 55).

[Neu46] F. E. Neumann: *Allgemeine Gesetze der induzierten elektrischen Ströme*. Annalen der Physik und Chemie **143**.1 (1846), pp. 31–44. DOI: 10.1002/andp.18461430103 (cit. on p. 48).

[Nit06] A. Nitzan: *Chemical dynamics in condensed phases: relaxation, transfer and reactions in condensed molecular systems*. Oxford university press, 2006 (cit. on pp. 3, 73, 92).

[Nvi18] Nvidia: *Nvidia turing GPU architecture*. (2018). URL: https://www.nvidia.com/content/dam/en-zz/Solutions/design-visualization/technologies/turing-architecture/NVIDIA-Turing-Architecture-Whitepaper.pdf (visited on 12/21/2020) (cit. on p. 1).

[Oli+05] W. D. Oliver, Y. Yu, J. C. Lee, K. K. Berggren, L. S. Levitov, and T. P. Orlando: *Mach-Zehnder Interferometry in a Strongly Driven Superconducting Qubit*. Science **310**.5754 (2005), pp. 1653–1657. DOI: 10.1126/science.1119678 (cit. on pp. 3, 73, 74).

[OIL10] P. P. Orth, A. Imambekov, and K. Le Hur: *Universality in dissipative Landau-Zener transitions*. Physical Review A - Atomic, Molecular, and Optical Physics **82**.3 (2010), pp. 1–5. DOI: 10.1103/PhysRevA.82.032118 (cit. on pp. 4, 75).

[OIL13] P. P. Orth, A. Imambekov, and K. Le Hur: *Nonperturbative stochastic method for driven spin-boson model*. Physical Review B **87**.1 (2013), pp. 119–123. DOI: 10.1103/PhysRevB.87.014305 (cit. on pp. 3, 4, 71, 75).

[OHM18] T. Ota, K. Hitachi, and K. Muraki: *Landau-Zener-Stückelberg interference in coherent charge oscillations of a one-electron double quantum dot*. Scientific Reports **8**.1 (2018), p. 5491. DOI: 10.1038/s41598-018-23468-2 (cit. on pp. 3, 74).

[Our17] Ourworldindata: *Moore's law: transistor*. (2017). URL: https://ourworld%7B~%7Dindata.org/grapher/transistors-per-microprocessor?time=earliest..2017 (visited on 12/20/2020) (cit. on p. 1).

[Pai+11] H. Paik, D. I. Schuster, L. S. Bishop, G. Kirchmair, G. Catelani, A. P. Sears, B. R. Johnson, M. J. Reagor, L. Frunzio, L. I. Glazman, S. M. Girvin, M. H. Devoret, and R. J. Schoelkopf: *Observation of high coherence in Josephson junction qubits measured in a three-dimensional circuit QED architecture*. Physical Review Letters **107**.24 (2011), p. 240501. DOI: 10.1103/PhysRevLett.107.240501 (cit. on pp. 38, 44, 55).

[Pet+05] J. R. Petta, A. C.Johnson, J. M. Taylor, E. A. Laird, A. Yacoby, M. D. Lukin, C. M. Marcus, M. P. Hanson, and A. C. Gossard: *Coherent Manipulation of Coupled Electron Spins in Semiconductor Quantum Dots*. Science **309**.2005 (2005), p. 2180. DOI: 10.1126/science.1116955 (cit. on p. 13).

[PLG10] J. R. Petta, H. Lu, and A. C. Gossard: *A Coherent Beam Splitter for Electronic Spin States*. Science **327**.5966 (2010), pp. 669–672. DOI: 10.1126/science.1183628 (cit. on pp. 3, 74).

[Phi59] N. E. Phillips: *Heat Capacity of Aluminum between 0.1 K and 4.0 K*. Physical Review **114**.3 (1959), pp. 676–685. DOI: 10.1103/PhysRev.114.676 (cit. on p. 9).

[Pla+20] A. P. M. Place, L. V. H. Rodgers, P. Mundada, B. M. Smitham, M. Fitzpatrick, Z. Leng, A. Premkumar, J. Bryon, S. Sussman, G. Cheng, T. Madhavan, H. K. Babla, B. Jaeck, A. Gyenis, N. Yao, R. J. Cava, N. P. de Leon, and A. A. Houck: *New material platform for superconducting transmon qubits with coherence times exceeding 0.3 milliseconds* (2020). URL: http://arxiv.org/abs/2003.00024 (cit. on pp. 2, 23, 28, 44, 55, 56, 61, 68).

[Pop+12] I. M. Pop, T. Fournier, T. Crozes, F. Lecocq, I. Matei, B. Pannetier, O. Buisson, and W. Guichard: *Fabrication of stable and reproducible sub-micron tunnel junctions*. Journal of Vacuum Science & Technology B, Nanotechnology and Microelectronics: Materials, Processing, Measurement, and Phenomena **30**.1 (2012), p. 010607. DOI: 10.1116/1.3673790 (cit. on pp. 61, 65).

[Pop+14] I. M. Pop, K. Geerlings, G. Catelani, R. J. Schoelkopf, L. I. Glazman, and M. H. Devoret: *Coherent suppression of electromagnetic dissipation due to superconducting quasiparticles*. Nature **508**.7496 (2014), pp. 369–372. DOI: 10.1038/nature13017 (cit. on pp. 23, 44).

[Poz11] D. M. Pozar: *Microwave Engineering*. 4th ed. John Wiley & Sons, Inc., 2011, p. 752 (cit. on pp. 35–37, 40, 41).

[Pre18] J. Preskill: *Quantum Computing in the NISQ era and beyond*. Quantum **2**.July (2018), p. 79. DOI: 10.22331/q-2018-08-06-79 (cit. on pp. 3, 13, 71, 72).

[Pro+15] S. Probst, F. B. Song, P. A. Bushev, A. V. Ustinov, and M. Weides: *Efficient and robust analysis of complex scattering data under noise in microwave resonators*. Review of Scientific Instruments **86**.2 (2015), p. 024706. DOI: 10.1063/1.4907935 (cit. on pp. 42, 77).

[Pue+19] R. Puebla, G. Zicari, I. Arrazola, E. Solano, M. Paternostro, and J. Casanova: *Spin-Boson Model as A Simulator of Non-Markovian Multiphoton Jaynes-Cummings Models*. Symmetry **11**.5 (2019), p. 695. DOI: 10.3390/sym11050695 (cit. on pp. 3, 71, 73, 94).

[PTP46] E. M. Purcell, H. C. Torrey, and R. V. Pound: *Resonance Absorption by Nuclear Magnetic Moments in a Solid*. Physical Review **69**.1-2 (1946), pp. 37–38. DOI: 10.1103/PhysRev.69.37 (cit. on p. 23).

[Qki20] Qkit collaborators: *Qkit – a quantum measurement and evaluation suite in python.* (2020). URL: https://github.com/qkitgroup/qkit (visited on 12/21/2020) (cit. on pp. 53, 78).

[Qui+14] C. M. Quintana, A. Megrant, Z. Chen, A. Dunsworth, B. Chiaro, R. Barends, B. Campbell, Y. Chen, I.-C. Hoi, E. Jeffrey, J. Kelly, J. Y. Mutus, P. J. J. O'Malley, C. Neill, P. Roushan, D. Sank, A. Vainsencher, J. Wenner, T. C. White, A. N. Cleland, and J. M. Martinis: *Characterization and reduction of microfabrication-induced decoherence in superconducting quantum circuits*. Applied Physics Letters **105**.6 (2014), p. 062601. DOI: 10.1063/1.4893297 (cit. on p. 61).

[Rab37] I. I. Rabi: *Space Quantization in a Gyrating Magnetic Field*. Physical Review **51**.8 (1937), pp. 652–654. DOI: 10.1103/PhysRev.51.652 (cit. on p. 18).

[Rea+16] M. Reagor, W. Pfaff, C. Axline, R. W. Heeres, N. Ofek, K. Sliwa, E. Holland, C. Wang, J. Blumoff, K. Chou, M. J. Hatridge, L. Frunzio, M. H. Devoret, L. Jiang, and R. J. Schoelkopf: *Quantum memory with millisecond coherence in circuit QED*. Physical Review B **94**.1 (2016), p. 014506. DOI: 10.1103/PhysRevB.94.014506 (cit. on p. 94).

[Ree+10] M. D. Reed, L. DiCarlo, B. R. Johnson, L. Sun, D. I. Schuster, L. Frunzio, and R. J. Schoelkopf: *High-Fidelity Readout in Circuit Quantum Electrodynamics Using the Jaynes-Cummings Nonlinearity*. Physical Review Letters **105**.17 (2010), p. 173601. DOI: 10.1103/PhysRevLett.105.173601 (cit. on p. 24).

[Rig+12] C. Rigetti, J. M. Gambetta, S. Poletto, B. L. Plourde, J. M. Chow, A. D. Córcoles, J. A. Smolin, S. T. Merkel, J. R. Rozen, G. A. Keefe, M. B. Rothwell, M. B. Ketchen, and M. Steffen: *Superconducting qubit in a waveguide cavity with a coherence time approaching 0.1 ms*. Physical Review B **86**.10 (2012), p. 100506. DOI: 10.1103/PhysRevB.86.100506 (cit. on p. 38).

[RC19] R.-P. Riwar and G. Catelani: *Efficient quasiparticle traps with low dissipation through gap engineering*. Physical Review B **100**.14 (2019), p. 144514. DOI: 10.1103/PhysRevB.100.144514 (cit. on p. 23).

[Riw+16] R.-P. Riwar, A. Hosseinkhani, L. D. Burkhart, Y. Y. Gao, R. J. Schoelkopf, L. I. Glazman, and G. Catelani: *Normal-metal quasiparticle traps for superconducting qubits*. Physical Review B **94**.10 (2016), p. 104516. DOI: 10.1103/PhysRevB.94.104516 (cit. on p. 23).

[Roc+12] N. Roch, E. Flurin, F. Nguyen, P. Morfin, P. Campagne-Ibarcq, M. H. Devoret, and B. Huard: *Widely Tunable, Nondegenerate Three-Wave Mixing Microwave Device Operating near the Quantum Limit*. Physical Review Letters **108**.14 (2012), p. 147701. DOI: 10.1103/PhysRevLett.108.147701 (cit. on pp. 2, 24, 61).

[Sai+07] K. Saito, M. Wubs, S. Kohler, Y. Kayanuma, and P. Hänggi: *Dissipative Landau-Zener transitions of a qubit: Bath-specific and universal behavior*. Physical Review B **75**.21 (2007), p. 214308. DOI: 10.1103/PhysRevB.75.214308 (cit. on p. 73).

[Sch20] S. Schlör: *Intrinsic decoherence in superconducting quantumcircuits*. PhD thesis. Karlsruhe Institute of Technology, 2020, p. 135. DOI: 10.5445/IR/1000105563 (cit. on pp. 10, 11).

[Sch+19] S. Schlör, J. Lisenfeld, C. Müller, A. Bilmes, A. Schneider, D. P. Pappas, A. V. Ustinov, and M. Weides: *Correlating Decoherence in Transmon Qubits: Low Frequency Noise by Single Fluctuators*. Physical Review Letters **123**.19 (2019), p. 190502. DOI: 10.1103/PhysRevLett.123.190502 (cit. on pp. 23, 65, 68).

[Sch+18] A. Schneider, J. Braumüller, L. Guo, P. Stehle, H. Rotzinger, M. Marthaler, A. V. Ustinov, and M. Weides: *Local sensing with the multilevel ac Stark effect*. Physical Review A **97**.6 (2018), pp. 1–8. DOI: 10.1103/PhysRevA.97.062334 (cit. on p. 24).

[Sch+08] J. A. Schreier, A. A. Houck, J. Koch, D. I. Schuster, B. R. Johnson, J. M. Chow, J. M. Gambetta, J. Majer, L. Frunzio, M. H. Devoret, S. M. Girvin, and R. J. Schoelkopf: *Suppressing charge noise decoherence in superconducting charge qubits*. Physical Review B **77**.18 (2008), p. 180502. DOI: 10.1103/PhysRevB.77.180502 (cit. on p. 30).

[Sch+07] D. I. Schuster, A. A. Houck, J. A. Schreier, A. Wallraff, J. M. Gambetta, A. Blais, L. Frunzio, J. Majer, B. Johnson, M. H. Devoret, S. M. Girvin, and R. J. Schoelkopf: *Resolving photon number states in a superconducting circuit*. Nature **445**.7127 (2007), pp. 515–518. DOI: 10.1038/nature05461 (cit. on p. 25).

[Sch07] F. Schwabl: *Quantenmechanik (QM I)*. Springer-Lehrbuch. Berlin, Heidelberg: Springer Berlin Heidelberg, 2007. DOI: 10.1007/978-3-540-73675-2 (cit. on pp. 74, 83).

[Sci+20] M. Scigliuzzo, A. Bengtsson, J.-C. Besse, A. Wallraff, P. Delsing, and S. Gasparinetti: *Primary thermometry of propagating microwaves in the quantum regime* (2020), pp. 1–12. URL: http://arxiv.org/abs/2003.13522 (cit. on p. 50).

[Ser+18] K. Serniak, M. Hays, G. de Lange, S. Diamond, S. Shankar, L. D. Burkhart, L. Frunzio, M. Houzet, and M. H. Devoret: *Hot Nonequilibrium Quasiparticles in Transmon Qubits*. Physical Review Letters **121**.15 (2018), p. 157701. DOI: 10.1103/PhysRevLett.121.157701 (cit. on p. 50).

[SMK15] E. A. Sete, J. M. Martinis, and A. N. Korotkov: *Quantum theory of a bandpass Purcell filter for qubit readout*. Physical Review A **92**.1 (2015), p. 012325. DOI: 10.1103/PhysRevA.92.012325 (cit. on pp. 27, 43).

[Sha+10] Y. Shalibo, Y. Rofe, D. Shwa, F. Zeides, M. Neeley, J. M. Martinis, and N. Katz: *Lifetime and Coherence of Two-Level Defects in a Josephson Junction*. Physical Review Letters **105**.17 (2010), p. 177001. DOI: 10.1103/PhysRevLett.105.177001 (cit. on p. 79).

[SMS02] A. Shnirman, Y. Makhlin, and G. Schön: *Noise and decoherence in quantum two-level systems*. Physica Scripta T **102** (2002), pp. 147–154. DOI: 10.1238/physica.topical.102a00147 (cit. on p. 94).

[Sho97] P. W. Shor: *Polynomial-Time Algorithms for Prime Factorization and Discrete Logarithms on a Quantum Computer*. SIAM Journal on Computing **26**.5 (1997), pp. 1484–1509. DOI: 10.1137/S0097539795293172 (cit. on pp. 1, 13).

[Shy04] A. V. Shytov: *Landau-zener transitions in a multilevel system: An exact result*. Physical Review A **70**.5 A (2004), pp. 2–4. DOI: 10.1103/PhysRevA.70.052708 (cit. on p. 73).

[Sil+06] M. Sillanpää, T. Lehtinen, A. Paila, Y. Makhlin, and P. Hakonen: *Continuous-time monitoring of Landau-Zener interference in a cooper-pair box*. Physical Review Letters **96**.18 (2006), pp. 1–4. DOI: 10.1103/PhysRevLett.96.187002 (cit. on pp. 3, 74).

[Sim+04] R. Simmonds, K. Lang, D. Hite, S. Nam, D. Pappas, and J. Martinis: *Decoherence in Josephson Phase Qubits from Junction Resonators*. Physical Review Letters **93**.7 (2004), p. 077003. DOI: 10.1103/PhysRevLett.93.077003 (cit. on p. 23).

[Sim01] R. N. Simons: *Coplanar waveguide circuits, components, and systems*. 1st ed. John Wiley & Sons, Inc., 2001, p. 464 (cit. on p. 36).

[Sok16] A. Sokolov: *Optimal conditions for high-fidelity dispersive readout of a qubit with a photon-number-resolving detector*. Physical Review A **93**.3 (2016), p. 032323. DOI: 10.1103/PhysRevA.93.032323 (cit. on p. 47).

[Ste+06] M. Steffen, M. Ansmann, R. McDermott, N. Katz, R. C. Bialczak, E. Lucero, M. Neeley, E. M. Weig, A. N. Cleland, and J. M. Martinis: *State Tomography of Capacitively Shunted Phase Qubits with High Fidelity*. Physical Review Letters **97**.5 (2006), p. 050502. DOI: 10.1103/PhysRevLett.97.050502 (cit. on pp. 21, 61).

[Ste+20] A. Stehli, J. D. Brehm, T. Wolz, P. Baity, S. Danilin, V. Seferai, H. Rotzinger, A. V. Ustinov, and M. Weides: *Coherent superconducting qubits from a subtractive junction fabrication process*. Applied Physics Letters **117**.12 (2020), p. 124005. DOI: 10.1063/5.0023533 (cit. on pp. 4, 21, 51, 55, 60, 62–64, 66–69, 91, 92).

[Stü32] E. C. G. Stückelberg: *Theorie der unelastischen Stösse zwischen Atomen*. Helv. Phys. Acta, (Basel) **5** (1932), pp. 369–422 (cit. on pp. 3, 73).

[Suk+01] K. Sukhatme, Y. Mukharsky, T. Chul, and D. Pearson: *Observation of the ideal josephson effect in superfluid 4He*. Nature **411**.6835 (2001), pp. 280–283. DOI: 10.1038/35077024 (cit. on p. 7).

[Tsi+20] I. Tsioutsios, K. Serniak, S. Diamond, V. V. Sivak, Z. Wang, S. Shankar, L. Frunzio, R. J. Schoelkopf, and M. H. Devoret: *Free-standing silicon shadow masks for transmon qubit fabrication*. AIP Advances **10**.6 (2020), p. 065120. DOI: 10.1063/1.5138953 (cit. on pp. 2, 55, 61).

[VSS11] R. Vijay, D. H. Slichter, and I. Siddiqi: *Observation of Quantum Jumps in a Superconducting Artificial Atom*. Physical Review Letters **106**.11 (2011), p. 110502. DOI: 10.1103/PhysRevLett.106.110502 (cit. on p. 21).

[Vis+13] M. R. Vissers, J. Gao, M. Sandberg, S. M. Duff, D. S. Wisbey, K. D. Irwin, and D. P. Pappas: *Proximity-coupled Ti/TiN multilayers for use in kinetic inductance detectors*. Applied Physics Letters **102**.23 (2013), p. 232603. DOI: 10.1063/1.4804286 (cit. on p. 23).

[Vit99] N. V. Vitanov: *Transition times in the Landau-Zener model*. Physical Review A **59**.2 (1999), pp. 988–994. DOI: 10.1103/PhysRevA.59.988 (cit. on pp. 4, 75).

[Wal16] M. M. Waldrop: *The chips are down for Moore's law*. Nature **530**.7589 (2016), pp. 144–147. DOI: 10.1038/530144a (cit. on p. 1).

[Wal+04] A. Wallraff, D. I. Schuster, A. Blais, L. Frunzio, R. S. Huang, J. Majer, S. Kumar, S. M. Girvin, and R. J. Schoelkopf: *Strong coupling of a single photon to a superconducting qubit using circuit quantum electrodynamics*. Nature **431**.7005 (2004), pp. 162–167. DOI: 10.1038/nature02851 (cit. on pp. 23, 24, 73).

[Wan+14] C. Wang, Y. Y. Gao, I. M. Pop, U. Vool, C. Axline, T. Brecht, R. W. Heeres, L. Frunzio, M. H. Devoret, G. Catelani, L. I. Glazman, and R. J. Schoelkopf: *Measurement and control of quasiparticle dynamics in a superconducting qubit*. Nature Communications **5**.1 (2014), p. 5836. DOI: 10.1038/ncomms6836 (cit. on p. 23).

[Wei+11a] M. Weides, R. C. Bialczak, M. Lenander, E. Lucero, M. Mariantoni, M. Neeley, A. D. O'Connell, D. Sank, H. Wang, J. Wenner, T. Yamamoto, Y. Yin, A. N. Cleland, and J. Martinis: *Phase qubits fabricated with trilayer junctions*. Superconductor Science and Technology **24**.5 (2011), p. 055005. DOI: 10.1088/0953-2048/24/5/055005 (cit. on p. 61).

[Wei+11b] M. P. Weides, J. S. Kline, M. R. Vissers, M. O. Sandberg, D. S. Wisbey, B. R. Johnson, T. A. Ohki, and D. P. Pappas: *Coherence in a transmon qubit with epitaxial tunnel junctions*. Applied Physics Letters **99**.26 (2011), p. 262502. DOI: 10.1063/1.3672000 (cit. on p. 61).

[Wen17] G. Wendin: *Quantum information processing with superconducting circuits: a review*. Reports on Progress in Physics **80**.10 (2017), p. 106001. DOI: 10.1088/1361-6633/aa7e1a (cit. on pp. 2, 13).

[WS99] W. Wernsdorfer and R. Sessoli: *Quantum Phase Interference and Parity Effects in Magnetic Molecular Clusters*. Science **284**.5411 (1999), pp. 133–135. DOI: 10.1126/science.284.5411.133 (cit. on pp. 3, 74).

[Win+20] P. Winkel, I. Takmakov, D. Rieger, L. Planat, W. Hasch-Guichard, L. Grünhaupt, N. Maleeva, F. Foroughi, F. Henriques, K. Borisov, J. Ferrero, A. V. Ustinov, W. Wernsdorfer, N. Roch, and I. M. Pop: *Nondegenerate Parametric Amplifiers Based on Dispersion-Engineered Josephson-Junction Arrays*. Physical Review Applied **13**.2 (2020), p. 024015. DOI: 10.1103/PhysRevApplied.13.024015 (cit. on pp. 2, 24, 61).

[Wol+20] T. Wolz, A. Stehli, A. Schneider, I. Boventer, R. Macêdo, A. V. Ustinov, M. Kläui, and M. Weides: *Introducing coherent time control to cavity magnon-polariton modes*. Communications Physics **3**.1 (2020), p. 3. DOI: 10.1038/s42005-019-0266-x (cit. on p. 24).

[Wu+17] X. Wu, J. L. Long, H. S. Ku, R. E. Lake, M. Bal, and D. P. Pappas: *Overlap junctions for high coherence superconducting qubits*. Applied Physics Letters **111**.3 (2017), p. 032602. DOI: 10.1063/1.4993937 (cit. on pp. 2, 55, 61).

[Wub+06] M. Wubs, K. Saito, S. Kohler, P. Hänggi, and Y. Kayanuma: *Gauging a quantum heat bath with dissipative Landau-Zener transitions*. Physical Review Letters **97**.20 (2006), pp. 2–5. DOI: 10.1103/PhysRevLett.97.200404 (cit. on p. 73).

[Yan+18] F. Yan, D. Campbell, P. Krantz, M. Kjaergaard, D. Kim, J. L. Yoder, D. Hover, A. Sears, A. J. Kerman, T. P. Orlando, S. Gustavsson, and W. D. Oliver: *Distinguishing Coherent and Thermal Photon Noise in a Circuit Quantum Electrodynamical System*. Physical Review Letters **120**.26 (2018), p. 260504. DOI: 10.1103/PhysRevLett.120.260504 (cit. on pp. 48, 49).

[Yan+16] F. Yan, S. Gustavsson, A. Kamal, J. Birenbaum, A. P. Sears, D. Hover, T. J. Gudmundsen, D. Rosenberg, G. Samach, S. Weber, J. L. Yoder, T. P. Orlando, J. Clarke, A. J. Kerman, and W. D. Oliver: *The flux qubit revisited to enhance coherence and reproducibility*. Nature Communications **7**.1 (2016), p. 12964. DOI: 10.1038/ncomms12964 (cit. on pp. 22, 23).

[Yan+20] P. Yang, J. D. Brehm, J. Leppäkangas, L. Guo, M. Marthaler, I. Boventer, A. Stehli, T. Wolz, A. V. Ustinov, and M. Weides: *Probing the Tavis-Cummings Level Splitting with Intermediate-Scale Superconducting Circuits*. Physical Review Applied **14**.2 (2020), p. 024025. DOI: 10.1103/PhysRevApplied.14.024025 (cit. on p. 80).

[YSK92] S. Yoakum, L. Sirko, and P. M. Koch: *Stueckelberg oscillations in the multiphoton excitation of helium Rydberg atoms: Observation with a pulse of coherent field and suppression by additive noise*. Physical Review Letters **69**.13 (1992), pp. 1919–1922. DOI: 10.1103/PhysRevLett.69.1919 (cit. on pp. 4, 75).

[Yon+18] J. Yoneda, K. Takeda, T. Otsuka, T. Nakajima, M. R. Delbecq, G. Allison, T. Honda, T. Kodera, S. Oda, Y. Hoshi, N. Usami, K. M. Itoh, and S. Tarucha: *A quantum-dot spin qubit with coherence limited by charge noise and fidelity higher than 99.9%*. Nature Nanotechnology **13**.2 (2018), pp. 102–106. DOI: 10.1038/s41565-017-0014-x (cit. on p. 13).

[ZFR16] A. M. Zagoskin, D. Felbacq, and E. Rousseau: *Quantum metamaterials in the microwave and optical ranges*. EPJ Quantum Technology **3**.1 (2016), p. 2. DOI: 10.1140/epjqt/s40507-016-0040-x (cit. on p. 13).

[Zen32] C. Zener: *Non-adiabatic crossing of energy levels*. Proc. Roy. Soc. A **33**.1929 (1932), pp. 696–702 (cit. on pp. 3, 73).

[Zen+09] A. Zenesini, H. Lignier, G. Tayebirad, J. Radogostowicz, D. Ciampini, R. Mannella, S. Wimberger, O. Morsch, and E. Arimondo: *Time-Resolved Measurement of Landau-Zener Tunneling in Periodic Potentials*. Physical Review Letters **103**.9 (2009), p. 090403. DOI: 10.1103/PhysRevLett.103.090403 (cit. on pp. 4, 75).

[Zha+20] H. Zhang, S. Chakram, T. Roy, N. Earnest, Y. Lu, Z. Huang, D. Weiss, J. Koch, and D. I. Schuster: *Universal fast flux control of a coherent, low-frequency qubit* (2020), pp. 1–12. URL: http://arxiv.org/abs/2002.10653 (cit. on pp. 2, 44, 55).

[Zha+17] J. Zhang, G. Pagano, P. W. Hess, A. Kyprianidis, P. Becker, H. Kaplan, A. V. Gorshkov, Z.-X. Gong, and C. Monroe: *Observation of a many-body dynamical phase transition with a 53-qubit quantum simulator*. Nature **551**.7682 (2017), pp. 601–604. DOI: 10.1038/nature24654 (cit. on pp. 3, 71).

[ZR04] J. Zmuidzinas and P. Richards: *Superconducting detectors and mixers for millimeter and submillimeter astrophysics*. Proceedings of the IEEE **92**.10 (2004), pp. 1597–1616. DOI: 10.1109/JPROC.2004.833670 (cit. on p. 5).

[ZHK08] D. Zueco, P. Hänggi, and S. Kohler: *Landau–Zener tunnelling in dissipative circuit QED*. New Journal of Physics **10**.11 (2008), p. 115012. DOI: 10.1088/1367-2630/10/11/115012 (cit. on pp. 4, 75).

# List of publications


[Bra+17] J. Braumüller, M. Marthaler, A. Schneider, A. Stehli, H. Rotzinger, M. Weides, and A. V. Ustinov: *Analog quantum simulation of the Rabi model in the ultra-strong coupling regime*. Nature Communications **8**.1 (2017), p. 779. DOI: 10.1038/s41467-017-00894-w.

[Bre+21] J. D. Brehm, A. N. Poddubny, A. Stehli, T. Wolz, H. Rotzinger, and A. V. Ustinov: *Waveguide bandgap engineering with an array of superconducting qubits*. npj Quantum Materials **6**.1 (2021), p. 10. DOI: 10.1038/s41535-021-00310-z.

[Kri+20] M. Kristen, A. Schneider, A. Stehli, T. Wolz, S. Danilin, H. S. Ku, J. Long, X. Wu, R. Lake, D. P. Pappas, A. V. Ustinov, and M. Weides: *Amplitude and frequency sensing of microwave fields with a superconducting transmon qudit*. npj Quantum Information **6**.1 (2020), p. 57. DOI: 10.1038/s41534-020-00287-w.

[Ste+20] A. Stehli, J. D. Brehm, T. Wolz, P. Baity, S. Danilin, V. Seferai, H. Rotzinger, A. V. Ustinov, and M. Weides: *Coherent superconducting qubits from a subtractive junction fabrication process*. Applied Physics Letters **117**.12 (2020), p. 124005. DOI: 10.1063/5.0023533.

[Wol+20] T. Wolz, A. Stehli, A. Schneider, I. Boventer, R. Macêdo, A. V. Ustinov, M. Kläui, and M. Weides: *Introducing coherent time control to cavity magnon-polariton modes*. Communications Physics **3**.1 (2020), p. 3. DOI: 10.1038/s42005-019-0266-x.

[Yan+20] P. Yang, J. D. Brehm, J. Leppäkangas, L. Guo, M. Marthaler, I. Boventer, A. Stehli, T. Wolz, A. V. Ustinov, and M. Weides: *Probing the Tavis-Cummings Level Splitting with Intermediate-Scale Superconducting Circuits*. Physical Review Applied **14**.2 (2020), p. 024025. DOI: 10.1103/PhysRevApplied.14.024025.

# Appendix

## A Going into the rotating frame

Going into a a rotating frame is a useful mathematical trick to eliminate time dependent drive fields. In some cases an additional rotating wave approximation (RWA) can be applied, removing fast rotating terms from the Hamiltonian.

In general, for a unitary transformation we can write

$$|\psi'\rangle = \hat{U}^\dagger |\psi\rangle \,, \tag{A1}$$

where $|\psi\rangle$ is an arbitrary quantum state and $\hat{U}^\dagger$ is a unitary transformation, i.e., $\hat{U}^\dagger\hat{U} = \mathbb{1}$. Plugging $|\psi'\rangle$ into the Schrödinger equation yields

$$\mathrm{i}\hbar \frac{\mathrm{d}}{\mathrm{d}t} |\psi'\rangle = i\hbar \frac{\partial \hat{U}^\dagger}{\partial t} |\psi\rangle + \hat{U}^\dagger \overbrace{\mathrm{i}\hbar \frac{\partial}{\partial t} |\psi\rangle}^{=\hat{H}|\psi\rangle} \tag{A2}$$

Restricting ourselves to transformations of the form

$$\hat{U} = \exp\left(-\mathrm{i}\hat{A}t\right), \tag{A3}$$

where $\hat{A}$ is an arbitrary but time-independent operator, Eq. (A2) simplifies to

$$\mathrm{i}\hbar \frac{\mathrm{d}}{\mathrm{d}t} |\psi'\rangle = -\hat{A} \overbrace{\hat{U}^\dagger |\psi\rangle}^{=|\psi'\rangle} + \hat{U}^\dagger \hat{H} \hat{U} \overbrace{\hat{U}^\dagger |\psi\rangle}^{=|\psi'\rangle}, \tag{A4}$$

which may be written as

$$\mathrm{i}\hbar \frac{\mathrm{d}}{\mathrm{d}t} |\psi'\rangle = \overbrace{\left(\hat{U}^\dagger \hat{H} \hat{U} - \hat{A}\right)}^{\hat{H}'} |\psi'\rangle \,, \tag{A5}$$

a Schrödinger equation for $|\psi'\rangle$.

# B Quantum harmonic oscillator

This section comprises a treatment of the quantum *LC*-oscillator in the basis of charge operator $\hat{n}$ and phase operator $\hat{\varphi}$. The Hamiltonian reads

$$\hat{H}_{\mathrm{osci}} = 4E_{\mathrm{C}}\hat{n}^2 + \frac{E_{\mathrm{L}}}{2}\hat{\varphi}^2, \tag{B6}$$

with $E_{\mathrm{C}} = e^2/C$ and $E_{\mathrm{L}} = (\Phi_0/2\pi)^2/L$. Since phase and charge do not commute, with the commutator $[\hat{\varphi}, \hat{n}] = i$, we find the creation operator

$$\hat{a} = \left(\frac{E_{\mathrm{L}}}{32E_{\mathrm{C}}}\right)^{\frac{1}{4}} \left(\hat{\varphi} + \mathrm{i}\left(\frac{8E_{\mathrm{C}}}{E_{\mathrm{L}}}\right)^{\frac{1}{2}} \hat{n}\right). \tag{B7}$$

Rewriting $\hat{n}$ and $\hat{\varphi}$ in terms of $\hat{a}^\dagger$ and $\hat{a}$ yields

$$\begin{aligned} \hat{\varphi} &= \left(\frac{2E_{\mathrm{C}}}{E_{\mathrm{L}}}\right)^{\frac{1}{4}} \left(\hat{a}^\dagger + \hat{a}\right) \\ \hat{n} &= \mathrm{i}\left(\frac{E_{\mathrm{L}}}{32E_{\mathrm{C}}}\right)^{\frac{1}{4}} \left(\hat{a}^\dagger - \hat{a}\right) \end{aligned} \tag{B8}$$

Finally, inserting in Eq. (B6), the Hamiltonian is rewritten as

$$\hat{H}_{\mathrm{osci}} = \sqrt{8E_{\mathrm{L}}E_{\mathrm{C}}}\left(\hat{a}^\dagger\hat{a} + \frac{1}{2}\right), \tag{B9}$$

where the eigenfrequency is calculated as $\omega = 1/\sqrt{LC}$, using the definitions of $E_{\mathrm{C}}$ and $E_{\mathrm{L}}$.

# C Circuit quantization

The capacitance matrix of the circuit in Fig. 4.6(b) reads

$$C = \begin{pmatrix} C_{\mathrm{q}} + C_{\mathrm{c}} & -C_{\mathrm{c}} \\ -C_{\mathrm{c}} & C_{\mathrm{r}} + C_{\mathrm{c}} \end{pmatrix}, \tag{C10}$$

with the coupling capacitance $C_{\mathrm{c}}$ between qubit and resonator, with a respective capacitance of $C_{\mathrm{q}}$ and $C_{\mathrm{r}}$ to ground. The inverse of $C$ is given by

$$C^{-1} = \frac{1}{\left(C_{\mathrm{q}} + C_{\mathrm{r}}\right)C_{\mathrm{c}} + C_{\mathrm{q}}C_{\mathrm{r}}} \begin{pmatrix} C_{\mathrm{r}} + C_{\mathrm{c}} & C_{\mathrm{c}} \\ C_{\mathrm{c}} & C_{\mathrm{q}} + C_{\mathrm{c}} \end{pmatrix}. \tag{C11}$$

Inserting into Eq. (4.16) yields the effective qubit, resonator, and coupling capacitances

$$\begin{aligned} C_{\mathrm{q}}^{\mathrm{eff}} &= C_{\mathrm{q}} + C_{\mathrm{c}} - \frac{C_{\mathrm{c}}^2}{C_{\mathrm{r}} + C_{\mathrm{c}}}, \\ C_{\mathrm{r}}^{\mathrm{eff}} &= C_{\mathrm{r}} + C_{\mathrm{c}} - \frac{C_{\mathrm{c}}^2}{C_{\mathrm{q}} + C_{\mathrm{c}}}, \\ C_{\mathrm{c}}^{\mathrm{eff}} &= C_{\mathrm{q}} + C_{\mathrm{r}} + \frac{C_{\mathrm{q}} C_{\mathrm{r}}}{C_{\mathrm{c}}}, \end{aligned} \tag{C12}$$

and the coupled qubit-resonator Hamiltonian:

$$\hat{H} = \frac{\hat{q}_{\mathrm{q}}^2}{2C_{\mathrm{q}}^{\mathrm{eff}}} - E_{\mathrm{J}} \cos\left(2\pi \frac{\hat{\phi}_{\mathrm{q}}}{\Phi_0}\right) + \frac{\hat{q}_{\mathrm{r}}^2}{2C_{\mathrm{r}}^{\mathrm{eff}}} + \frac{\hat{\phi}_{\mathrm{r}}^2}{2L} + \frac{\hat{q}_{\mathrm{q}} \hat{q}_{\mathrm{r}}}{C_{\mathrm{c}}^{\mathrm{eff}}}. \tag{C13}$$

Inserting the charge and phase operators in terms of the creation and annihilation operators $\hat{a}^\dagger(\hat{a})$ and $\hat{b}^\dagger(\hat{b})$ of resonator and qubit, respectively, see Eq. (B8), results in

$$\hat{H} = \hat{H}_{\mathrm{tr}} + \hat{H}_{\mathrm{osci}} - \overbrace{\frac{1}{C_{\mathrm{c}}^{\mathrm{eff}}} \left(\frac{\hbar\omega_{\mathrm{r}}}{2} C_{\mathrm{r}}^{\mathrm{eff}}\right)^{\frac{1}{2}} \left(\frac{\hbar\left(\omega_{\mathrm{q}} - \alpha\right)}{2} C_{\mathrm{q}}^{\mathrm{eff}}\right)^{\frac{1}{2}}}^{\hbar g} \left(\hat{a}^\dagger - \hat{a}\right)\left(\hat{b}^\dagger - \hat{b}\right), \tag{C14}$$

with the Hamilton operators of the transmon qubit, see Eq. (3.32), and harmonic oscillator, see Eq. (B9). Here, $\omega_{\mathrm{r}}$ and $\omega_{\mathrm{q}}$ are the frequencies of resonator and qubit, and $\alpha$ is the transmon's anharmonicity. Finally, a rotating wave approximation yields the well-known Jaynes-Cummings model, see Eq. (3.23), of a transmon coupled to a bosonic mode. For a small $\alpha$ and $C_{\mathrm{c}}$, the coupling strength $g$ of qubit and resonator simplifies to

$$g \approx C_{\mathrm{c}} \left(\frac{\hbar\omega_{\mathrm{r}}}{2C_{\mathrm{r}}}\right)^{\frac{1}{2}} \left(\frac{\hbar\omega_{\mathrm{q}}}{2C_{\mathrm{q}}}\right)^{\frac{1}{2}} \tag{C15}$$

# D Fabrication parameters

**Table 1: Resist application**. The parameters include the ramp speed $\nu_r$ and time $t_r$, the acceleration $a$ of the spin coater, the maximum rotation speed $\nu_s$ and time $t_s$, as well as the bake temperature $T_B$ and time $t_B$.

| resist | $a$ (rpm/s) | $\nu_r$ (rpm) | $t_r$ (s) | $\nu_s$ (rpm) | $t_s$ (s) | $T_B$ (°C) | $t_B$ (s) |
|---|---|---|---|---|---|---|---|
| S1805 (optical) | 7500 | 500 | 1 | 6000 | 60 | 115 | 60 |
| AZ5414E (ABs) | 7500 | 500 | 5 | 1000 | 60 | 110 | 50 |
| PMMA 950K (e-beam) | 7500 | 300 | 10 | 1200 | 60 | 145 | 300 |
| S1818 (protective coating) | 2000 | – | – | 4500 | 60 | 80 | 300 |

**Table 2: Optical resist exposure parameters**. Independent of the resist, the UV light wavelength is 365 nm at a lamp power of 500 W. A filter can be used to further decrease the intensity.

| resist | intensity (mW/cm$^2$) | duration (s) | filter |
|---|---|---|---|
| S1805 (optical) | 2 | 10 | yes |
| AZ5414E (ABs) | 13 | 5.5 | no |

**Table 3: Electron-beam exposure parameters**. The resist was applied one hour before the installation in the 50 keV JEOL JBX-5500ZD electron-beam writer.

| resist | base dose (µC/cm$^2$) | current (nA) |
|---|---|---|
| PMMA 950K | 260 | 2 |

**Table 4: Development parameterss.**

| resist | developer | duration (s) | stopper/rinse |
|---|---|---|---|
| S1805 (optical) | AZ-developer/$H_2O$ (3:2 ratio) | 30 | $H_2O$ (>60 s) |
| AZ5414E (ABs) | AZ-developer/$H_2O$ (1:1 ratio) | 70 | $H_2O$ (>60 s) |
| PMMA 950K (e-beam) | MIBK/IPA (1:3 ratio) | 60 | IPA (30 s), $H_2O$ (60 s) |

**Table 5: Resist removal and sample cleaning.**

| type | strippers | hotplate | ultrasonic cleaning | rinse |
|---|---|---|---|---|
| pre-processing | piranha solution, acetone | in NEP 20 min at 90 °C | in NEP, 5 min | IPA |
| post-processing | acetone (flush), NEP (> 12 h) | in NEP, > 4 h at 90 °C | – | IPA |

# E Qubit aging

Table 6 comprises the qubit frequencies of the sample studied in Sec. 5.3, before and after $\sim$ 6 months of aging in ambient conditions.

**Table 6: Effects of aging on the qubit frequency.** The table comprises the qubit frequency $\omega_{q,\,new}$ before and $\omega_{q,\,old}$ after $\sim$ 6 months of aging in ambient conditions, as well as the frequency shift $\Delta\omega_q = \omega_{q,\,new} - \omega_{q,\,old}$.

| qubit | $\omega_{q,\,new}$ (GHz) | $\omega_{q,\,old}$ (GHz) | $\Delta\omega_q$ (GHz) |
|---|---|---|---|
| $q_1$ | 3.548 | 3.556 | 0.008 |
| $q_2$ | 3.950 | 3.959 | 0.009 |
| $q_3$ | 3.161 | 3.201 | 0.040 |
| $q_4$ | 3.324 | 3.345 | 0.021 |

# Acknowledgments

I want to thank Prof. Alexey V. Ustinov for giving me the opportunity to work under his guidance in his group as a Bachelor, Master, and eventually as a PhD student. Over the past few years, we had fruitful discussions, where I learned a lot about science but also life. Especially, during my time as a PhD student, I enjoyed a great freedom in my research, which allowed me to grow as a scientist and person. All of this was possible in the flourishing and cooperative work environment you generate for the group. In particular, I enjoyed the seminar on high frequency waves as well as the regular conferences on low temperature physics. Thank you for making this possible.

I am grateful to Prof. Martin Weides, my second reviewer and adviser. Under his supervision, I began my studies as a Bachelor's student, where I learned what it means to be a scientist. He also motivated me to stick with the group for my Master's degree and PhD. Throughout the past years you had an open ear for questions and discussions at all times. You were always easy to talk to, both on professional and personal matters. Thank you for everything!

A big thanks goes to Dr. Hannes Rotzinger for giving useful advice in many situations. I enjoyed our discussions on physics and beyond. You always had an interesting anecdote to share regardless of the topic of conversation.

I want to thank Andre Schneider, the good soul of our group, who always offered a helping hand to those in need. You cleared the way for most of us to start measuring without having to write another 5000 lines of qKIT code. I am also grateful to my companion Jan Brehm. Together we struggled through hard times, but be it in the cleanroom or at the silver fridge, you always had my back. Thanks also to Tim Wolz for our regular and fruitful discussions. Your harsh (but justified) criticism of any written document I provided, helped me to improve my writing skills. I want to thank Patrick Winkel for his company and humor, but most of all for convincing me to grow a beard. Your diligence and overall work ethic was inspiring. A big thanks also goes to Dr. Jochen Braumüller for mentoring me during my Master's thesis and beyond. I will always remember the amazing time as a member of "team transmon".

I want to thank Alexander Bilmes, Marco Pfirrman, Tim Wolz and Yannick Schön for the colorful climate in our office. Please remember to clean your whiteboards! Big thanks also to my former office mates from 4-05, Nico Voss, Micha Wildermuth, and Max Kristen. It was not always productive, but certainly, we had fun. Keep up the good work.

I would like to thank Dr. Sasha Lukashenko for teaching me how to solder and for useful input on operating the silver fridge.

I am grateful to Steffen Schlör, Tim Wolz, Andre Schneider, Maximilian Kristen, and Jan Brehm for proof-reading my thesis. All of you had great input (if nothing else, there are certainly less spelling errors)!

A big thanks goes to all remaining scientific members of the institute, past and present. Each and everyone of you shaped the friendly work environment we have here at the PHI.

Ein großes Dankeschön gilt auch den Angestellten des PHI, insbesondere der Elektronik- und Mechanikwerkstatt, sowie Steffi Baatz und Claudia Alaya im Sekretariat. Mit eurer harten Arbeit nehmt ihr uns so manche Hürde, so dass wir uns auf die Wissenschaft konzentrieren können. Vielen Dank auch an Lukas Radtke, der mich über all die Jahre tatkräftig im Reinraum unterstützt hat und mir mit guten Ratschlägen zur Seite stand. Danke auch an Silvia Diewald für ihre Unterstützung bei der Elektronenstrahllithografie.

Mit der größte Dank gebührt meiner Familie, insbesondere meinen Eltern und meinem Lieblingsbrudi, Lars. Ihr habt immer an mich geglaubt und mich ermutigt, meinen eigenen Weg zu gehen. Dank euch bin ich zu dem geworden, der ich bin.

Zum Schluss, aber nicht zuletzt, möchte ich mich bei meiner Freundin Christina bedanken. Du hast mich während des gesamten Studiums und insbesondere während der Promotion unterstützt und motiviert. Vielen Dank dafür!

Karlsruhe, February 2021 M. Sc. Alexander Stehli